

©2012

Sean R. Stratton

ALL RIGHTS RESERVED

**MEASUREMENT OF THE FLUX OF ULTRA-HIGH ENERGY COSMIC RAYS  
BY THE TELESCOPE ARRAY FADC FLUORESCENCE DETECTORS**

BY SEAN R. STRATTON

A dissertation submitted to the  
Graduate School—New Brunswick  
Rutgers, the State University of New Jersey  
in partial fulfillment of the requirements

for the degree of

Doctor of Philosophy

Graduate Program in Physics and Astronomy

Written under the direction of

Professor Stephen Schnetzer

and approved by

---

---

---

---

---

New Brunswick, New Jersey

October, 2012

ABSTRACT OF THE DISSERTATION

**Measurement of the Flux of Ultra-High Energy Cosmic Rays by the  
Telescope Array FADC Fluorescence Detectors**

**by Sean R. Stratton**

**Dissertation Director: Stephen Schnetzer**

Ultra-high energy cosmic rays (UHECRs) produce the most powerful collisions between single particles and atmospheric matter. They have been studied since the early 20<sup>th</sup> century yet, to this date, there is no clear answer as to the acceleration process responsible for their production. The Telescope Array Project is an experiment designed to observe the showers of particles produced as by-products of the interactions between UHECRs and the atmosphere. As a *hybrid* experiment, it currently utilizes 38 fluorescence detectors (FDs) divided between three sites overlooking an array of 507 surface detectors (SDs). The project's mission is to study the energy, composition and origin of UHECRs using a variety of techniques which may include some or all of the experiment's apparatus. This document, in particular, is a presentation of the UHECR energy spectrum measured at Telescope Array using the fluorescence detection technique in *monocular* mode. Only data from the 24 FDs at Black Rock Mesa (BR) and Long Ridge (LR) stations are used here.

## PREFACE

Whenever I'm approached by somebody and asked what I do, I usually respond in the following order: I am a graduate student at Rutgers, I study Physics, and my thesis is on the phenomenon of ultra-high energy cosmic rays. The response is usually raised eyebrows, widened eyes and statements like "Wow, Physics... That's heavy stuff." If the conversation manages to continue, the next obvious question is, "Why cosmic rays?" I must admit, my entry into the cosmic ray research community was purely happenstance. As a sophomore at the University of Utah I still only had a vague idea of where I was heading, academically. I had always been interested in astronomy and engineering and had a knack for mathematics. But I also recognized the importance of becoming involved with a research group at the university as a means of gaining experience and making connections which might help after graduation. Before I knew it, I was a member of the High-Resolution Fly's Eye experiment, entering with literally zero awareness of cosmic rays. I stayed for ten years because, while the work was challenging, it was also exciting, fun and *interesting* (I'll explain the emphasis momentarily).

I can still remember watching the event display at the HiRes III air fluorescence detector, five years before the valley floor would be spattered with surface detectors and flanked by a multi-million dollar array of fluorescence detectors. I watched in amazement while the tracks lit up the display. Here was a device picking up the invisible light generated as charged particles streak through the atmosphere, and this wasn't just happening because we were looking. This is a phenomenon that is occurring now, all over the world, as it has been as long as Earth had an atmosphere. How many people do you think are aware of this?

Ultra-high energy cosmic rays frequently collide with Earth's atmosphere, they are tens to hundreds of millions of times more energetic than the protons accelerated by the Large Hadron Collider and, to date, nobody can say where they are coming from. Unfortunately, most people won't find this interesting. And why should they? What happens when we discover the source of ultra-high energy cosmic rays? It won't solve world hunger. It won't bring peace to the Middle

East. It won't balance the US budget. So if taxpayers are going to pay millions of dollars funding research, then shouldn't it be directed towards solving these problems? The people who would ask such a question should realize that the benefits may not come from the *product* of the research projects, but from their *execution*. The town of Delta, Utah and Millard County receives an estimated million dollars a year from the Telescope Array collaboration through house rentals, food, supplies and even souvenirs. As the experiment expands, infrastructure must be developed which means new construction contracts and jobs. Graduate and undergraduate students gain experience working with cutting edge technology and international relationships are forged bringing people from different cultures together. Scientists want to perform the research because they're interested in studying the phenomena. Governments are willing to subsidize these projects because the work has a positive effect on the economy and overall quality of life. Only now is that truly becoming clear to me.

This thesis presents the measurement of the Ultra-high energy cosmic ray flux by the Telescope Array fluorescence detectors. It is, for the most part, a description of experimental apparatus and data analysis methods. I start with the big picture, that is an introduction to cosmic ray theory (Chapter 1), followed by a description of the hardware and software used to collect and analyze cosmic ray air shower data (Chapter 2, Chapter 3 and Chapter 4), and finally focus on a simple plot with just 21 data points (Chapter 5). However, most readers of this document will be less interested in that plot (the *objective* of this thesis!) and more interested in the techniques used to determine where the points on that plot are placed. I see this as a fitting analogy to the research project itself, that is, the means are more relevant than the ends.

I emphasized the word *interest* earlier because I believe people don't work to learn about things when they are not interested in them. As I try to recall my state of mind throughout my experience with this research group, I'm realizing something I hadn't thought of before. Aside from developing experience with the experiment's hardware and skills in problem-solving, my perspective has widened as well. I entered understanding little more than the benefit I would re-

ceive through my employment with the group. Now, as my task completes, I understand the important contribution “pure” research has to society and I am thrilled to be a part of that.

If you, the reader, are using this document as a means of understanding the methods for performing an UHECR energy spectrum measurement using similar methods, or checking for errors or misplaced assumptions, then this thesis will have served its purpose. If you happen to be a new graduate student entering school with a state of mind similar to what I had coming in, then I hope I have opened your eyes to a bigger picture. No matter who you are, thank you for taking the time to read this. I hope this work serves you well.

## ACKNOWLEDGEMENTS

First and most importantly, I would like to thank my wife, Laura, for without her incredible support and encouragement I would not be writing this today.

I would like to thank my de facto advisor, Douglas Bergman, who taught me to balance careful attention to detail while maintaining a clear view of the broader picture.

Robert and Leslie Leith, Donald Stratton, Melissa McIntire, Steven Kuznicki, brother Douglas, brothers and sisters-in-law Matthew, Martii, David, Malissa, Dan, Jennifer, Michael, Amanda and Steven, “bonus” brother and sisters Ian, Mandy and Sandra, and the rest of my extended family. Your influence in the past helped shape who I am today and your support in the present helped me achieve this great goal.

My closest friends, including those I knew entering college and those I have met since, whose encouragement and support has been a constant driving force. There are simply too many of you to name here.

The other members of the Telescope Array Collaboration, for many of which there is no distinction between colleague and close friend. I do, however, owe special debts of gratitude to Jeremy Smith, Stan Thomas, Tom Stroman, Elliott Barcikowski, Zachary Zundel, Lauren Scott, Gareth Hughes, Benjamin Jones, Douglas Rodriguez, Yoshiki Tsunesada, Akimichi Taketa, Toshihiro Fujii, Shoichi Ogio, Daisuke Ikeda, Mike & Gary and, of course, John Matthews. You all, at some point, have interrupted your own duties to help me with my little problems. Thank you, and my apologies to those I forgot to name.

The faculty and staff of the Rutgers University Department of Physics and Astronomy, especially Shirley Hinds, Helen Posluszny, Nancy DeHaan and Ronald Ransome.

The faculty and staff of the University of Utah Department of Physics and Astronomy, especially Heidi Frank, Vicki Nielsen, John DeFord and Lynn Higgs.

The Telescope Array experiment is supported by,

The Japan Society for the Promotion of Science through Grants-in-Aid for Scientific Research on Specially Promoted Research (21000002) “Extreme Phenomena in the Universe Explored by Highest Energy Cosmic Rays”, and the Inter-University Research Program of the Institute for Cosmic Ray Research.

The U.S. National Science Foundation awards PHY-0307098, PHY-0601915, PHY-0703893, PHY-0758342, and PHY-0848320 (Utah) and PHY-0649681 (Rutgers).

The National Research Foundation of Korea (2006-0050031, 2007-0056005, 2007-0093860, 2010-0011378, 2010-0028071, R32-10130)

The Russian Academy of Sciences, RFBR grants 10-02-01406a and 11-02-01528a (INR), IISN project No. 4.4509.10 and Belgian Science Policy under IUAP VI/11 (ULB).

The foundations of Dr. Ezekiel R. and Edna Wattis Dumke, Willard L. Eccles and George S. and Dolores Doré Eccles all helped with generous donations.

The State of Utah supported the project through its Economic Development Board, and the University of Utah through the Office of the Vice President for Research.

The experimental site became available through the cooperation of the Utah School and Institutional Trust Lands Administration (SITLA), U.S. Bureau of Land Management and the U.S. Air Force.

We also wish to thank the people and the officials of Millard County, Utah, for their steadfast and warm support.

We gratefully acknowledge the contributions from the technical staffs of our home institutions and the University of Utah Center for High Performance Computing (CHPC).

This research was supported in part by the National Science Foundation through TeraGrid resources provided by Purdue University and Indiana University under grant number TG-PHY100060.

DEDICATION

*for Parker*

*“Once you’ve come to the conclusion that what you know already is all you need to know, then you have a degree in disinterest.”*

John Dobson, from *A Sidewalk Astronomer*

## TABLE OF CONTENTS

Abstract of the Dissertation .....	ii
Preface .....	iii
Acknowledgements.....	vi
Dedication.....	viii
List of Tables .....	xii
List of Figures.....	xiii
Chapter 1. Ultra-High Energy Cosmic Ray Theory.....	1
1.1. First Observation of Cosmic Rays.....	1
1.2. Background .....	3
1.3. UHECR Origins .....	5
1.4. First-Order Fermi Acceleration .....	8
1.5. UHECR Propagation .....	10
1.6. The Extensive Air Shower.....	11
Chapter 2. The Telescope Array Project.....	15
2.1. Experiment and Apparatus .....	15
2.2. The FADC Fluorescence Telescopes .....	17
2.3. Photomultiplier Tubes .....	19
2.4. The Signal Digitizer/Finder and Track Finder .....	22
2.5. Detector Calibration .....	26
2.6. CRAYS.....	29
Chapter 3. Data Analysis .....	31

3.1. DST Files.....	31
3.2. Raw Data Storage.....	34
3.3. Computing Resources.....	36
3.4. TAMA .....	37
3.5. Fitting the Shower Geometry .....	39
3.6. Fitting the Shower Profile .....	44
3.7. Primary Energy Estimation .....	47
3.8. Data Selection and Quality Cuts.....	49
Chapter 4. Detector Simulation and Monte Carlo.....	51
4.1. CORSIKA Shower Library .....	51
4.2. TRUMP .....	54
4.3. Data-Monte Carlo Comparisons.....	70
Chapter 5. Measurement of the UHECR Flux .....	77
5.1. Monocular Energy Spectrum Measurement.....	77
5.2. Energy Spectrum .....	82
5.3. BR & LR Combined Spectrum.....	84
5.4. Evaluation of Detector Resolution .....	90
5.5. Evaluation of Systematic Errors .....	93
5.6. Interpretation of results .....	97
Appendix A. Geometry Correction.....	99
Appendix B. FADC Correlation .....	100

Appendix C. Recursion Relation for Waveform Simulation .....	102
Bibliography .....	106

## LIST OF TABLES

Table 2.1 The PMT gain correction factors .....	27
Table 3.1 DST banks used for this analysis .....	33
Table 3.2 Data Quality Cuts.....	50
Table 4.1 CORSIKA configurations used in TRUMP and Nerling.....	52
Table 4.2 List of configuration parameters recognized by TRUMP.....	56
Table 4.3 Constants used in fluorescence yield equation .....	59
Table 4.4 Constants used to parameterize $\alpha_{\text{eff}}$ in Nerling and this analysis .....	62
Table 5.1 Statistics for the good-weather data collected by BRM and LR FD stations.....	77
Table 5.2 Fit parameters for aperture.....	82
Table 5.3 Contribution to total systematic uncertainty due to detector calibration .....	94
Table 5.4 Contributions to the systematic uncertainty.....	96

## LIST OF FIGURES

Figure 1.1 Measurements of the flux of high energy cosmic rays by various experiments.....	5
Figure 1.2 Hillas plot showing potential UHECR sources .....	7
Figure 1.3 Magnetic abnormality in the presence of a strong planar shock wave .....	10
Figure 1.4 Schematic of the Heitler toy model EM cascade, reproduced from Matthews .....	13
Figure 2.1 Political map of the Telescope Array Experiment.....	16
Figure 2.2 Schematic of a fluorescence telescope ring 1/ring 2 pair .....	18
Figure 2.3 Basic components of a photomultiplier tube .....	19
Figure 2.4 Example QE measurements from four photomultiplier tubes .....	20
Figure 2.5 PMT uniformity map.....	21
Figure 2.6 Schematic diagram of the track finding process.....	24
Figure 2.7 Schematic diagram of the partial track search near the boundary of a camera .....	24
Figure 2.8 SDF Flow Chart.....	25
Figure 2.9 FADC FD Data flow chart.....	25
Figure 2.10 Schematic of the YAP module .....	28
Figure 2.11 Diagram of CRAYS apparatus .....	30
Figure 3.1 Diagram of main components of a DST file.....	32
Figure 3.2 File naming convention for raw FD data.....	34
Figure 3.3 Raw Data Format.....	35
Figure 3.4 Waveform data packing.....	36
Figure 3.5 Computing resource map.....	37
Figure 3.6 Signal time fit residual versus significance .....	38
Figure 3.7 Shower geometry parameters in monocular reconstruction .....	40
Figure 3.8 Example of a shower-detector plane fit.....	42
Figure 3.9 Example of a time versus angle fit .....	43
Figure 3.10 Region of FD considered when calculating acceptance .....	45

Figure 3.11 Missing energy correction derived from CORSIKA showers .....	47
Figure 3.12 Missing energy correction compared to other estimates .....	48
Figure 4.1 Gaisser-Hillas parameter dependence on $E$ and $\theta$ .....	55
Figure 4.2 Fluorescence Spectrum Lines .....	60
Figure 4.3 Contribution of Čerenkov light to the total light collected for each event .....	63
Figure 4.4 Rayleigh and Aerosol scattering phase functions .....	67
Figure 4.5 Data-Monte Carlo comparison of waveform power spectra .....	72
Figure 4.6 Waveform autocorrelation between each time bin with the next ( $\log E > 17.5eV$ )....	72
Figure 4.7 Waveform autocorrelation between time bins separated by 200ns ( $\log E > 17.5eV$ ). 72	
Figure 4.8 Data-Monte Carlo comparisons of $R_p$ distributions ( $\log E > 17.5eV$ ).....	73
Figure 4.9 Data-Monte Carlo comparisons of $\psi$ distributions ( $\log E > 17.5eV$ ) .....	73
Figure 4.10 Data-Monte Carlo comparisons of $\log(N_{PE}/deg)$ ( $\log E > 17.5eV$ ).....	73
Figure 4.11 Data-Monte Carlo comparisons of track length distributions ( $\log E > 17.5eV$ ) .....	74
Figure 4.12 Data-Monte Carlo comparisons of event duration ( $\log E > 17.5eV$ ) .....	74
Figure 4.13 Data-Monte Carlo comparisons of zenith angle distributions ( $\log E > 17.5eV$ ).....	74
Figure 4.14 Data-Monte Carlo comparisons of shower azimuthal direction ( $\log E > 17.5eV$ )....	75
Figure 4.15 Data-Monte Carlo comparisons of the tangent fit $\chi^2/DOF$ ( $\log E > 17.5eV$ ) .....	75
Figure 4.16 Data-MC comparisons of Čerenkov fraction distributions ( $\log E > 17.5eV$ ) .....	75
Figure 4.17 Data-MC comparisons of tube viewing angle from the SDP ( $\log E > 17.5eV$ ).....	76
Figure 4.18 Data-Monte Carlo comparisons of $X_{max}$ distributions ( $\log E > 17.5eV$ ) .....	76
Figure 4.19 Data-Monte Carlo comparisons of $N_{max}$ distributions ( $\log E > 17.5eV$ ) .....	76
Figure 5.1 FD duty cycle .....	78
Figure 5.2 Fraction of dark period when the detectors were actually taking data .....	79
Figure 5.3 Distribution of primary energies for real data events .....	81
Figure 5.4 FD aperture measured by Monte Carlo method .....	83

Figure 5.5 Measurement of the UHECR flux from the three FD stations of Telescope Array.....	84
Figure 5.6 Distribution of event energies in the BR and LR combined data sets .....	85
Figure 5.7 Individual components of the combined data event distribution.....	87
Figure 5.8 Black Rock Mesa and Long Ridge combined exposures .....	88
Figure 5.9 Energy spectrum calculated by combining the BR and LR data sets .....	89
Figure 5.10 Combined energy spectrum compared to its constituent data sets .....	89
Figure 5.11 Measurement presented in this work compared to other independent experiments ...	90
Figure 5.12 $R_p$ and $\psi$ resolution plots for BR and LR FD stations .....	92
Figure 5.13 $X_{max}$ and $N_{max}$ resolution plots for BR and LR FD stations.....	92
Figure 5.14 Energy resolution plots for BR and LR FD stations.....	93
Figure A.1 Geometry Correction .....	99

# Chapter 1. Ultra-High Energy Cosmic Ray Theory

## 1.1. First Observation of Cosmic Rays

Around the turn of the 20<sup>th</sup> century, following some groundbreaking discoveries in radiation and radioactivity, there were several laboratories where scientists were studying the ionization properties of gases. A tool commonly used in these laboratories was a device called the *gold leaf electroscope*. To measure the radiation level, one would first apply a charge to a contact on the device, inducing Coulomb repulsion in the leaves. The rate at which the leaves fell back together would indicate how much ionizing radiation was present. However, it was quickly found that the electroscope would always discharge, no matter how far it was placed from known sources of radiation. After much debate, it eventually was accepted that there must be some natural source of radiation which was causing the discharge.

In 1910, physicist Theodor Wulf, known for the Wulf electrometer, sought to determine what type of radiation was causing the electroscopes to discharge [1]. At the time, there were three classes of radiation known to ionize air (i.e.  $\alpha$ ,  $\beta$  and  $\gamma$ -rays), which could be identified by their penetrating depth. Wulf surmised that if the radiation were  $\gamma$ -rays, which have the longest range, the intensity at a height of 80 meters should be half that at the surface. Using his own device, he measured the ionization radiation at the Eiffel Tower, which has a height of 330 meters. At the base of the tower he measured a level of 6 ions per cubic centimeter. At the top of the tower he observed a surprising 3.5 ions per cubic centimeter, a level far higher than what was expected [2].

Two years later, physicist Victor Hess expanded on this experiment by taking a Wulf electrometer to a height of 5km in a hot-air balloon (This was followed shortly by Verner Kolhörster, who actually ascended to 9 km!). At low altitudes, the radiation decreased with height, in

agreement with Wulf's findings [2]. However, Hess discovered that above an altitude of 1.5km, the level of radiation actually increased rapidly with height. He deduced that the radiation must come from beyond the atmosphere, calling it "cosmic radiation," a discovery which would later earn him the Nobel Prize.

After the invention of the Geiger-Müller detector in 1928, experiments performed by Kolhörster and Walther Bothe revealed not only that cosmic radiation consisted of charged particles, but that they arrived in bunches [3]. Physicist Pierre Auger explored this phenomenon, writing in his 1939 paper,

...we know that the increase of the soft group with altitude is very rapid, so we must admit that electrons of another origin than that indicated above are adding their effects to those of the decay and collision electrons from mesotrons. It seems natural to suppose that they represent the end effects of the showers that the primary particles, probably electrons, which enter the high atmosphere produced there. If this is the case, we should be able to recognize it by the existence of a "coherence" of these shower particles, the multiple effects of a single initial particle remaining bound in time and in space [4].

Through his experiments at Jungfrauoch and Pic du Midi, Auger observed coincidences in cosmic rays picked up by detectors placed several tens of meters apart, suggesting that the observed high-energy electrons were the byproducts of a single particle colliding high in the atmosphere. In the quote above Auger mentions the recently-discovered "mesotron", a particle with similar properties to the electron, yet apparently more massive and very unstable.

Theoretical physicist Hideki Yukawa believed the mesotrons to be responsible for the  $\beta$ -decay observed in extensive air showers [5]. He theorized that they must be particles with a mean life on the order of microseconds and give rise to electron-neutrino pairs (although neutrinos had yet to be discovered, their existence was widely accepted). Later experiments found that there seemed to be two kinds of mesotrons, one interacting far more weakly than the other. Both had charges of  $\pm e$  and lifetimes on the order of microseconds yet would turn out to be fundamentally different particles. The so-called "cosmic ray mesotron" would turn out to be the muon, which actually decays into an electron and a neutrino-anti-neutrino pair. The particle Yukawa was re-

ferring to was actually the  $\pi$ -meson, which decays into a muon-neutrino pair. Both the pion and the muon have similar masses (140 MeV versus 106 MeV), half-lives ( $\sim 2 \mu\text{s}$ ) and both have the same magnitude of charge, but only the pion participates in Strong Force interaction.

So this all begs the question, if the cosmic rays we observe on the ground are really the by-products of an extremely high energy collision between a single particle and Earth's atmosphere, then what are those particles and what could possibly be responsible for accelerating them to such high energies. In the conclusion of his 1939 paper, Auger states, "One of the consequences of the extension of the energy spectrum of cosmic rays up to  $10^{15}$  eV is that it is actually impossible to imagine a single process able to give to a particle such an energy" [4].

The work described above helped lay the foundation for particle collider experiments and studies in nuclear physics, eventually leading to the Standard Model Theory. Over the past 100 years, our understanding of cosmic rays has expanded dramatically with increasingly sophisticated experiments and theories. What follows is a brief description of the current state of those models as they relate to this dissertation.

## 1.2. Background

*Primary* cosmic rays refer to charged particles and stable, long-lived nuclei incident on Earth's atmosphere which have been accelerated by extraterrestrial sources. Charged particles and nuclei resulting from interactions between primary cosmic rays and the interstellar medium are called *secondary* cosmic rays, a term also used to describe high-energy pions and kaons produced after a primary cosmic ray interacts in the atmosphere. Because cosmic rays are believed to be a product of stellar nucleosynthesis, they most likely consist of electrons, protons, carbon, nitrogen, oxygen or iron nuclei.

As demonstrated in the previous section, it was known even in the early days of cosmic ray research that particles were entering our atmosphere carrying energies in excess of  $10^{15}$  eV.

Much of this was later explained by supernova remnants yet, even today, nobody can explain the acceleration mechanism behind the highest energy cosmic rays, which carry energies exceeding  $10^{18}$  eV [6]. Various theories have been presented over the years which postulate that, given some acceleration mechanism, the distribution of cosmic ray energies would follow a power law of some slope. So it is a natural first step for a cosmic ray experiment to measure their flux as a function of energy, otherwise called the cosmic ray's energy spectrum.

For this thesis, the terms *energy spectrum* and *cosmic ray flux* are used interchangeably and are defined as the number of cosmic rays carrying energy  $E$  whose trajectory is contained by the solid angle  $d\Omega$ , crossing the area  $dA$  during a time period  $dT$ . That is,

$$\frac{dN}{dE} \equiv dA d\Omega dT \cdot J(E) \quad (1.1)$$

with  $J(E)$  in units of  $(\text{eV m}^2 \text{ sr sec})^{-1}$ . The cosmic ray energy spectrum has been studied for decades because the various kinks and power law slopes provide clues to the phenomena behind their acceleration. The measurements by various experiments are shown together in Figure 1.1. Below  $10^{10}$  eV, particles are deflected by the solar wind and Earth's magnetic field, so primary cosmic rays observed on Earth are typically of extra-solar origin. Near  $10^{15}$  eV, there is a sharp decline in flux as a function of primary cosmic ray energy. Referred to as the knee, this is generally believed to be the limit of acceleration by sources within our galaxy. Near  $10^{19.6}$  eV lies the Greissen-Zatsepin-Kuzmin (GZK) suppression, beyond which protons interact with the cosmic microwave background radiation (CMBR) with sufficient energy to produce a nucleon and pion at rest [8]. Just below the GZK limit is a feature called the "ankle", the physical meaning of which is still under debate. One explanation for this feature is that an excess in the measured flux is generated just below the GZK limit by primary cosmic rays that have been accelerated to super-GZK energies and subsequently lost energy via pion production. Alternatively, it may correspond to a lower limit to extragalactic cosmic ray energies. Cosmic rays entering our galaxy are

subject to deflection by the galactic magnetic field (GMF) and lose energy via interaction with the CMBR. Higher energy particles have longer interaction lengths and are less prone to magnetic field deflection. But there is a more important question here: What could possibly accelerate particles to such high energies in the first place?

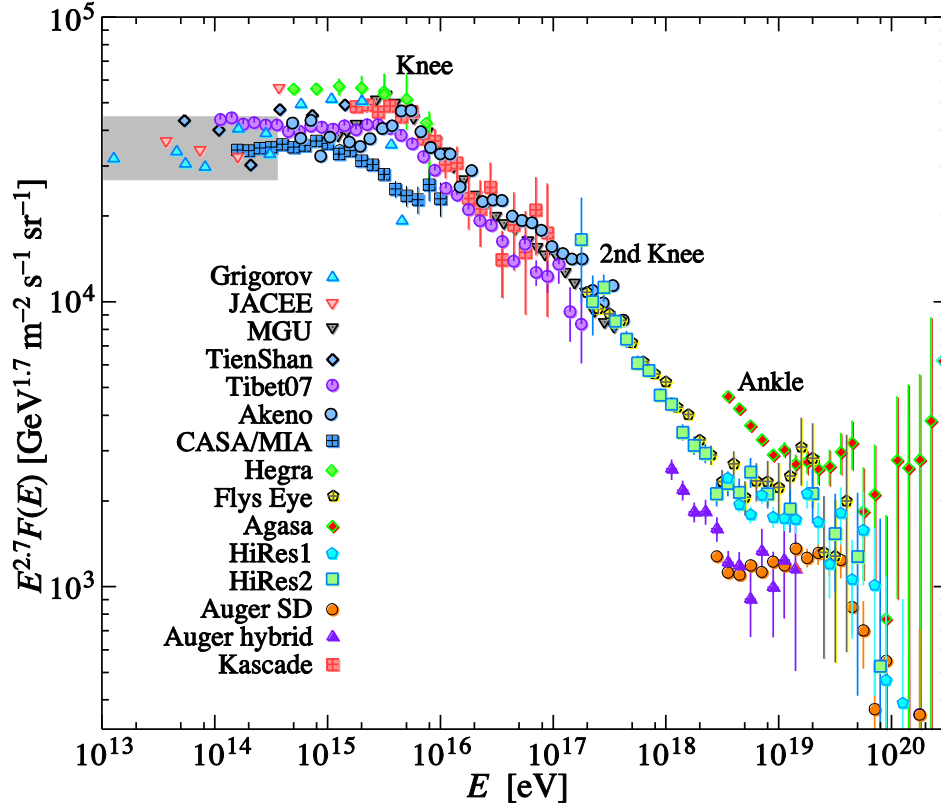


**Figure 1.1** Measurements of the differential flux of high energy cosmic rays by various experiments [7].

### 1.3. UHECR Origins

Ultra-high energy cosmic rays, referring to primary particles carrying energies in excess of  $10^{17}$  eV, occur much more rarely than those produced by supernova remnants within our galaxy. However, one may derive from Figure 1.1 that about ten  $10^{18}$  eV cosmic ray events cross a single square kilometer each year. Today, a cosmic ray experiment which covers hundreds of square kilometers would seem small, yet wouldn't take long to acquire an energy spectrum meas-

urement up to  $10^{19}$  eV. Larger experiments operating for longer periods will eventually resolve the GZK effect. Amazingly, collisions between cosmic rays and the atmosphere regularly occur with energies well over  $10^{18}$  eV while the largest particle collider on Earth can accelerate protons to a few tens of TeV. Furthermore, there are no objects known to exist which can accelerate particles to such energies. Experimentalists and theorists are attempting to answer the question of the origin of UHECRs from opposite ends.

UHECR experimental data yields primary cosmic ray energies and their trajectories as they enter Earth's atmosphere. The data may be used to isolate potential sources of UHECRs, but the analysis faces two major difficulties. First, due to the GMF, only the highest energy cosmic rays ( $\gtrsim 10^{19}$  eV) can be reliably traced back to their origin [9]. About a dozen or so of these events are observed each year, so it takes a very long time to accumulate enough data to allow for a significant result. Second, because a comparison is being made between an observed distribution of sources and maps of known objects, it is easy to apply an event selection algorithm that maximizes the significance of the observed correlations, thus increasing the risk of a confirmation bias. An alternative is to ignore the catalogues and study the multi-pole moments of the observed sources compared to isotropy, a method referred to as *anisotropy study*.

From the perspective of high energy theorists, several approaches have been taken to determine the type of process responsible for acceleration to ultra-high energies. Anthony Hillas argued that if the cosmic ray accelerator behaves like a synchrotron, then the charged particles in its magnetic field will continue to accelerate until they reach sufficient energy to escape. For objects with known size and field strength, one can estimate the maximum achievable energy by applying the requirement that the Larmor orbit of a charged particle in an accelerator be smaller than the size of the accelerator,  $R_s$ . That is,

$$E_{\max} = \Gamma Z B e R_s. \quad (1.2)$$

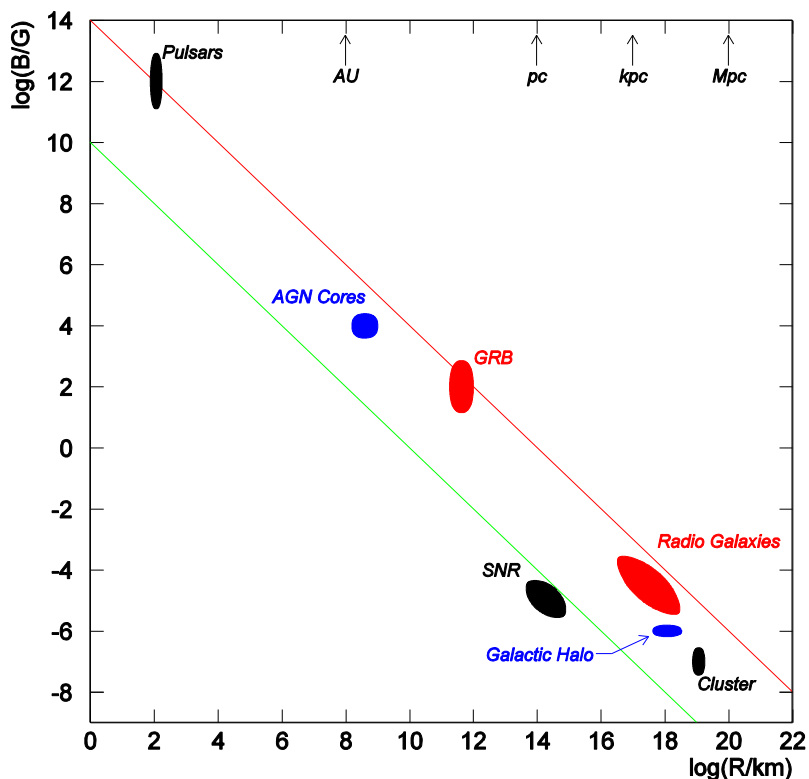


**Figure 1.2** Hillas plot showing potential UHECR sources (adapted from [9]). The source classes are plotted according to their characteristic magnetic field strength and size. The red line follows the energy density required to accelerate a proton to  $10^{21}$  eV, green for iron.

Figure 1.2 is a so-called “Hillas plot”, where potential sources are plotted according to their size and magnetic field strength. The red line corresponds to the energy of a  $10^{21}$  eV proton and the green line for a  $10^{21}$  eV iron nucleus. The most likely candidates appear near the center of this figure, because cosmic rays accelerated by sources that are small will tend to lose much of their energy to synchrotron radiation. Those accelerated by sources that are very large will spend more time accelerating and hence have more opportunity to interact with the CMBR. As the figure shows, gamma ray bursts (GRBs) and radio galaxies are the most probable candidates for proton sources while AGN cores and the galactic halo are candidate sources for iron.

## 1.4. First-Order Fermi Acceleration

Regardless of the type of source, the driving force is best described by Fermi shock acceleration [10]. Consider the encounter between a strong planar shock wave and a large magnetic cloud as shown in Figure 1.3. The shock wave travels with velocity  $\beta = v_s/c$  and the average velocities of the gas downstream and upstream from the wave are  $v_1$  and  $v_2$ , respectively. Let  $v_1 < v_2 < v_s$  and  $v_s \ll c$ . Now consider a cosmic ray particle carrying energy  $E_1$  entering the cloud. Lorentz transformation to a reference frame moving with the shock front gives,

$$E'_1 = \gamma E_1 (1 - \beta \cos \vartheta_1) \quad (1.3)$$

with  $\gamma = 1/\sqrt{1 - \beta^2}$ . After encountering the shock front, it will have energy,

$$E_2 = \gamma E'_2 (1 + \beta \cos \vartheta'_2). \quad (1.4)$$

No energy is transferred between the cosmic ray and the cloud and the collision with the shock front is assumed to be purely elastic, so  $E'_2 = E'_1$  and the particle's energy increases by,

$$\xi = \frac{E_2 - E_1}{E_1} = \frac{1 - \beta \cos \vartheta_1 + \beta \cos \vartheta'_2 - \beta^2 \cos \vartheta_1 \cos \vartheta'_2}{1 - \beta^2} - 1. \quad (1.5)$$

The average increase is found by averaging over the direction cosines.

$$\langle \cos \vartheta_1 \rangle = \int_0^{2\pi} \cos \vartheta_1 \frac{dn}{d\cos \vartheta_1} d\Omega \bigg/ \int_0^{2\pi} \frac{dn}{d\cos \vartheta_1} d\Omega. \quad (1.6)$$

In the presence of a planar shock wave, the cosmic rays must all leave the cloud on the same side of the wave that they arrived. That is,

$$\frac{dn}{d\cos \vartheta_1} = \begin{cases} 2\cos \vartheta_1, & \cos \vartheta_1 < 0 \\ 0, & \cos \vartheta_1 > 0 \end{cases} \quad (1.7)$$

and,

$$\frac{dn}{d\cos \vartheta'_2} = \begin{cases} 0, & \cos \vartheta'_2 < 0 \\ 2\cos \vartheta'_2, & \cos \vartheta'_2 > 0 \end{cases} \quad (1.8)$$

leading to  $\langle \cos \vartheta_1 \rangle = -\frac{2}{3}$  and  $\langle \cos \vartheta'_2 \rangle = +\frac{2}{3}$ . Plugging this result into Equation (1.7) and dropping terms which are quadratic in  $\beta$  yields,

$$\langle \xi \rangle \approx \frac{4}{3}\beta. \quad (1.9)$$

On average, the increase in the cosmic ray's energy after each encounter with the shock wave is proportional to the shock front's velocity, hence the name "first-order" Fermi acceleration.

If the cosmic ray is trapped in the magnetic cloud then it may have multiple encounters with the shock front. After  $n$  encounters, its energy will be,

$$E_n = E_0(1 + \langle \xi \rangle)^n. \quad (1.10)$$

Between each encounter, however, there is a probability the particle will escape,  $p_n$ , which will be a monotonically increasing function of  $E$ . The probability of finding a cosmic ray with energy  $E_n$  leaving the cloud is then,

$$P(E_n) = p_n \prod_{k=0}^{n-1} (1 - p_k). \quad (1.11)$$

If the escape probability was a constant equal to  $1 - \epsilon$ , then the ratio of cosmic rays with different energies will be given by,

$$\frac{N_n}{N_0} = \prod_{k=0}^{n-1} \epsilon = \epsilon^n \quad (1.12)$$

and the differential cosmic ray energy spectrum will follow a power law that is proportional to the probability of containment by the accelerator and the average energy increase per encounter with the shock front,

$$\frac{N_n}{N_0} = \left( \frac{E_n}{E_0} \right)^\gamma, \quad \gamma = \frac{\ln \epsilon}{\ln(1 + \langle \xi \rangle)} \quad (1.13)$$

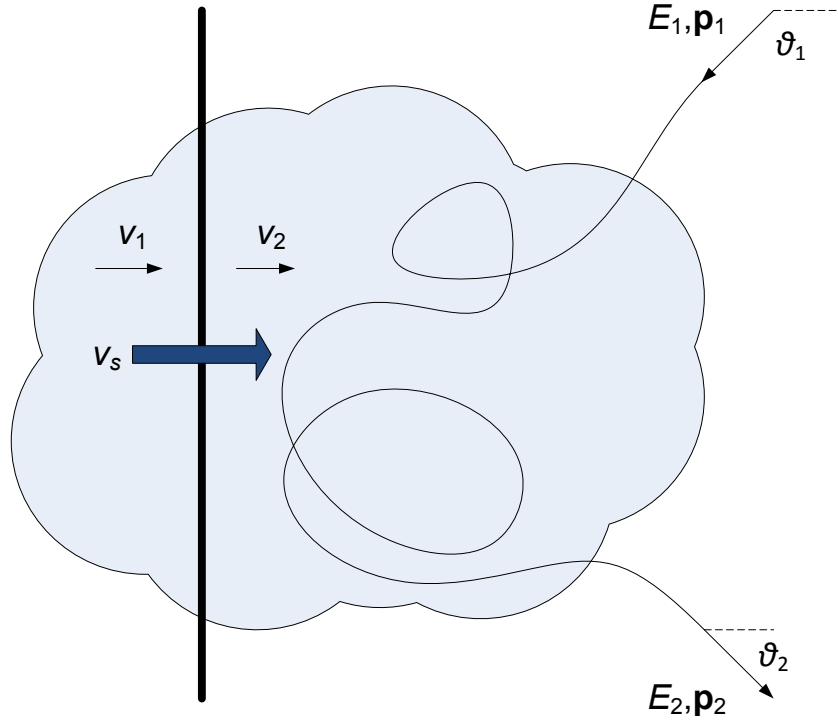
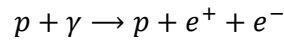


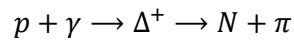
**Figure 1.3** Magnetic abnormality in the presence of a strong planar shock wave [9].

## 1.5. UHECR Propagation

Cosmic ray protons are subject to three major energy loss mechanisms during their transit to Earth; adiabatic losses due to the expansion of the universe, synchrotron radiation and pion production. Each mechanism has a different relative impact, depending on the energy of the primary. Only the relative loss due to redshift is independent of energy,  $(dE/dt)/E = -H_0$ . The cross section for electron-positron pair production, given by the reaction,

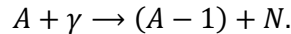


has a lower threshold than that for pion production, but occurs much more frequently. At threshold, this process produces an energy loss of only  $2m_e/m_p$ . Pion production is the theoretical basis of the so-called GZK limit, has a very strong impact on cosmic ray energies, but only affects protons with energies above  $10^{19.6}$  eV in the reaction described by,



where  $N$  may be a proton or neutron [8]. The  $\pi$  will either be positively charged or neutral, depending on the nucleon it is paired with. In this case, the threshold energy loss is the ratio,  $m_\pi/m_p$ .

Iron nuclei are subject to energy loss by photodisintegration according to the reaction,



To a lesser extent, their energy is additionally attenuated by the CMBR due to the giant dipole resonance, leading to a suppression of iron cosmic rays above  $8 \times 10^{19}$  eV [9].

By the time they have reached the Earth, UHECRs will have spent (relatively) little time within our galaxy. The primary influence on cosmic ray propagation, locally, will be the GMF. According to Alvarez-Muñiz and Stanev, “the gyroradius of a  $10^{18}$  eV proton is 300 pc, the typical thickness of the galactic disk” [9]. So isotropy should be expected in UHECRs with energies below this level.

## 1.6. The Extensive Air Shower

When a cosmic ray collides with Earth’s atmosphere with enough energy, a cascade of secondary particles called an *extensive air shower* (EAS) is created. After the initial interaction, hundreds to thousands of high energy particles are produced. These subsequently collide with other molecules in the atmosphere and the chain reaction continues until the per-particle energy is insufficient to sustain the shower and the remaining particles decay or are absorbed.

Typically, the initial interaction produces neutral pions and both positively and negatively charged pions in roughly equal numbers. Neutral pions quickly decay into gamma ray pairs, each subsequently producing electron-positron pairs. This component of the EAS is known as the electro-magnetic component and is responsible for producing the fluorescence light. Charged pions have significantly longer lifetimes than their neutral counterparts. They form a highly col-

limited beam along the trajectory of the primary particle and are responsible for propagating the air shower in the component referred to as the “hadronic core”.

Some of the charged pions manage to decay into muon-neutrino pairs. Muons also lose energy to local ionization energy deposit and, like the electrons and positrons, are responsible for producing some of the air shower fluorescence. In a typical EAS, electrons and positrons vastly outnumber muons and are responsible for 97-98% of the total ionization energy deposit near shower maximum [12]. The neutrinos carry away energy which will never be detected. This *missing energy* is more significant high in the atmosphere, where charged pions are more likely to decay before colliding with atmospheric matter. Because, by definition, missing energy is not observed, we must rely on cosmic ray interaction models to determine how much must be accounted for, depending on the *calorimetric energy*, i.e. the energy which is transferred from the secondary cosmic rays to atmospheric matter via ionization and particle decay processes.

In 1977, Thomas Gaisser and Michael Hillas suggested that the number density of charged particles in an EAS as a function of atmospheric matter traversed take the form [13],

$$N(X) = N_{\max} \left( \frac{X - X_0}{X_{\max} - X_0} \right)^{\frac{X_{\max} - X_0}{\Lambda}} e^{-\frac{X - X_{\max}}{\Lambda}} \quad (1.14)$$

where  $N_{\max}$  is the maximum number of charged particles present in the shower,  $X_{\max}$  is the amount of atmosphere crossed when the shower reaches its peak,  $X_0$  represents the depth of first interaction and  $\Lambda$  is the shower width parameter, related to the characteristic interaction length of the particles in the shower. All of the variables except  $N_{\max}$  carry units of  $\text{g}/\text{cm}^2$ . All four parameters to some extent depend on the energy of the primary particle. It turns out that some also depend on the primary particle type as well.

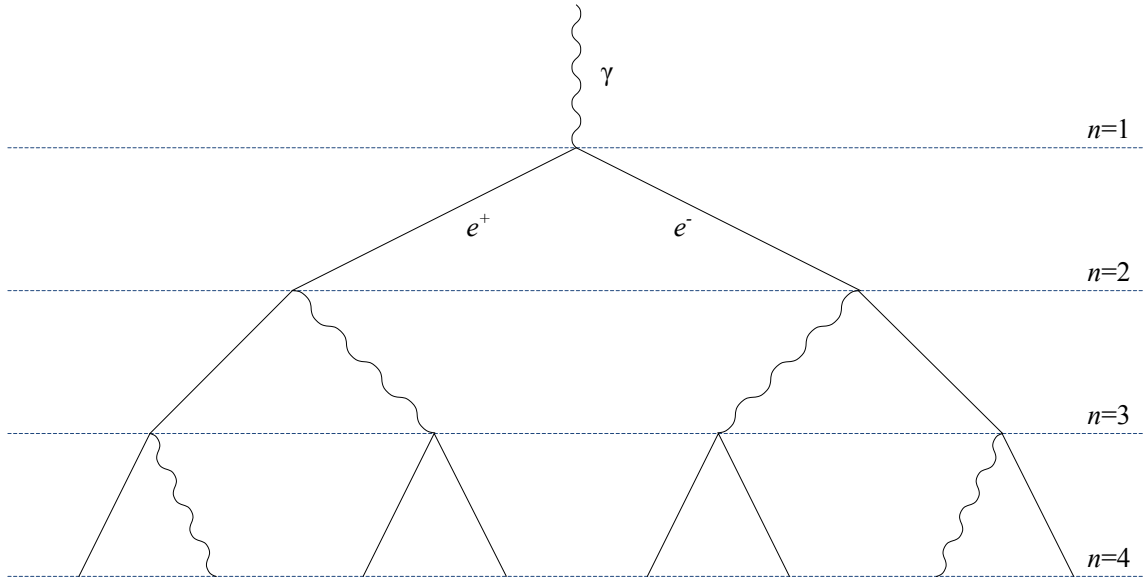


**Figure 1.4** Schematic of the Heitler toy model EM cascade, reproduced from Matthews [14].

Figure 1.4 is a representation of the EM cascade model described by Heitler in 1954, adapted from [14]. A photon enters with energy  $E_0$  and produces an electron-positron pair each with energies  $E_0/2$ . After some interaction length  $\lambda$ , the electron or positron produce a bremsstrahlung photon which carries away half of its kinetic energy. The new photons subsequently produce another  $e^+e^-$  pair, thus propagating the cascade. This process continues until the energy per particle reaches some threshold energy  $E_c$  below which no more collisions can occur. After  $n$  interactions, there will be  $N_n = 2^n$  particles and photons, each carrying energy  $E_n = E_0 2^{-n}$  and the shower will have reached its peak when  $E_n = E_c$ . The number of interactions needed to occur to get to the peak is  $n = \ln(E_0/E_c)/\ln 2$ , leading to the following relationship between  $N$  and  $E_0$ ,

$$N = \frac{E_0}{E_c}. \quad (1.15)$$

In the Heitler model, the number of particles present in the cascade is proportional to the primary energy and the “depth” of the peak is then,

$$n\lambda = \lambda \ln \frac{E_0}{E_c}. \quad (1.16)$$

Hence, there is a logarithmic dependence between the depth of the shower maximum and primary energy.

Now consider a situation where the primary particle consists of  $A$  nucleons that break apart immediately after the initial interaction, so that,

$$E_1 \approx \frac{E_0}{A}, \quad N_1 \approx A \quad (1.17)$$

given the same interaction length. Naturally, this will require fewer interactions before the shower maximum is reached. We have  $n = \ln(E_0/AE_c)/\ln 2$ ,  $N = A \cdot E_0/AE_c = E_0/E_c$  and  $n\lambda = \lambda \ln(E_0/AE_c)$ . Therefore, the depth of shower maximum depends logarithmically on the number of nucleons in the primary. However, the maximum number of particles does not depend on the number of nucleons in the primary at all.

So it should be expected that the parameters in Equation (1.14), named the Gaisser-Hillas formula, should have the following dependencies on primary particle energy  $E_0$  and nucleon number  $A$ ,

$$N_{\max} \propto E_0, \quad X_{\max} \propto \log \frac{E_0}{A}. \quad (1.18)$$

The depth of the initial interaction will certainly depend on the primary particle species. It is sometimes assumed that all cosmic ray primaries are either protons or iron nuclei and, obviously, iron nuclei have much larger cross sections and will tend to have smaller  $X_0$ , a parameter which will also depend on primary energy. This dependence is complex and will be described in more detail in Chapter 4. The shower width parameter,  $\Lambda$ , also has a complex dependence on primary particle species and energy. Additionally, it depends on altitude so it is not even constant throughout the shower. Fortunately, it doesn't change very much so it is usually sufficient to treat it as a constant. Again, this is discussed with more detail in a later chapter.

## Chapter 2. The Telescope Array Project

### 2.1. Experiment and Apparatus

Telescope Array (TA) is an international collaboration with more than 120 members representing 26 institutions. The experiment is situated in the high desert of central Utah, 200 km southwest of Salt Lake City near the town of Delta. It consists of 38 fluorescence detectors (FDs) divided into three observation stations overlooking an array of 507 surface detectors (SDs). Middle Drum (MD) station sits to the north and houses 14 FDs utilizing refurbished hardware from the HiRes experiment. The Black Rock Mesa (BRM) and Long Ridge (LR) stations each contain 12 newly-built FDs outfitted with FADC electronics systems [15].

The SD array is arranged in a square grid with 1.2 km spacing, yielding a total coverage area of 680 square kilometers. Each SD contains two layers of plastic scintillator, each 3 m<sup>2</sup> by 1.2 cm in size. The light emitted as charged particles pass through the scintillators is passed to PMTs via fiber-optic cable and the signal processed with an on-board data acquisition system. They are independently powered by an on-board battery and solar panel. To optimize communication between the SDs and the control computer in Delta, the array is divided into three regions and the SDs transmit their digitized signal to the communication tower corresponding to its region. The signal is subsequently sent to the control computer via microwave radio.

The FDs measure the calorimetric energy deposit of extensive air showers by collecting the fluorescence light produced as charged particles ionize nearby nitrogen atoms. Functionally, they are telescopes, each consisting of a segmented spherical mirror projecting onto an array of photomultiplier tubes (PMTs). The telescopes' viewing directions are fixed and designed so each PMT views one degree of solid angle in the sky. In each observation station, the FDs are arranged in a *two-ring* configuration, with one group of telescopes viewing elevations from 3° to

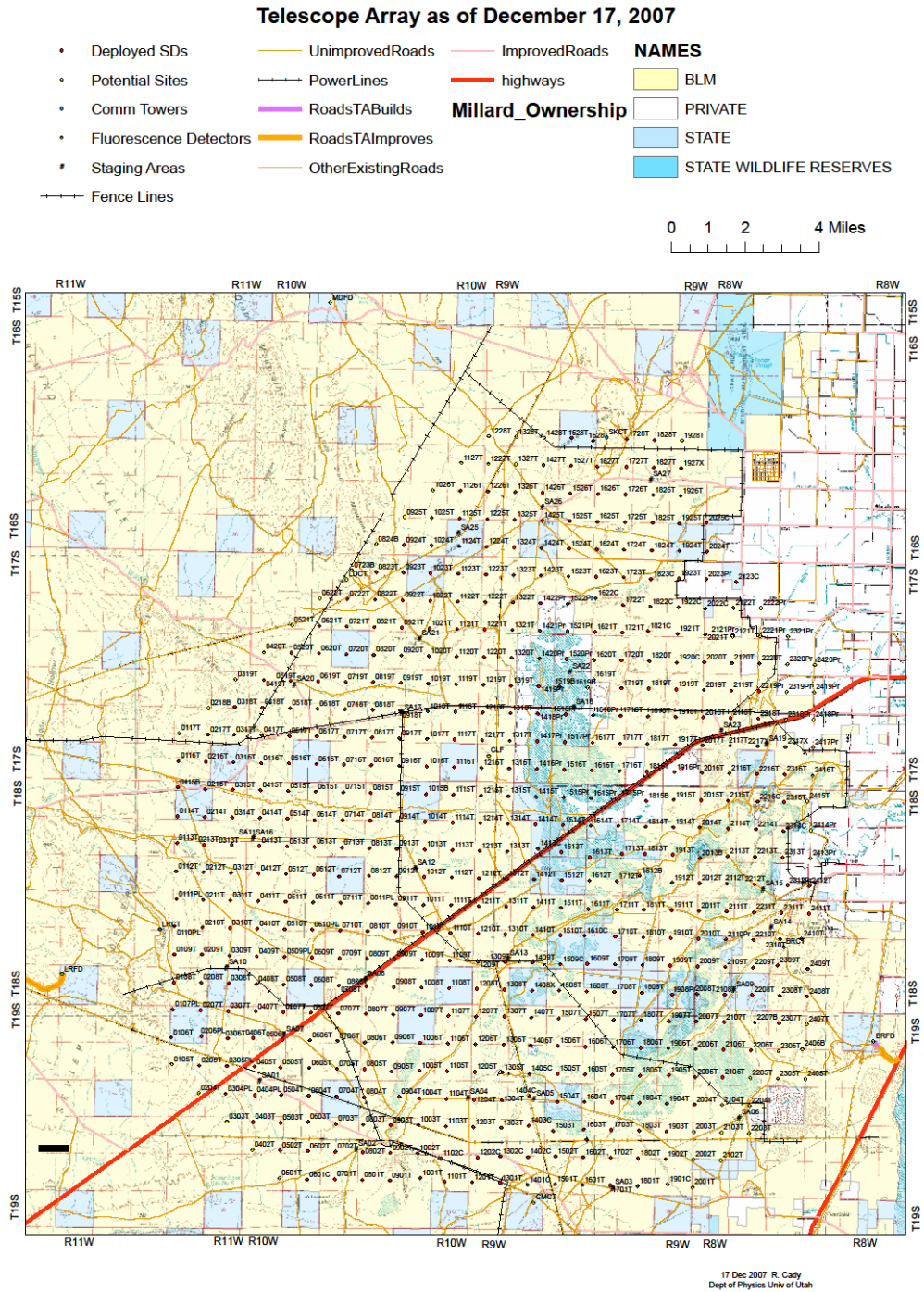


Figure 2.1 Political map of the Telescope Array Experiment [16].

17° (ring 1) and the other from 17° to 31° (ring 2), both covering a total of  $\sim 110^\circ$  in azimuth.

In “hybrid” mode, when data from two or more detector classes is combined, independent measurements of the cosmic ray air shower position and longitudinal development is achieved, yielding high-precision energy and geometry measurements. The detectors may also be cross-calibrated, so even in *monocular* mode, when data from only one detector class is considered, the precision in energy estimation is still improved. The focus of this thesis is on the analysis of data collected from BRM and LR stations in monocular mode.

## 2.2. The FADC Fluorescence Telescopes

The BRM and LR observation stations are identical in design, each housing 12 FDs organized into three bays of four telescopes. Within each bay, the telescopes are arranged with crossing fields of view, where the ring 1 FDs are physically stacked on top of the ring 2 FDs. Each FD’s mirror consists of 18 individual segments offering a total light collection area of 6.8 square meters. Each segment is formed from a 10.5 mm thick sheet of borosilicate glass which is given a spherical curvature through a process called *slumping*. In the slumping process, each glass segment is laid onto a convex ceramic slab, which has been milled to the desired radius of curvature. The glass is heated in an electric oven while a vacuum is applied, causing the glass to conform to the slab’s surface. A 200 nm thick layer of aluminum is then applied by vacuum deposition followed by a 50 nm layer of aluminum oxide ( $\text{Al}_2\text{O}_3$ ) by anodization. The aluminum oxide layer not only forms a protective coating, but the thickness “tunes” the optimum wavelength of reflected light. A thickness of 50 nm was selected to maximize reflectivity of 350 nm light. Before installation, the segments measured greater than 90% reflectance for wavelengths between 300-400 nm. The mirror radii of curvature are all within 30 mm of design specification (6067 mm). The optical quality of a mirror segment is gauged by its *spot size*, the radius of a circle con-

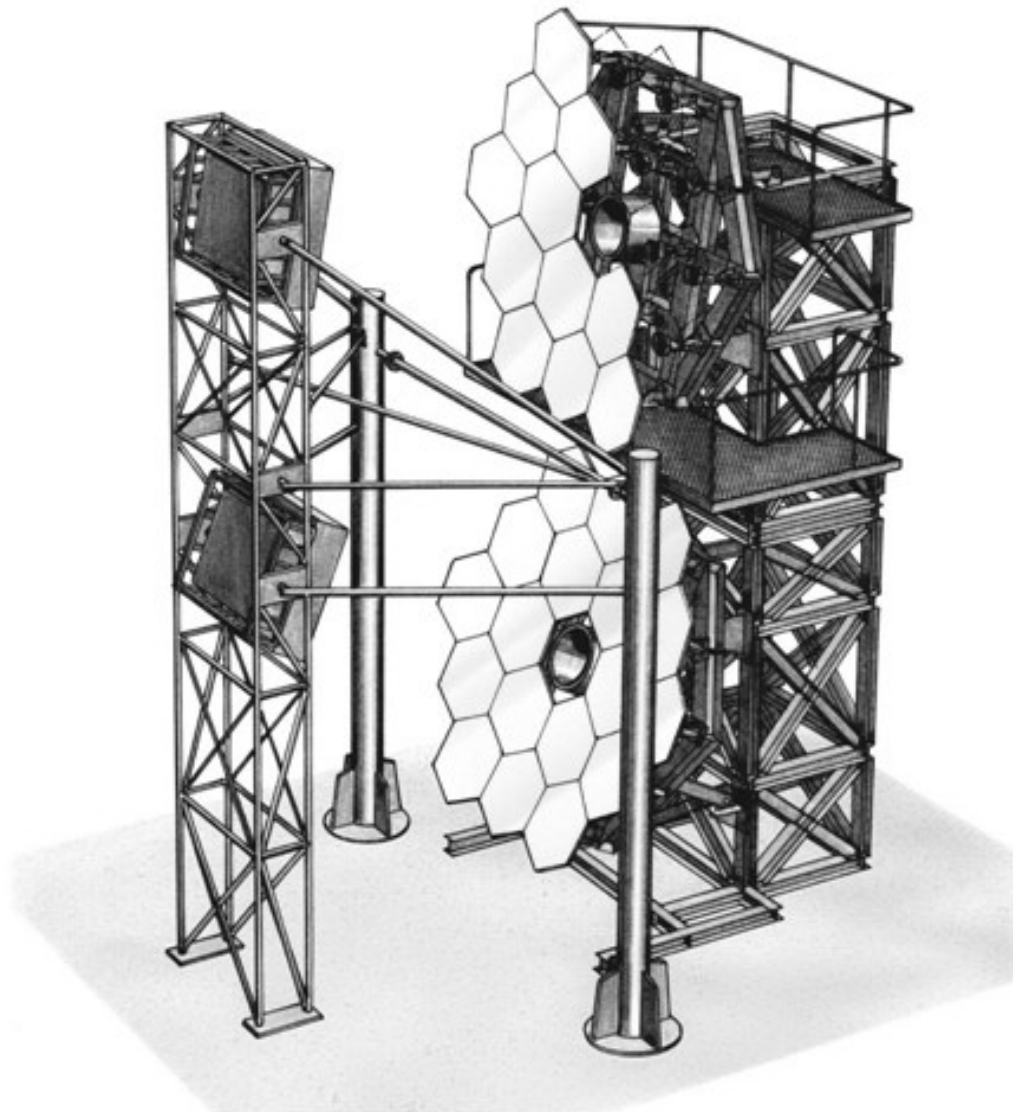


**Figure 2.2** Schematic of a fluorescence telescope ring 1/ring 2 pair. Seven segments have been removed from the top mirror to reveal the support structure [17].

taining 90% of the reflected light from a point source placed at its center of curvature. For the mirror segments of the FADC FDs, this is typically  $12 \pm 3$  mm [17].

Each camera contains 256 hexagonally close-packed PMTs with 60 mm spacing. Together, the PMTs form a flat focal plane set 300 cm from the mirror center. Due to spherical aberration, the size of the projection of a point source will be different near the edge of the camera than it would be near the center. Ray tracing simulation studies show that, given a 300 cm focal length and 85% mirror reflectance, a segment radius of curvature of 6067 mm would optimize

EAS event reconstruction, yielding a spot size smaller than 40 mm at the focal plane [17]. The cameras are independently connected to their own electronics rack via 25 m long cables. One set of cables supplies HV to the individual PMTs and another set carries the signal to the data acquisition system (DAQ). The electronics racks are situated next to each other in a single, air-conditioned room isolated from the telescope bays.

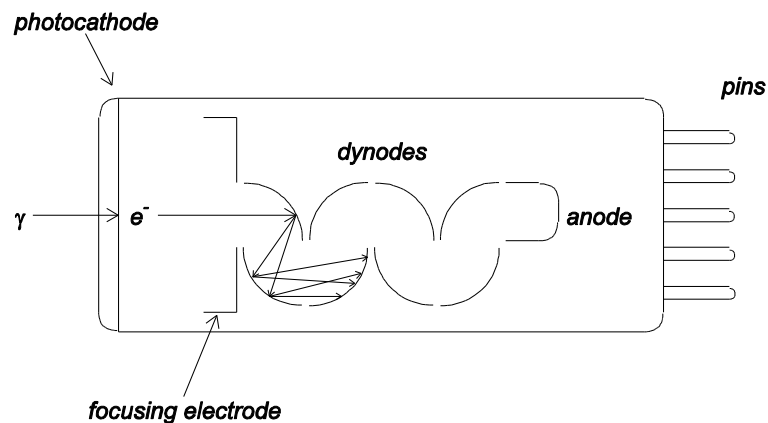


**Figure 2.3** Basic components of a photomultiplier tube.

### 2.3. Photomultiplier Tubes

The FADC telescopes use Hamamatsu R9508 photomultiplier tubes (PMTs). They were custom-made for Telescope Array and designed for “photon-counting” experiments, meaning they have been optimized for extreme low-light applications. They have borosilicate windows coated with a bialkali photocathode, which ejects an electron when struck by a photon via the photoelectric effect. These PMTs use a linear dynode structure similar to the example shown in Figure 2.3 where the dynodes, photocathode and anode are all held at different voltages. As electrons are ejected from the photocathode, they are drawn to the first dynode by the potential difference. After collision with the first dynode, more electrons are ejected and drawn to the second dynode. The multiplication continues until there are roughly 105 electrons reaching the anode for every electron that strikes the first dynode.

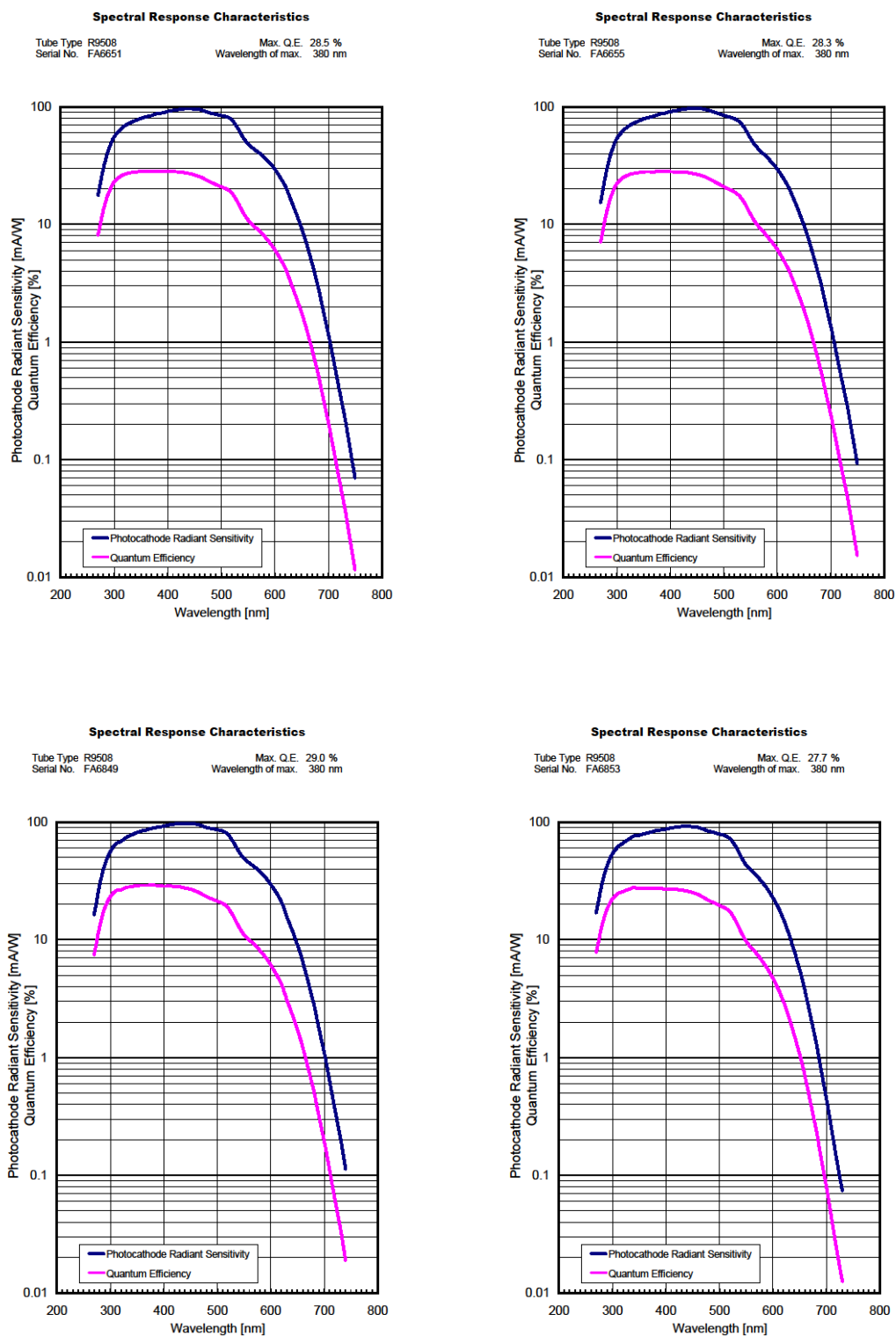
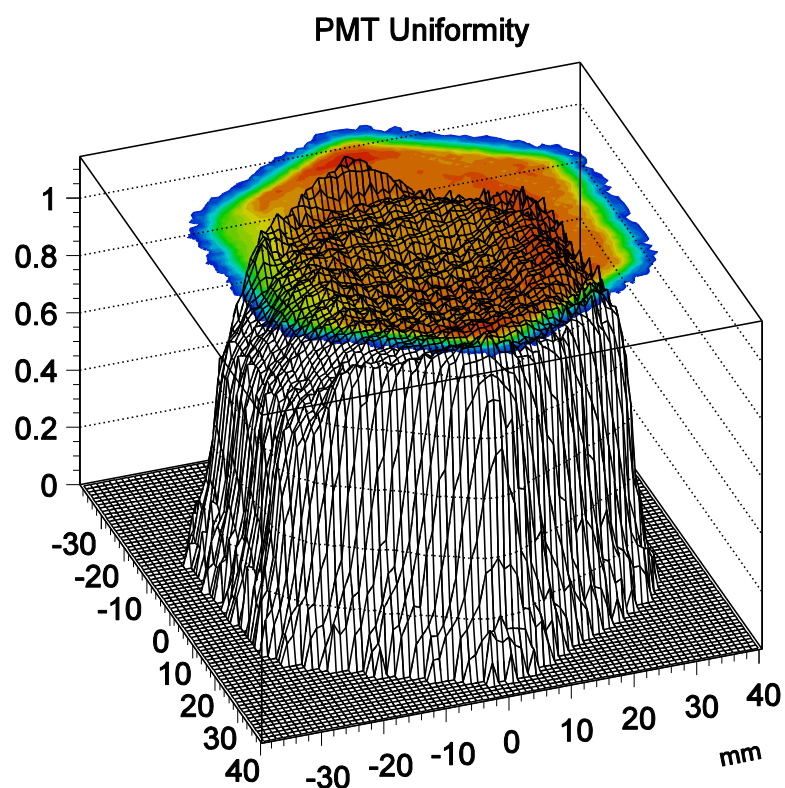


Figure 2.4 Example QE measurements from four photomultiplier tubes [18].

Some of the intrinsic properties of the PMTs have major implications on the measurement of fluorescence light. The most significant is the quantum efficiency (QE), which is the ratio of electrons ejected from the photocathode to number of incident photons. Sometimes the ejected electron misses the first dynode or else doesn't result in the ejection of any secondary electrons. This loss factor is accounted for in the PMT's collection efficiency (CE). Sometimes this factor is folded into the tube's overall QE or given the label QECE to indicate the combined effect. High-precision measurements of PMT QE and CE are crucial for understanding the relationship between the observed signal and the number of photons it took to produce it.



**Figure 2.5** PMT uniformity map. The  $x$  and  $y$  axes are in mm,  $z$  axis is scaled so all entries within 18mm from the center average unity.

Because of QE and CE, PMTs are sensitive to the wavelength and position of the incident light. QE is related to the chemistry of the photocathode, so it is primarily wavelength-dependent. Before shipment, Hamamatsu measured the QE profiles of 32 PMTs, three of which

are shown in Figure 2.4. To some extent CE has to do with the chemical properties of the dynodes, but it is mainly a measurement of how efficiently the electrons travel from the photocathode to the first dynode and is therefore geometry-dependent. Average measures of CE for each of the 32 PMTs were supplied by the manufacturer, but careful scans of their acceptance as a function of position of incident light were taken. The average of these measurements form what is called the PMT uniformity map, shown in Figure 2.5 [19].

Special narrow band UV-transparent filters called BG3 filters are glued to the front of each PMT. These filters use a special formula which only allows light in the wavelength range of 290 to 410 nm, covering the transition lines of nitrogen fluorescence.

## 2.4. The Signal Digitizer/Finder and Track Finder

Each camera has 16 signal digitizer/finder modules (SDF) which continuously monitor the PMTs, looking for significant signals above background. Each module uses 16 AD9224 FADC chips operating at 40 MHz, one for each of the attached PMTs. This particular model of FADC chip has two input voltage pins, labeled  $V_{INA}$  and  $V_{INB}$ . The chip generates a 12-bit number based on the difference between these voltages using the scale set by the reference voltage,  $V_{REF}$  [20]. The FADC can resolve a signal within 25 nanoseconds, but the typical signal received by a single PMT from an air shower is on the order of several microseconds and it is therefore unnecessary to view the signal with such high resolution. To improve signal-to-noise and reduce the size of the raw data, the SDF sums the FADC digitizations four at a time, producing 14-bit time series data effectively operating at 10 MHz.

To determine if a channel received signal from an air shower, the data are divided into sequences of 256 samples called *frames*. Within a frame, sums of 16, 32, 64 and 128 bins are compared to a threshold value, determined by the threshold generator component in the SDF. The threshold generator monitors the background mean and variance, averaged over four long

sample windows in parallel, and computes a threshold value in number of FADC counts, corresponding to a significance of  $6\sigma$ . A tube is considered “hit” if any one of the four sums is above threshold. If the PMT is not hit, then the frame advances by 128 samples and performs another scan overlapping the previous scan by half a frame [21].

The track finder (TF) module scans sub-matrices of tubes and compares patterns of hit PMTs to lookup tables programmed in the FPGA memory bank. If five adjacent hit tubes are found in a  $5 \times 5$  sub-matrix (Figure 2.6), then the TF issues a code 1 trigger to the central timing and distribution (CTD) computer and a station-wide trigger command is issued, where the PCs for every camera are instructed to dump the FADC buffers from all channels to disk. A station-wide trigger command may also be sent if two adjacent cameras report a code 2 trigger, where three adjacent hit tubes are found in a  $4 \times 4$  sub-matrix along the edge of the camera (Figure 2.7). The tubes and cameras are synchronized, so a specific index in the time series from one waveform corresponds to the same time period in every channel of every camera at that FD station. The buffers include the frame where the trigger condition was satisfied plus 128 time slices before and after to ensure the entire shower track was captured.

Figure 2.9 is the data flow diagram for the FD trigger electronics, adapted from [22]. The pulse produced from the PMT for each photo-electron is essentially a delta function, with 95% of the signal occurring within 10 ns. The signal from the PMT is sent directly to a pre-amplifier then the camera’s patch panel. Sixteen sets of 16 twisted pair cable bring the signal 25 m from the camera to the differential receiver in the VME crate. Because the signal from a single PE is smaller than the sampling rate of the FADC (25 ns), a 2<sup>nd</sup> order Butterworth filter with a 50 ns RC constant is used as an anti-aliasing filter (the shaper circuit).

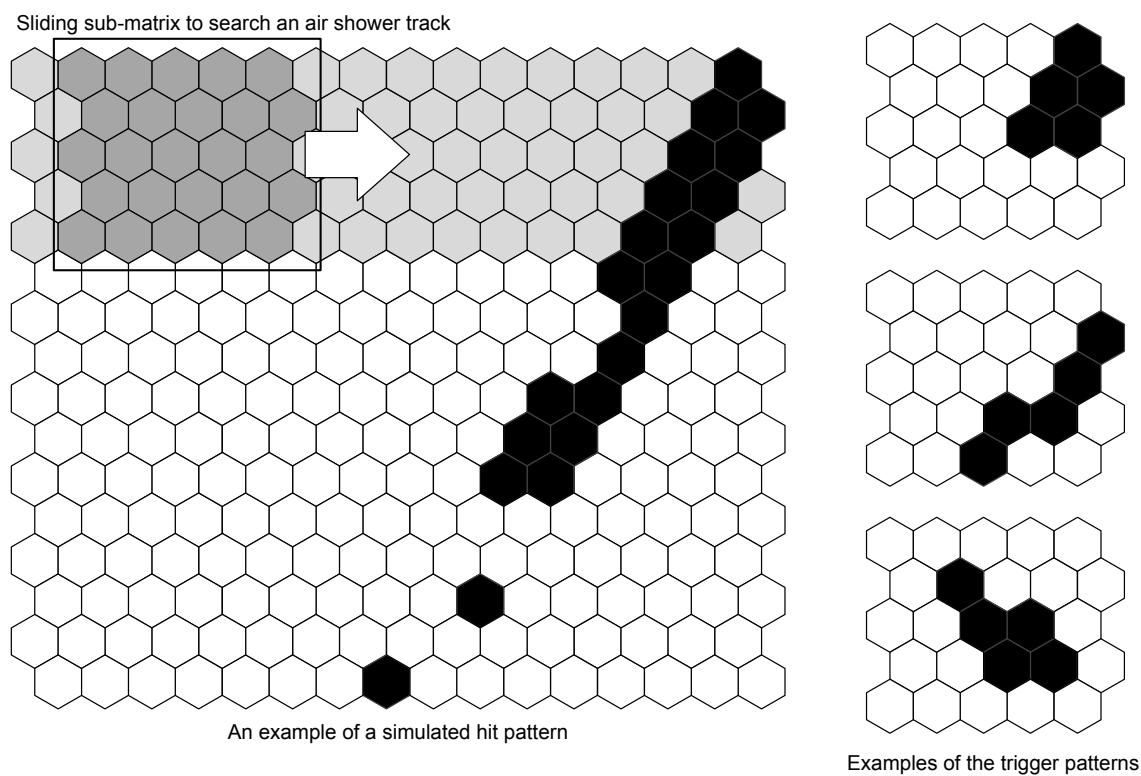


**Figure 2.6** Schematic diagram of the track finding process [21].

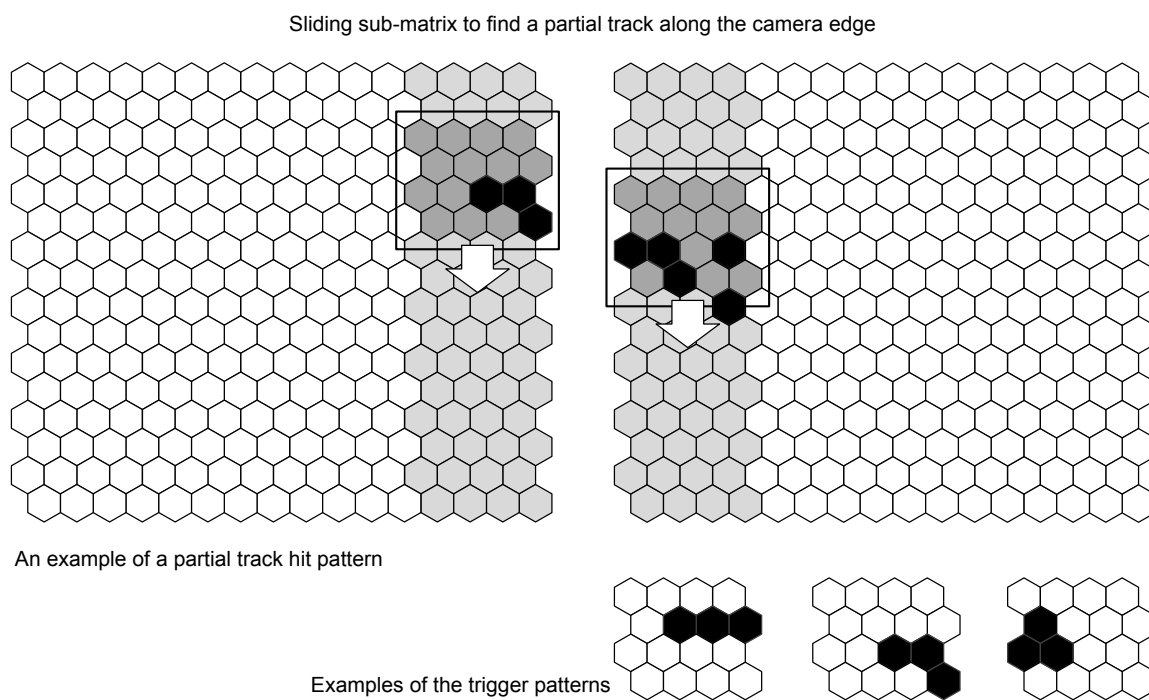


**Figure 2.7** Schematic diagram of the partial track search near the boundary of a camera [21].

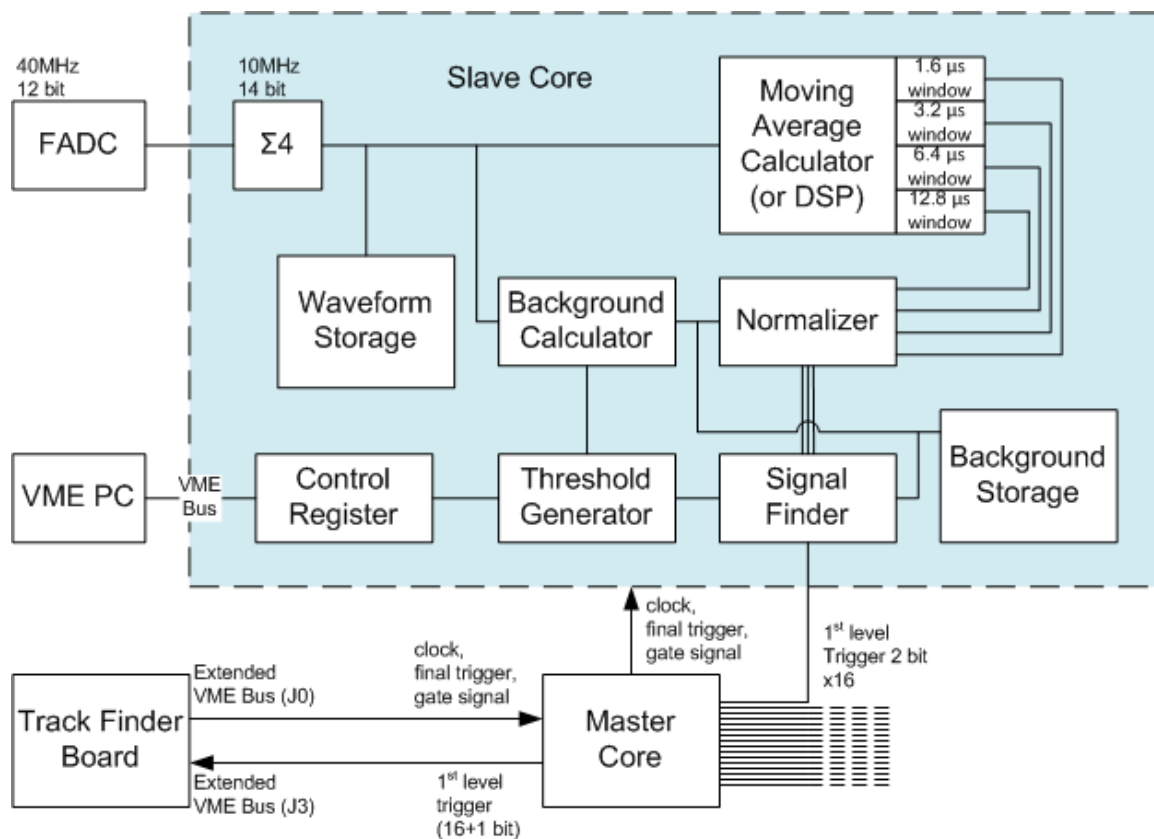


Figure 2.8 SDF Flow Chart [22].

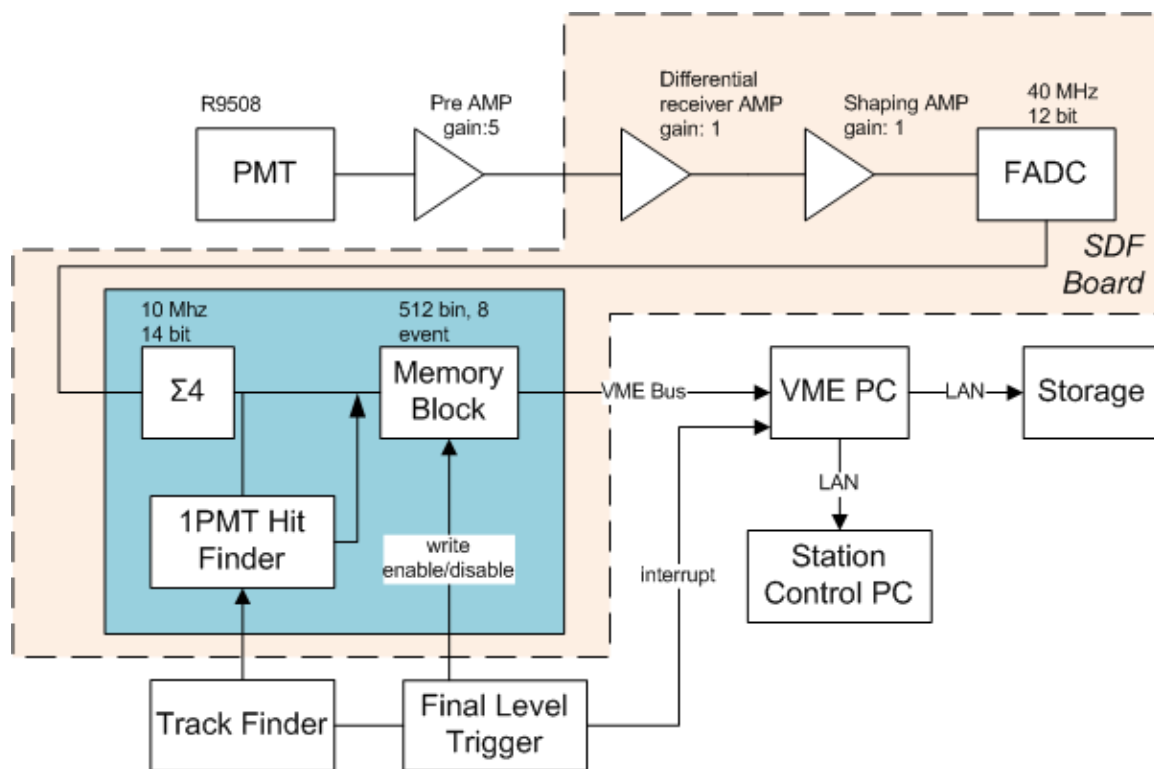


Figure 2.9 FADC FD Data flow chart [22].

## 2.5. Detector Calibration

The analysis of fluorescence data hinges on the ability to translate ADC counts in the raw data into numbers of photons. It is insufficient to assemble a simple list of conversion factors for the photomultipliers, simply because they are not constant. As described in Section 2.3, a photomultiplier works by generating a small electrical pulse when a photon strikes its photocathode. The probability that a pulse will be generated from that photon depends on the tube's QE, which adds wavelength dependence, and CE, which adds position dependence. The size of the signal depends on the tube's *anode gain*, the ratio of number of electrons at the anode to the number ejected from the photocathode, which adds temperature dependence. Additionally, QE tends to decrease over time due to long-term degradation of the photocathode. In an experiment with an estimated lifetime of 10 or more years and 6,144 PMTs between the two FD stations, a complex system is required to test and maintain detector calibration.

The fluorescence detectors are calibrated with a system which uses camera temperature, hourly xenon flasher runs, periodic roving flasher tests and a tiny scintillator unit called a YAP. Through this system, a database is computed with hourly estimates of individual PMT gains, the product of an absolute calibration constant ( $g_0$ ) and four corrections ( $g_{1-4}$ ). Here, *gain* is defined as the number of ADC resulting from a 337 nm photon incident on the photocathode. To control the sources of systematic error, the units of ADC per photon are kept entirely in the first factor,  $g_0$ , while all other terms are unity if no correction is needed.

It would be prohibitive to measure an absolute calibration for all six thousand tubes. Instead, 52 highly calibrated PMTs are distributed throughout the cameras. This special calibration was done using a system called CRAYS, detailed in Section 2.6. Every camera has at least two CRAYS tubes; one near the center of the camera (position 0x77) and one part-way to the corner

$g_0$	<b>Absolute Calibration Constant</b> – For the highly-calibrated tubes, this is the gain measured by CRAYS. For the remaining tubes, this is the measurement relative to the CRAYS tubes after HV adjustment.
$g_1$	<b>Geometry Correction</b> – Accounts for the difference in light each tube receives from the XF due to their physical location.
$g_2$	<b>XF Correction</b> – Correction based on the comparison between run-time XF data and the results from the HV adjustment period.
$g_3$	<b>YAP Correction</b> – Correction for long-term photocathode degradation, using YAP data.
$g_4$	<b>Temperature Correction</b> – Correction using the typical dependence of gain on temperature of $-0.72\%/^{\circ}\text{C}$ .

**Table 2.1** The PMT gain correction factors.

(position 0x33). Cameras 00 and 06 of each station have a third one installed in position 0xB3.<sup>1</sup> Once installed, the HV supplied to the other tubes in each camera is adjusted until they all produce the same size signal when illuminated by a xenon flasher.

The xenon flashers (XFs) used here are small devices mounted at the center of each mirror and pointed directly toward the cameras. Each has a 355 nm narrow-band filter and Teflon diffuser to produce a smooth distribution of monochromatic light. During HV adjustment, these are operated with the mirrors covered to eliminate *splash-back* effects, where light reflected from the Paraglas dust cover gets reflected back from the mirror. After the tubes' gains are matched, the XFs are run with the mirror covers removed to measure the amount of splash-back seen by each PMT. The XFs are run on an hourly basis during regular observation periods to monitor the time progression of gain drift. Of course, the mirrors cannot be covered in this case, so the XF data must be corrected for splash-back according to the measurements taken during HV adjustment.

Since the HV is adjusted to produce a flat ADC response to the xenon flasher and the tubes farther from the mirror-camera axis actually receive less light than the center channels, the gains of the outer channels will have been over-adjusted. The geometry correction factor,  $g_1$ ,

<sup>1</sup> Because the PMTs are placed in a 16x16 grid, specific channels may be identified by a two-digit hexadecimal number corresponding to their row and column placement (0x[*row*][*column*]). Channels may alternatively be identified by their decimal counterpart, so the '0x' prefix is used for clarity.

accounts for this geometric effect by applying a  $\cos^4 \theta$  factor to the total gain, where  $\theta$  is the angle between the mirror-camera axis and the line from the mirror's vertex to the center of the PMT. This correction is then scaled to one of the CRAYS tubes, specifically channel 0x77. The details of the origin of the  $\cos^4 \theta$  are provided in Appendix A.

Assuming constant HV, temperature variation has the most significant effect on tube gains. The CRAYS tubes' temperature dependence was measured before installation and found to be  $-0.72 \pm 0.053\%/^{\circ}\text{C}$  [23]. The correction factor  $g_4$  is computed from the average temperature dependence using the individual measurements of camera temperature, which are logged and saved in a separate database file. After correcting for the average temperature dependence, there will still be some variation from tube to tube, mainly due to the individual PMT's temperature dependence. This additional correction is calculated from the XF data and factored into  $g_2$ .

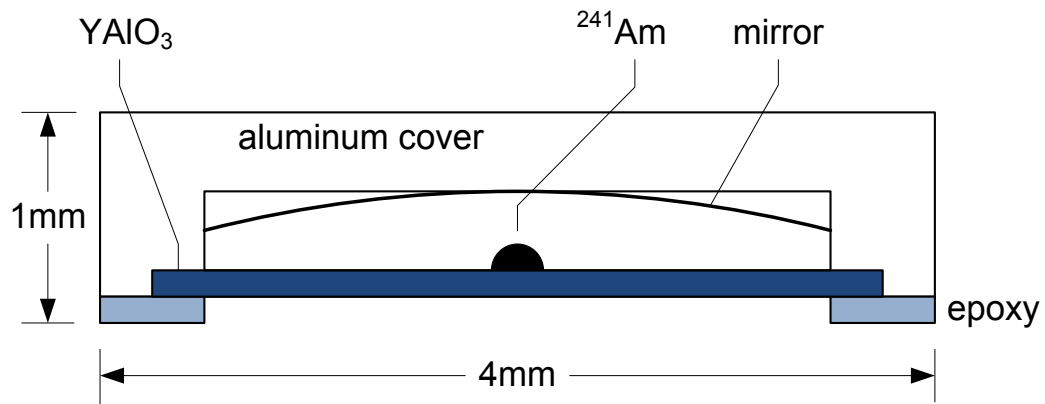


**Figure 2.10** Schematic of the YAP module [24].

On a time scale of years, PMT QE gradually decreases due to photocathode degradation, an effect which is accounted for by correction factor  $g_3$ . This is measured using a tiny yttrium aluminum peroxide scintillator (YAP). The YAP module is a small aluminum cylinder, 1 mm high and 4 mm in diameter and open at the bottom, as shown in Figure 2.10. Inside is a  $\text{YAlO}_3$  crystal scintillator and americium-241, which is an alpha source with a half-life of 242.2 years [25]. The mirror ensures that the emitted radiation passes through the YAP crystal. There is no

temperature dependency to the scintillator so when the  $^{241}\text{Am}$  decays, the same number of photons will be produced in the scintillator, regardless of environmental conditions. All of the CRAYS tubes have YAP modules installed on their BG3 filters.

## 2.6. CRAYS

Absolute calibration of the photomultipliers was done with a system called CRAYS, for “calibration with Rayleigh scattering”. The motivation for the technique is based on the results of Naus and Ubachs whose measurements of the Rayleigh scattering of nitrogen and argon using the cavity-ringdown (CRD) technique were within 1% of theoretical expectation [26]. The CRAYS apparatus, shown in Figure 2.11, is a cylindrical aluminum container with outlets for a vacuum pump, gas intake and windows for the laser beam and PMT. To minimize extra reflections, the inside is lined with black cloth and baffles are placed around the beam trajectory. Photodiodes are used to measure the beam intensity before and after it passes through the apparatus. A flipper is used to interrupt the beam and alternate between measurement of background levels and beam intensity. When the beam is passed through nitrogen gas, the scattered light is polarized because the gas is diatomic. This effect is measured by including a polarizer to switch between linearly and circularly polarized light and a  $\lambda/4$  retardation plate to change the polarization angle of linearly polarized light [27].

To be sure signal loss from the electronics is considered, the same cables and trigger boards used during CRAYS calibration are also used once the PMTs are installed. Furthermore, the calibration is done with the BG3 filter and YAP already installed. The PMT is positioned so its viewing direction is perpendicular to the beam line. A 36 mm diameter circular mask and a 40x10 mm rectangular slit are used to control the geometrical optics of the apparatus. The mask is placed directly in front of the PMT’s aperture and the slit is placed at the first baffle the scattered laser light passes from the beam line to the PMT. During calibration, the HV supplied to

the PMT is adjusted until the measured FADC arrives at some nominal value, corresponding to 2.3 337 nm photons per FADC count.

Since calibration of single photomultiplier tubes using CRAYS is intensive and time-consuming, it was only performed on a subset of 52 tubes. This also means these tubes are only calibrated once, since there is a risk of damage to other components and introduction of new systematic errors if certain tubes were to be extracted, re-tested, then re-installed. One of the purposes for the YAP calibration is to help account for the long-term changes in gain.

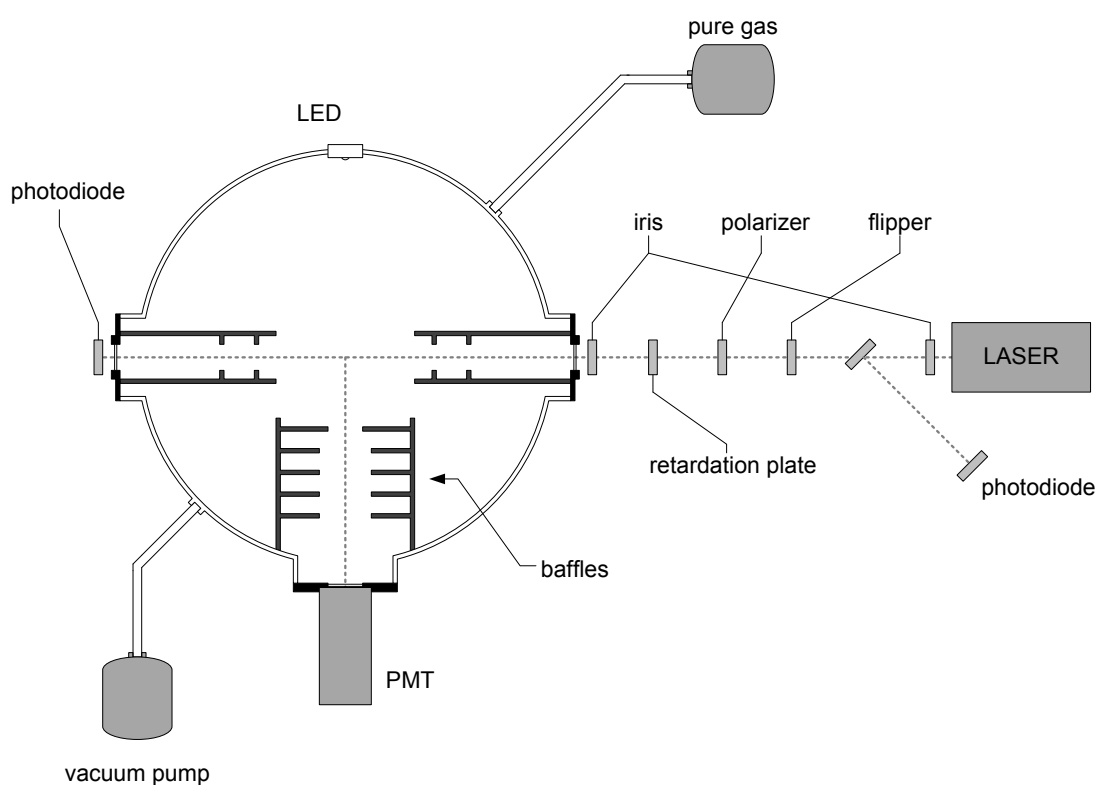


**Figure 2.11** Diagram of CRAYS apparatus. The laser beam is passed through a chamber with controlled atmosphere, perpendicular to photomultiplier field of view.

## Chapter 3. Data Analysis

Translating the information contained in the raw data into parameters that describe a cosmic ray air shower is a complex, multi-stage process. The atmosphere and the experimental apparatus involve phenomena that, even in the best circumstances, cannot be modeled exactly. At each processing stage, a careful decision is made to accept or reject data based on our understanding of these limits. Like the fluorescence detection technique itself, the chain of analysis of FD data has been refined over the years. While the programs used in this analysis are new, they are based conceptually on the analysis of the FADC fluorescence detector of the HiRes experiment. The programs that form the analysis chain are described in this chapter along with an explanation of the cuts applied to the data to prevent biasing from poorly-reconstructed events.

### 3.1. DST Files

Telescope Array is the largest cosmic ray observatory in the northern hemisphere with more than 120 members, many of whom are performing independent analyses on the same data. Therefore it is important to have a uniform storage system that allows individuals to access other members' data without spending a lot of time translating it into their own formats. The collaboration decided to use the DST format, used by the HiRes experiment.

A DST file contains a sequential list of *events*, each containing one or more elements called *banks*, stored in sequence within each event. Typically, a program that processes data in one DST file will write out a separate DST file where each event has all the banks from the original file plus additional banks which contain the results of the processing for that event. This inefficiency is the largest drawback to the DST system, because analysis programs that do not automatically apply event rejection will always generate output files that are larger than the input files. An example of the layout of a DST file is shown in Figure 3.1.

## DST File Format

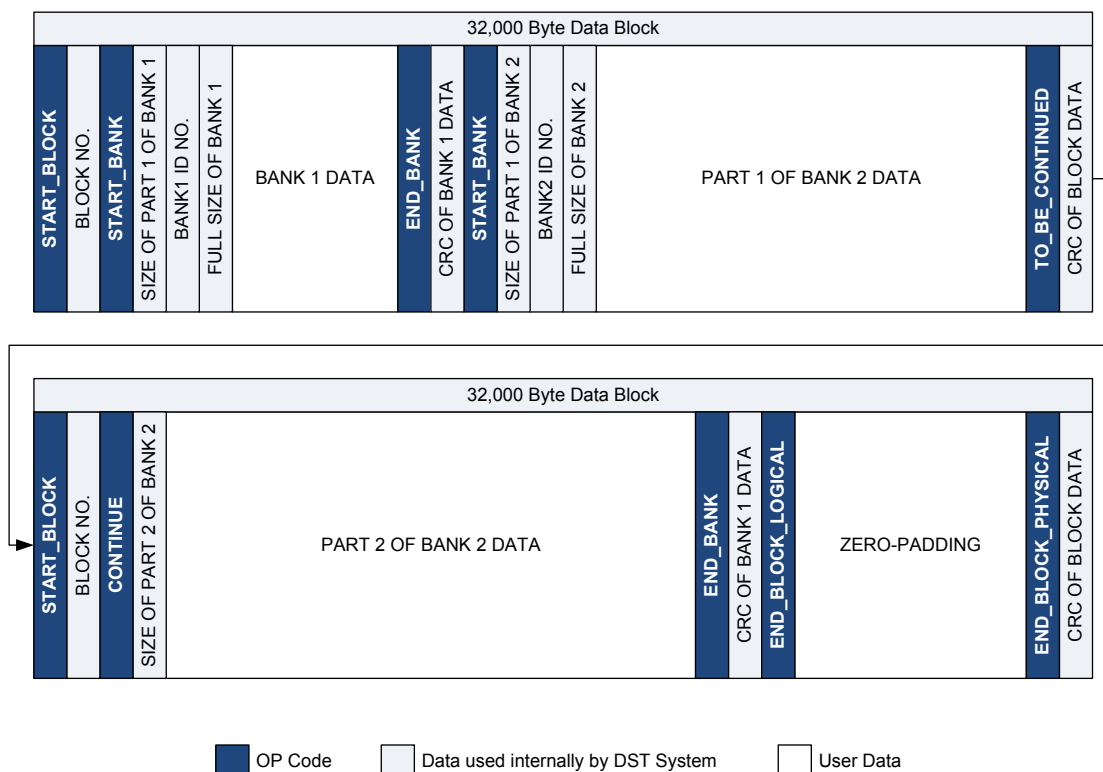


**Figure 3.1** Diagram of main components of a DST file. Files are stored in 32 kB blocks with CRC32 checksums. Banks may be split across two or more data blocks, each with a CRC checksum. “Events” are defined by sandwiching data blocks between special “Start” and “Stop” DST banks.

Dozens of DST banks have been defined at this point. Those relevant to this analysis are listed in Table 3.1, categorized by the banks found in analyzed data, those used by the TRUMP Monte Carlo simulation program and those used to store calibration data. To accommodate stereo analysis, some of the banks are designed to “extend” a template bank. For example, a user may want to combine plane-fitting data from both BRM and LR FD stations for a single event. The bank structures will have the same variable names, but the DST system requires them to be distinguishable. In these circumstances, by convention, the template bank will contain the letters ‘FD’ in its structure or class name, which is replaced by either ‘BR’ or ‘LR’ in the implemented bank’s name.

(a) Banks for processed data.		
Bank Name	Bank ID	Contents
FDRaw	12102/12201	Pre-processed raw waveform data and GPS timing.
FDPlane	12103/12203	Results of geometry fitting, NPE counts and time windows.
FDTubeProfile	12106/12206	Results of profile fitting, measured flux at FD and acceptance analyzed by tube.
TrumpMC	12803	Simulation data (e.g. shower parameters, light generated at shower and light flux at FD).
(b) Banks used by TRUMP Simulation		
Bank Name	Bank ID	Contents
FDPed	12416/12426	Background FADC mean and variance by channel in one-minute averages.
ShowLib	12811	Shower library entry with fit parameters to a single air shower event simulated by CORSIKA.
ShowScale	12812	Set of linear scaling parameters for an entire shower library.
(c) Banks for Detector Geometry and Calibration Data		
Bank Name	Bank ID	Contents
GeoFD	12101/12202	FD telescope critical dimensions, radii of curvature, focal length, etc.
FDMirrorRef	12400	Mirror reflectance in 10-day intervals, interpolated from semi-annual measurements.
FDBG3Trans	12401	BG3 filter transmittance interpolated in 1nm wavelength steps from 250-500nm.
FDParaglasTrans	12402	Paraglas transmittance interpolated in 1nm wavelength steps from 250-500nm.
FDPMTQECE	12403	Average PMT quantum efficiency and collection efficiency. CE is constant, QE is interpolated in 1nm steps.
FDPMTUniformity	12404	Average PMT uniformity, mapped with 1mm <sup>2</sup> resolution.
FDPMTGain	12405	Absolute PMT gain in FADC/337nm photon with one entry per 10-minute interval.
FDAtmParam	12409	Thermodynamic properties of the atmosphere ( $P$ , $T$ , $\rho$ ). Each entry covers a user-defined time period.
FDScat	12410	General aerosol scattering parameters (HAL, Scale Height). Each entry covers a user-defined time period.

**Table 3.1** DST banks used for this analysis.

### 3.2. Raw Data Storage

During observation runs, the FDs switch between data acquisition and calibration run modes, each assigned a unique ID number. This typically begins with two 1000-trigger “1-sigma” runs, named for the trigger threshold setting, to measure background levels from the electronics and night sky. The bay doors are closed during the first 1-sigma run and open for the second. This is followed by start-of-observation YAP and XF calibration runs with the SDF set to “6-sigma” mode. Normal data acquisition runs (DAQ) are often found in pairs, with one set of three or four thousand triggers immediately followed by a separate run for 6-12 thousand triggers, depending on the average trigger rate from the previous run. Another YAP and XF calibration pair follows and the cycle continues throughout the night. Observation ends with two more 1-sigma doors-open and doors-closed runs. Only regular data acquisition runs, i.e. 6-sigma ‘DAQ’ runs, were used directly for the analysis presented in this dissertation.

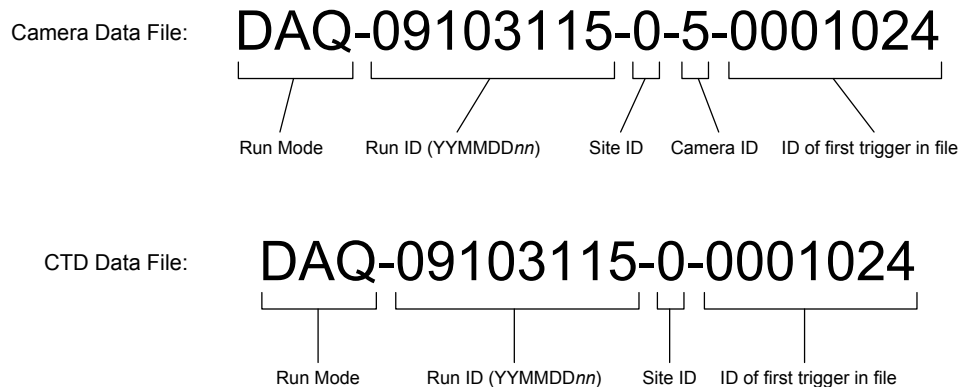


**Figure 3.2** File naming convention for raw FD data.

Event data is stored 256 triggers at a time using the file name convention shown in Figure 3.2. The FDs are synchronized, but each camera’s PC saves its waveform data independently. The camera data files begin with a 256 byte header containing some general diagnostic information specific to the PC which generated the file. This is followed by 256 camera event data blocks, consisting of a 128 byte event header and the FADC buffers from all 256 channels, shown

schematically in Figure 3.3. Waveform data is stored in arrays of 512 2-byte unsigned integers, but since the FADC count itself only requires 14 bits, the highest two are used to pack information about background levels, thresholds and PMT “hit” status (Figure 3.4). The file ends with a 64-byte footer block containing some basic diagnostic information. GPS timing and synchronization data are saved by the CTD computer. The layout of a CTD data file is similar to the camera data file, but requires substantially less hard disk space.

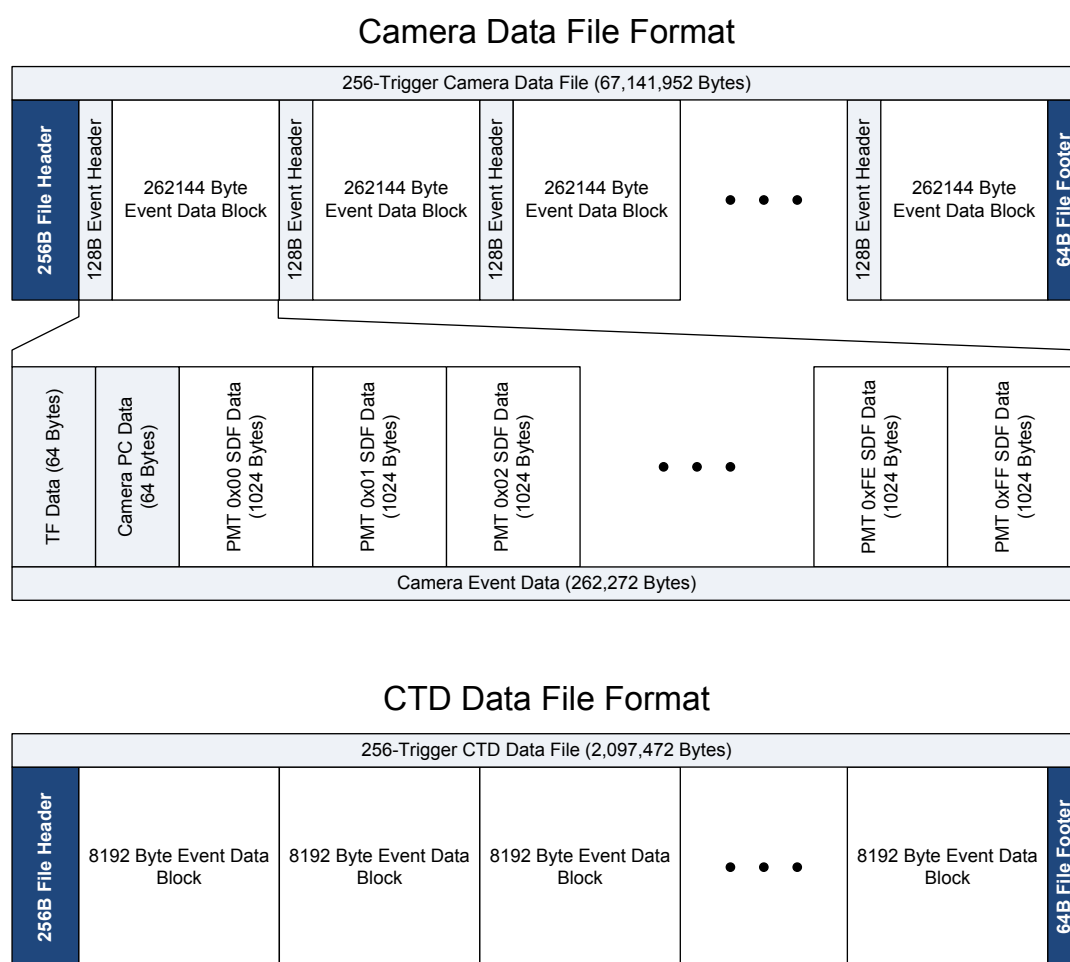


**Figure 3.3** Raw Data Format. FD Camera and CTD data files hold a maximum of 256 trigger events. File sizes are reduced an average of 65% with BZ2 file compression.

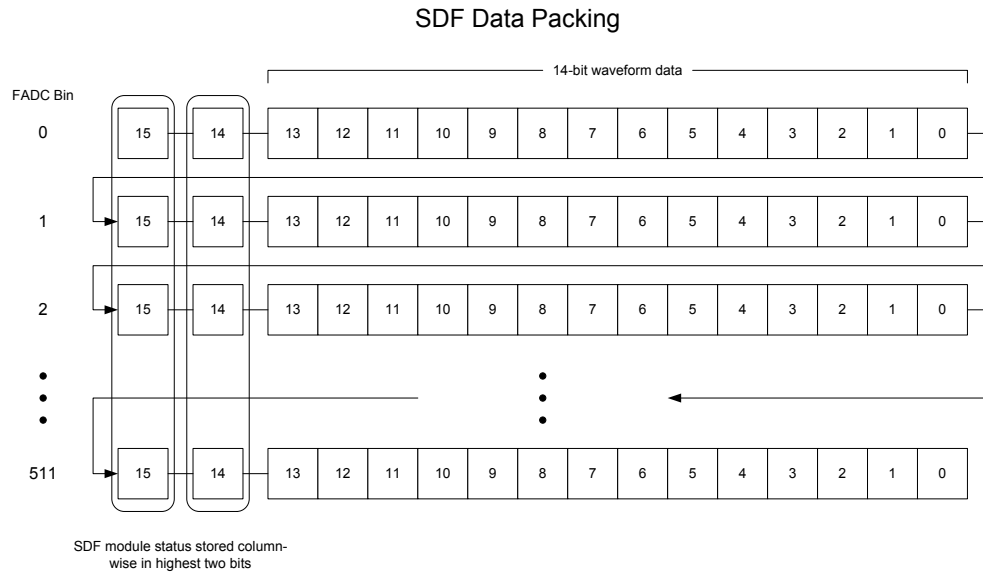


**Figure 3.4** Waveform data packing. Raw FADC data uses 14 bits. SDF module information is packed column-wise into the highest two bits.

### 3.3. Computing Resources

The Telescope Array Project involves members in the US, Japan, Korea, Russia and Brussels. The various institutions and funding agencies come with access to large-scale computing resources like the Center for High Performance Computing (CHPC) at the University of Utah and the TeraGrid Network. The systems utilized for this work are mapped out in Figure 3.5. Raw data is processed and analyzed on the Sith cluster because it is directly connected to the servers on which the raw data are stored. The Monte Carlo simulation and analysis of MC data was done on the super-clusters of CHPC, but significant development and debugging was performed on the Purdue Condor Pool, a member of the TeraGrid network. The earliest development and testing of the analysis programs was done on a small compute farm at Rutgers, but this constituted an insignificant time period so it is not represented in the figure.

Programs developed by members of Telescope Array are maintained on a Subversion software repository at the Institute for Cosmic Ray Research (ICRR) in Kashiwa, Japan. This provides a central source for collaboration members to view and run other members' programs

## Computing Resource Map

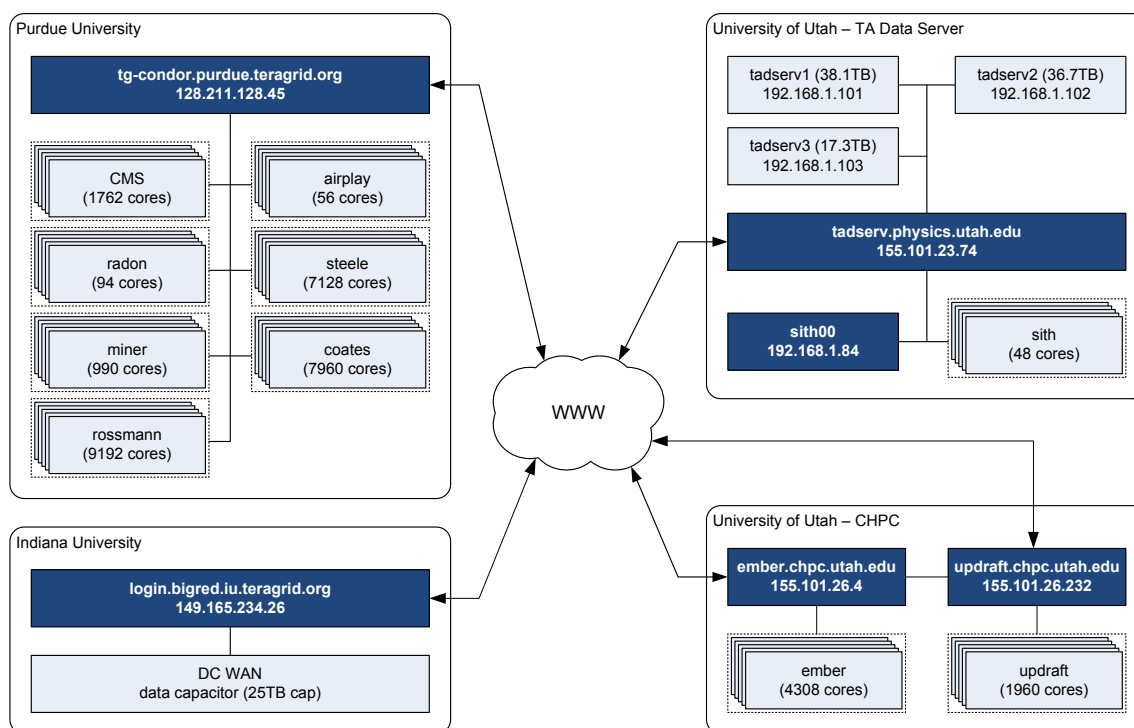


**Figure 3.5** Computing resource map. This figure only shows the resources used for this work.

and analyses and was the means of synchronizing programs across the different systems. This ensured that the programs used to analyze real data were identical to those used to process simulated data. Additionally, a MediaWiki server is installed on the head node of the TA data server at the University of Utah for collecting abstracts, presentation slides and publications. Members can also create and edit each other's Wiki articles which, in an experiment where individuals separated by large distances may need to collaborate closely on particular projects, make planning and reporting progress an easy process.

### 3.4. TAMA

The FADC fluorescence detectors generate a tremendous amount of raw data. An event triggers each FD station roughly twice a second. With each trigger, the FADC buffer from every channel of every camera in the station is saved, totaling 3 MB per trigger. After compression,

approximately 10 GB of data per hour of observation is collected. This work uses data collected over three years, corresponding to 25 TB of raw data, 99.9% of which doesn't make it to the final analysis. It is common, especially early in the experiment's lifetime while software is being developed, that code is changed or other corrections need to be made that require the analysis programs to be re-run from the beginning. A significant amount of time is saved when there is a special set of pre-processed data that is not sensitive to these changes.

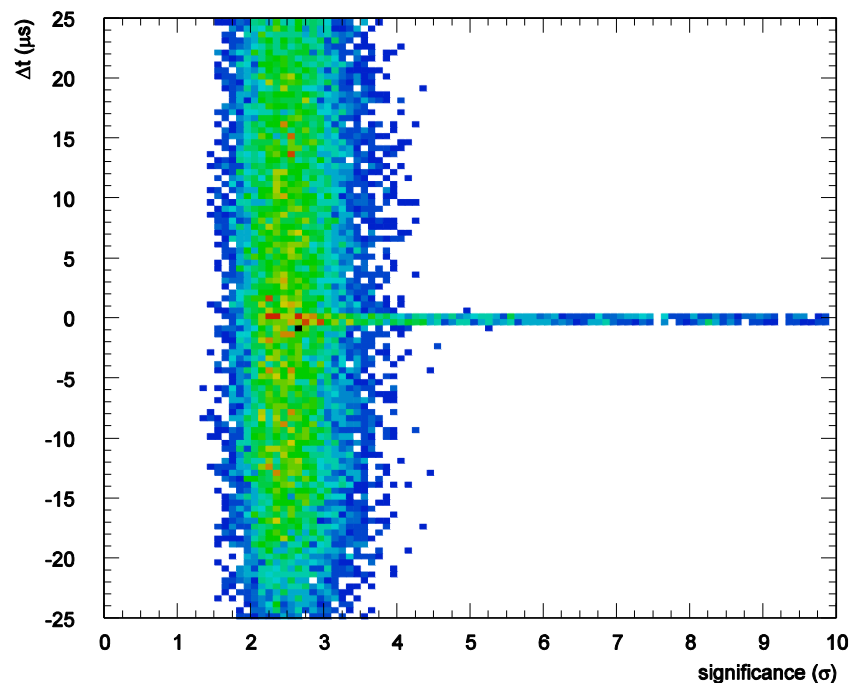


**Figure 3.6** 2D Histogram of the difference between measured signal time and the expected time for a single night's data, plotted against signal significance. Expected time is based on the tangent fit. The z axis is in arbitrary units.

TAMA (for TA MAtch) generates DST files from the raw data saved by the 12 cameras and CTD computer in each FD station. It applies a simple noise rejection algorithm which produces files  $1/10^{\text{th}}$  the size of the corresponding raw data. When the TF module signals the CTD of a track, the code number is stored as part of the raw data. TAMA only keeps data from cameras with non-zero TF code number or those adjacent to them, a requirement which by itself cuts

the data by more than half. Additionally, only tubes that register a signal more than  $3\sigma$  over background are kept, based on a 16 and 32-bin sample within the FADC buffer. That is,

$$\sigma = \max\left(\frac{S_i - wM}{\sqrt{wV}}\right), \quad S_i = \sum_{k=i}^{i+w} F_k \quad (3.1)$$

where  $M$  is the mean background FADC level,  $V$  is the variance of the background,  $F_k$  is the FADC count in time slice  $k$  and the sum is taken over sample size  $w$ . The index of  $S_i$  is incremented in steps of  $w/2$ . Note that this is not the same algorithm used by the SDF threshold generator for finding hit tubes. Figure 3.6 is a plot of the difference between measured signal time and the time it “should” have been received, based on the geometry fit, versus significance. The broad vertical band clearly comes from noise channels and the thin horizontal band is signal. There is some overlap, but this figure shows that  $3\sigma$  is a reasonable place to cut.

The 16 and 32-bin sample window sizes are selected because they are the characteristic transit times for the projection of real cosmic ray showers across a single tube’s field of view. For pure noise, there will be a tendency for the smaller sample window to produce the most significant signal to noise fraction, mainly because there are more opportunities (63 quasi-independent samples in a given waveform compared to 31 for the 32-bin samples). The expected number of samples with significance greater than  $\sigma_{\min}$  can be found by multiplying the number of opportunities by the complementary error function,

$$n(\sigma > \sigma_{\min}) = 63 \operatorname{erfc}\left(\frac{\sigma_{\min}}{\sqrt{2}}\right). \quad (3.2)$$

This evaluates to 1 for  $\sigma_{\min} \approx 2.45$ , corresponding to the peak of the vertical band in Figure 3.6.

### 3.5. Fitting the Shower Geometry

The extensive air shower propagates in a nearly straight line through the atmosphere from the primary interaction point in the trajectory of the primary particle’s momentum. Air showers

typically extend several kilometers and have a lateral extent on the order of tens of meters. Therefore, air showers are well described as a point source of light traveling along a line at the speed of light.

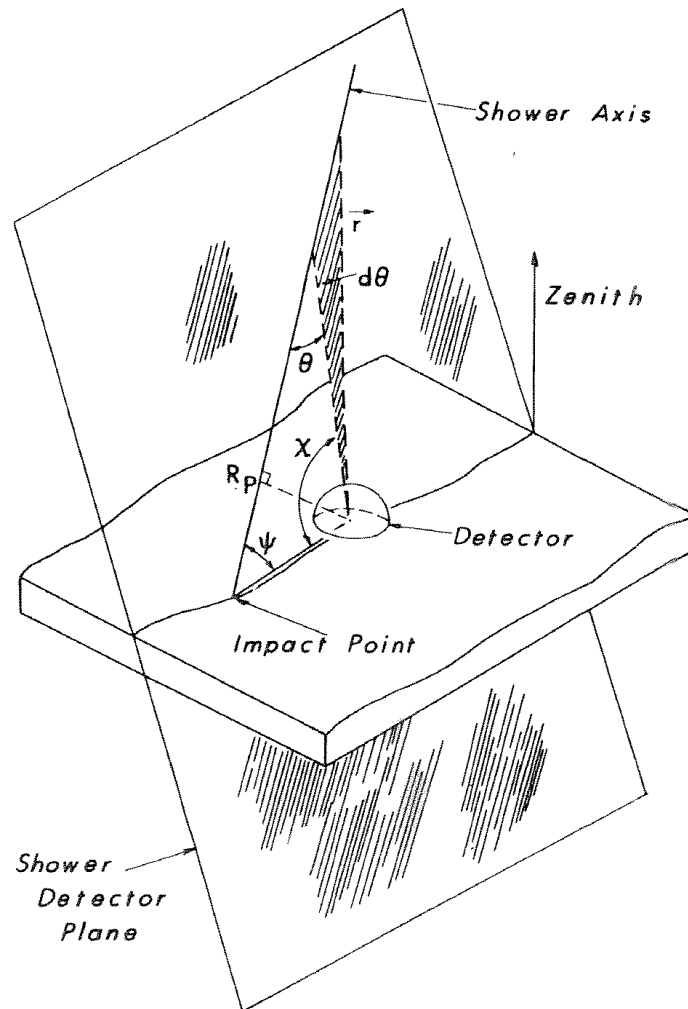


**Figure 3.7** Shower geometry parameters in monocular reconstruction [28].

The determination of air shower geometry using information from only one FD station is called monocular geometry reconstruction. In monocular analysis, the physical location and orientation of the shower axis is described by the unit vector normal to the plane it forms with the detector ( $\hat{n}$ ), the angle it forms with the ground in that plane ( $\psi$ ) and the impact parameter of the primary cosmic ray particle with the detector ( $R_p$ ). These parameters are shown schematically in

Figure 3.7. The shower-detector plane (SDP) is found first, which defines  $\hat{n}$ , then  $R_p$  and  $\psi$  are found in the tangent fit phase, where relative signal timing and PMT viewing directions are used to determine the orientation and position of the shower axis.

The SDP fit is an iterative process which minimizes the  $\chi^2$ ,

$$\chi^2 = \sum_{i=1}^{N_{\text{gt}}} (\hat{n} \cdot \hat{v}_i)^2 (N_{\text{pe}})_i \quad (3.3)$$

where  $\hat{v}_i$  is tube  $i$ 's viewing direction relative to the FD station and the summation is taken over “good” tubes,  $N_{\text{gt}}$  (i.e. tubes with a proven signal). The residual is weighted by the estimated number of photo-electrons,  $N_{\text{pe}}$ , observed by channel  $i$ , found by scanning the waveform and isolating the signal from the background. Given a specific selection of tubes, the minimization can be done analytically by finding the smallest eigenvector of the matrix,

$$M_{jk} = \nabla^2 \chi^2 = 2 \sum_{i=1}^{N_{\text{gt}}} v_{ij} v_{ik} (N_{\text{pe}})_i. \quad (3.4)$$

But, since tube selection depends on the best-fit SDP, the chi-square must be recalculated each time tubes are added or removed from the good tube list.

Once the SDP is established, the orientation of the shower axis in that plane is found by performing a chi square minimization of relative PMT signal timing as a function of viewing angle in that plane. To do this, one must compute a mean signal time from the waveform data from each good tube. Since each waveform will contain signal and noise data, a DSP filter must be used and the signal bracketed, or else the fits will be biased and the subsequent analysis will be corrupted. In this case, the first step is to subtract the average background, using the measurements stored in the raw data. Then the filter is applied and the signal is bracketed by scanning away from the peak of the filtered waveform until the level falls below zero. The average signal

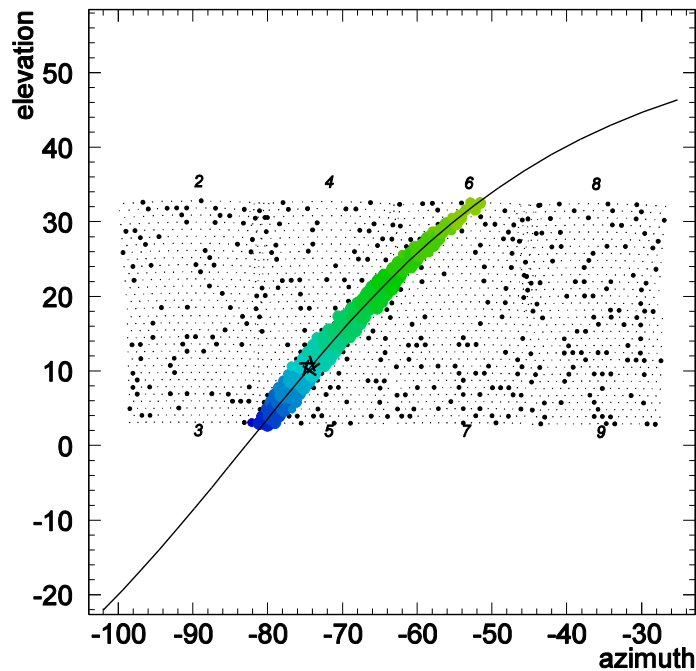


**Figure 3.8** Example of a shower-detector plane fit.

time is then found by taking the average time-bin index weighted by the background-subtracted FADC count.

The performance of the DSP will depend on the type of filter applied. The signal-to-noise ratio is maximized by selecting a filter which most closely matches the shape of the underlying signal. From the perspective of the FDs, air showers appear approximately as point sources moving through space at the speed of light. As I mentioned in Chapter 2, the design parameters of the FDs were optimized so the spot size is roughly the same no matter where the projection lies on the camera. The projection of a point source onto the camera has a diameter of approximately 40 mm, while the active area of each PMT is nearly 60 mm. So, as the shower propagates and its projection on the camera crosses the PMTs, a roughly trapezoidal light profile will be produced in each one. The shape of the trapezoid is slightly distorted due to autocorrelation in the time bins (a result of the Butterworth filter) and noise, and its width will depend on the distance to the shower (more distant showers will produce slower-moving projections on the focal plane). A

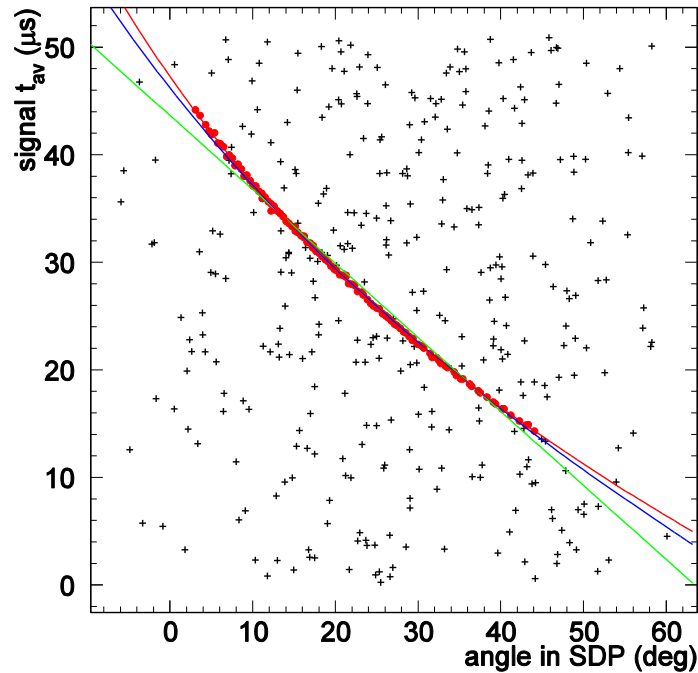


**Figure 3.9** Example of a time versus angle fit. Each point represents one tube. The red circles are points actually used for the fit and the black crosses are noise. The green, blue and red curves are the linear, pseudo-tangent and full tangent fits, respectively.

triangular filter is used here because we found that it was the most effective at separating signal from noise, even in low-signal channels.

The parameters  $R_p$  and  $\psi$  are found by fitting PMT signal time to the tangent function,

$$t = t_0 + \frac{R_p}{c} \tan \left[ \frac{1}{2} (\pi - \psi - \chi) \right]. \quad (3.5)$$

Here,  $\chi$  is the viewing angle in the SDP and  $t_0$  is an arbitrary constant (its physical meaning is the arrival time of light produced at the shower axis at  $\chi = 0$ , but this is often not seen).

Frequently, when trying to minimize  $\chi^2$  sums using functions like Equation (3.5), nonsense values come out of the fit unless reasonable starting estimates are used. To avoid this problem, two other fits are performed before attempting the tangent fit. First, a linear fit is done to establish if the PMTs triggered in generally downward-going order. This is typically unnecessary for the later stages of the time fit, but useful for eliminating “upward” events and showers that

move so quickly across the camera that a proper time fit is not possible. Then, a pseudo-tangent fit is done which presumes the shower is perpendicular to the ground in the SDP, i.e.  $\psi = \pi/2$ . Figure 3.9 shows an example time versus angle fit. The red circles represent tubes with proven signal (aka *good* tubes) and the black crosses represent noise tubes.

### 3.6. Fitting the Shower Profile

The large number of systematic issues involved in the connection between numbers of charged particles and ADC counts make the Inverse Monte Carlo (IMC) method an ideal choice for shower profile estimation. The shower profile is described by a form of the Gaisser-Hillas function with four parameters (Equation (1.14)). In the Inverse Monte Carlo method, air showers are simulated (using the best-fit geometry) and the GH parameters are varied until the best agreement between real and simulated signal is found, minimizing the  $\chi^2$ ,

$$\chi^2 = \sum_{i=1}^{N_{\text{gt}}} \frac{(S_i - \tilde{S}_i)^2}{\delta S_i^2} \quad (3.6)$$

where  $S_i$  is the number of signal PE received by channel  $i$ . The tilde on the  $\tilde{S}_i$  in Equation (3.6) indicates simulated signal using the same integration window determined for that tube during the geometry fit. For each channel, the number of signal PE are determined by integrating the FADC over the time window determined during the geometry fit,

$$S_i = \sum_{j=t_{1i}}^{t_{2i}} \frac{F_{ij} - M_i}{g_i} \quad (3.7)$$

where  $F_{ij}$  is the value of the raw digital readout in time index  $j$  of PMT channel  $i$ ,  $M_i$  is the average background level computed by the SDF and  $g_i$  is that channel's gain in ADC counts per photo-electron. The uncertainty in  $S_i$  comes from the statistical error in the number itself, night-sky background fluctuations and the binomial error in the tube's *acceptance*. The total uncertainty is given by,

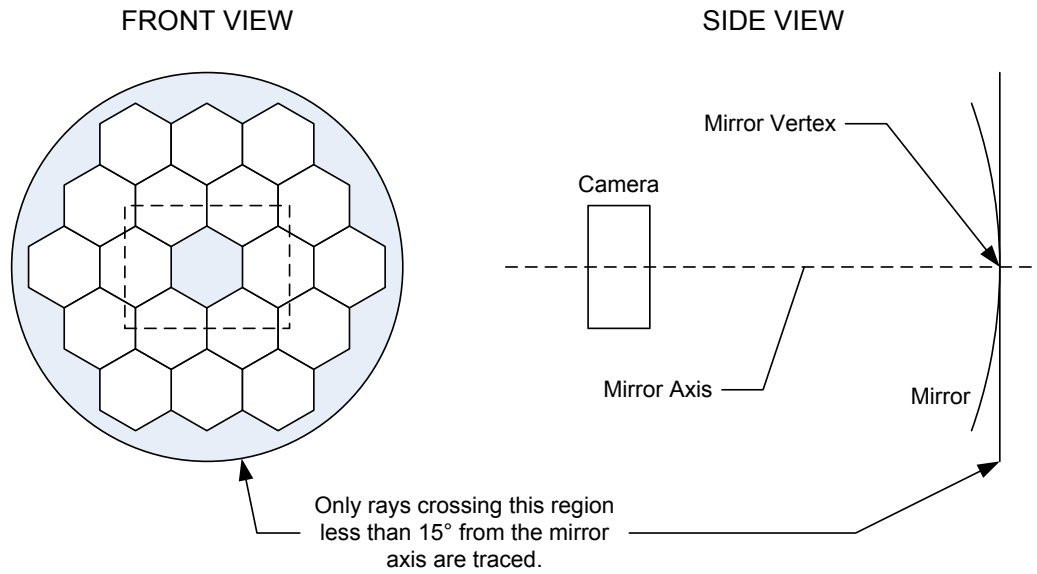


**Figure 3.10** Region of FD considered when calculating acceptance. Only the mirror segments and camera are shown (not to scale) for the purpose of the diagram. Ray tracing also considers the camera support structure, the hand rail in front of the ring 1 mirrors (physically placed above the ring 2 mirrors) and the wind baffle placed at the center of each bay door opening.

$$\delta S_i^2 = S_i + N_{\text{sky}} + \sum_{j=t_{1i}}^{t_{2i}} \left[ \frac{(F_{ij} - M_i)^2}{g_i^2} \left( \frac{1}{v_{ij}} - \frac{1}{n_j} \right) \right]. \quad (3.8)$$

Acceptance is the ratio of accepted rays ( $v_{ij}$ ) traced from a simulated air shower to the number thrown ( $n_j$ ). There are many ways a ray can fail to be collected by a PMT. For example, the ray may be blocked by the camera box or support structure, it may fall on the space between tubes, it may miss the camera from spherical aberration, or the light may miss the mirror altogether. For a ray to be counted as thrown, it must cross a circular region centered at the mirror vertex at an angle less than  $15^\circ$  from the mirror axis (Figure 3.10).

Each thrown PE is passed through the ray tracing code of the FD simulator, which is detailed in the next chapter. It is computationally intensive and has inherent randomness, which enters in three places; (1) when determining where the ray strikes the mirror, (2) where the reflected ray actually strikes the cluster if it's not shadowed by the camera or support structure, and (3) when deciding if the ray will actually result in a PE being produced. Furthermore, the wave-

form is simulated including Poisson-distributed night-sky background. If ray tracing was performed during minimization, the  $\chi^2$  sum will itself be random and the minimizing would fail to converge. It is therefore important to build a table for each event which stores each PMT's acceptance for light produced from a given location and time.

Accepted PE are found by taking the simulated waveform data, applying the PMT and time bin selection determined in the geometry fit, then subtracting the background and dividing by gain. The same shower is simulated multiple times using the same geometry and GH parameters to reduce the uncertainty from the acceptance calculation. The acceptance is then used to compute the numbers of photo-electrons incident on each tube. Since shower energy is weakly dependent on  $X_0$  and  $\lambda$ , they are set to  $-100$  and  $60 \text{ g/cm}^2$ , respectively, and only  $N_{\text{max}}$  and  $X_{\text{max}}$  are varied for the fit. Because shower width is a function of  $X_{\text{max}}$ , a new acceptance table is generated if the fitter changes its value by more than  $50 \text{ g/cm}^2$ . For each new acceptance calculation, the shower is simulated 10 times over. When the fit is near convergence, the acceptance is computed by simulating the shower 20 times to further reduce statistical error.

There is a subtle issue that enters in when considering the time index  $j$  of thrown and accepted PE. For thrown PE, the time index comes from the total transit time from the shower to the FD plus ten nanoseconds to account for the mirror-camera separation. In the case of accepted PE, a light ray is traced from the shower through the detector and the electronics response is simulated. The transfer function from the pre-amp and shaper circuit spreads the signal out an average of 80 ns after the PE arrival times. An adjustment is made to account for the delay between the true PE arrival time and the time the resulting signal reaches its maximum at the FADC chip. This improves the agreement between the time indices of thrown and accepted PE.

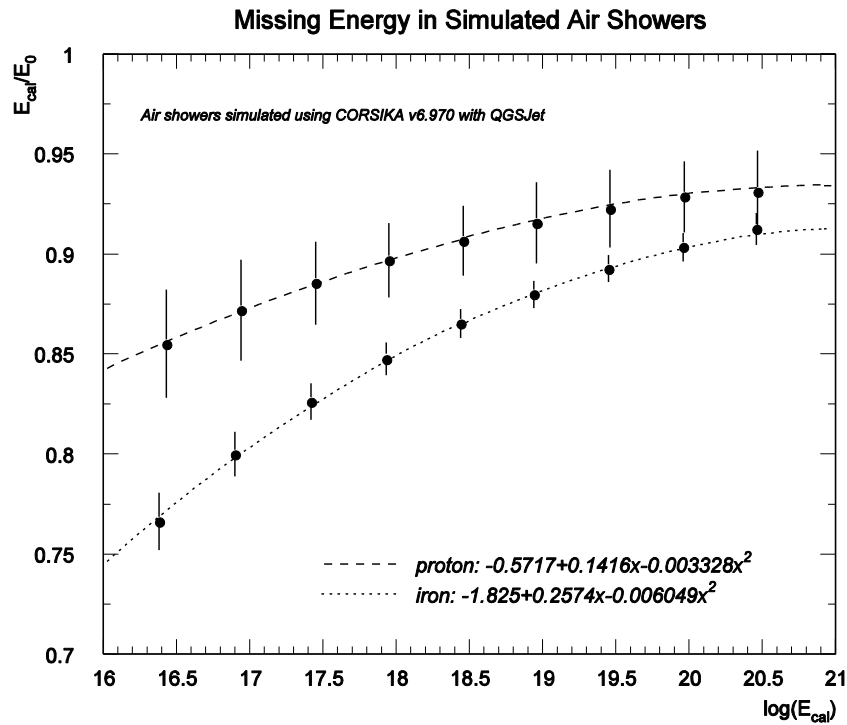


**Figure 3.11** Missing energy correction derived from CORSIKA showers. Showers with only proton or Iron primaries were simulated, each fit to their own quadratic function in  $\log E_{\text{cal}}$ , the results of which are shown in the figure.

### 3.7. Primary Energy Estimation

The result of the profile fit provides a set of parameters for the Gaisser-Hillas function which describes the number of charged particles present in an extensive air shower after it has propagated to a depth  $X$  through the atmosphere. The GH function is related to the local energy deposit through the mean ionization loss  $\alpha$  by,

$$\frac{dE_{\text{dep}}}{dX}(X) = \alpha(X) N_{\text{ch}}(X) \quad (3.9)$$

The energy deposited into the atmosphere by the air shower, also called the *calorimetric* energy, is found by integrating the local energy deposit as a function of  $X$ ,

$$E_{\text{cal}} = \int_{\tilde{X}_0}^{\infty} \frac{dE_{\text{dep}}}{dX}(X) dX. \quad (3.10)$$

To find the energy of the primary cosmic ray particle, the energy lost to neutrino production and nuclear excitation, collectively referred to as missing energy must also be accounted for. Missing energy is a real phenomenon, so it is inconsistent for various experiments to use different formulas to correct for it. But while some have been proposed based on simulations and extrapolation of particle accelerator data, no universally accepted formula exists. In this work, the correction for missing energy is derived from air showers simulated with CORSIKA. The simulated shower profiles are fit to the Gaisser-Hillas function and integrated with an expression for mean ionization provided by Nerling et al., the details of which are provided in the next chapter. Analysis of the simulation results revealed little dependence on shower geometry, but a strong dependence on composition. Only proton and iron-induced showers were simulated and each set fit to a quadratic function in  $\log E_{\text{cal}}$  (Figure 3.11).

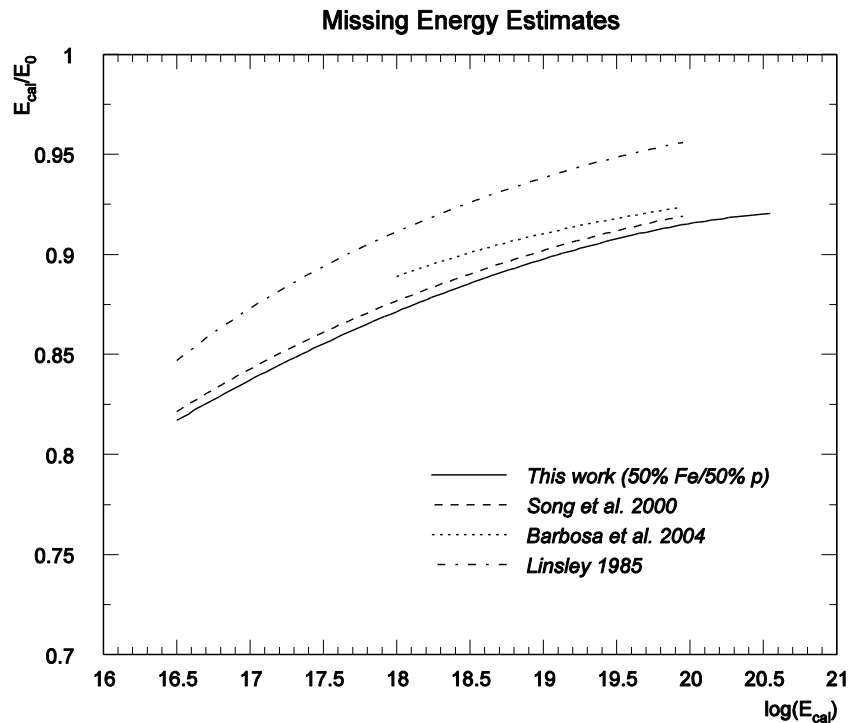


**Figure 3.12** Missing energy correction compared to other estimates. The curves shown represent an equal mixture of Iron and proton primaries except for Linsley, whose result is derived from experimental data [29][30][31].

Figure 3.12 shows how the results from this independent analysis of CORSIKA showers compare to other published expressions for missing energy. For consistency, an equal composition of protons and iron is shown. However, experimental results so far have suggested UHECR to be mostly light nuclei [32], so the missing energy correction used for this dissertation is derived from only proton-induced showers, yielding the formula,

$$\frac{E_{\text{cal}}}{E_0} = -0.5717 + 0.1416 \log E_{\text{cal}} - 0.003328(\log E_{\text{cal}})^2. \quad (3.11)$$

### 3.8. Data Selection and Quality Cuts

It goes without saying that the reliability of an experimental result is a function of the quality of the data from which it was derived. During a typical observation night, a fluorescence detector station will trigger  $\sim 100,000$  times, yielding  $\sim 10$  good events. Events must be rejected along the analysis chain if they are clearly not cosmic ray events or, if they are real showers, their geometry or profile fits are so poor that the estimates of the parameters that define them are unreliable. Unfortunately there is no “golden cut” which sweeps away all of the bad events at once. In fact, for every observable parameter, the distributions of good and bad events will have overlapping distributions. Therefore it is inevitable that some fraction of good events will be rejected by a given cut. The object is to find the proper balance between rejection of good events and acceptance of bad ones.

Some of the more frequent sources of noise triggers are distant airplanes and muons physically passing through the photomultipliers. Typically, the flashers used on aircraft are very bright and take a long time to reach a maximum intensity, relative to a  $50 \mu\text{s}$  time scale. There is a hardware-level airplane veto system which monitors their characteristic waveform signature. If the aircraft is far enough away, however, the signal may be strong enough to trigger the detector without triggering the veto mechanism. Muon triggers are easy to handle because they produce very sharp spikes in the tubes they cross. If one happens to pass through the camera in such a

(a) Geometry Cuts	
Tangent Fit Convergence	the fit does not converge
Good Tube Fraction	$N_{gt}/N_T < 3.5\%$
NPE per Degree	$N_{pe}/\Delta\chi < 25 \text{ deg}^{-1}$
Pseudo-distance	$r_p < 1.5 \text{ km}$
SDP Angle	$\cos^{-1} n_z > 80^\circ$
$R_p$ Cut	$R_p < 500 \text{ m}$
Psi Cut	$\psi > 130^\circ$
Time Extent	$\Delta t < 6.5 \mu\text{s}$
Psi Error	$\delta\psi > 36^\circ$
Tangent Fit Chi Square	$\chi^2/\text{DOF} > 10$
Track Length	$\Delta\chi < 7^\circ(10^\circ)$ in ring 1(2)
Zenith Angle	$\theta > 70^\circ$
$R_p$ Crossing Time	$t_0 > 25.6 \mu\text{s}$
Compound $R_p - \Delta t$	$R_p < 5\text{km}$ and $\Delta t < 6\mu\text{s}$
(b) Profile Fit Cuts	
Profile Fit Convergence	the fit does not converge
First Depth	$X_1 < 150 \text{ g/cm}^2$ or $X_1 > 1200 \text{ g/cm}^2$
Depth Extent	$\Delta X < 150 \text{ g/cm}^2$
Bracketing	$X_{\text{max}}$ not in detector field of view

**Table 3.2** Data Quality Cuts.

way that it triggers several tubes, the signals will appear to occur simultaneously. An event like this will be labeled “in-time” and be excluded from further analysis.

Table 3.2 describes the quality cuts used in this analysis. The analysis cannot continue if the geometry fit failed to converge, so this is the first test for event rejection. It should also be noted that a particular cut may not be designed to reject events which are necessarily difficult to reconstruct, but to eliminate a region that is difficult to simulate. The compound  $R_p - \Delta t$  is an example of this. Events in this range are sensitive to the relative pointing directions of the cameras. When analyzing simulation data, one can be sure that the detector geometry used in reconstruction is exactly the same as that used in the simulation. In fact, detector geometry is not exactly known and there will be a slight discrepancy between the geometry used for reconstruction of real data and that which exists in reality.

## Chapter 4. Detector Simulation and Monte Carlo

A full detector simulation plays an integral role in the analysis of fluorescence detector data. Detector sensitivity depends on air shower brightness and geometry, so it is best computed by Monte Carlo simulation of air shower events using the same distribution of geometry and energy observed in real data. Components of the simulation program are also used for estimating the charged particle profiles of real data events. Two simulation programs are described in this chapter, namely CORSIKA and TRUMP. CORSIKA is an air shower simulation program which is widely accepted among members of the cosmic ray research community. The longitudinal charged particle and energy deposit profiles that it produces are used by TRUMP, a fluorescence detector simulation program developed at Rutgers specifically for simulating the fluorescence detectors of Telescope Array. This chapter begins with descriptions of CORSIKA and TRUMP, and is followed by more detailed descriptions of the models used for fluorescence yield and propagation through the atmosphere. Finally, comparisons of critical parameter distributions from data and Monte Carlo will be shown to demonstrate that the simulation program provides an accurate representation of reality.

### 4.1. CORSIKA Shower Library

CORSIKA stands for COsmic Ray SIMulations for Kascade, a cosmic ray experiment in Karlsruhe, Germany. Developed by Dieter Heck and Tanguy Pierog of the Institut für Kernphysik, it is freely available to anyone who requests it [33]. When installing, the user may choose from different interaction models and other features. Since TRUMP uses Čerenkov and electron energy distribution models described in Nerling et al. [34], who also used CORSIKA for their work, it makes sense to use a configuration that most closely matches theirs. Table 4.1 lists the configurations used in each case.

	TRUMP Shower Library	Nerling et al.
CORSIKA version	6.617	6.137
High- $E$ interaction model	QGSJet01c	QGSJet01
Low- $E$ interaction model	GEISHA 2002	GEISHA 2002
Thinning	$10^{-5}$	$10^{-6}$
UPWARD option	Enabled	Enabled
$E_{\text{cut}}$ for hadrons & muons	100 MeV	100 MeV
$E_{\text{cut}}$ for $e^+$ , $e^-$ and $\gamma$ 's	1 MeV	1 MeV
ČERENKOV, LONG and SLANT options	Enabled	

**Table 4.1** CORSIKA configurations used in TRUMP and Nerling [34].

As shown in the table, the configurations used by Nerling and for the TRUMP shower library are identical with the exception of the choice of *thinning* level. Thinning is a computation-saving feature where secondary cosmic rays carrying energies below some fraction of the primary energy are bunched together into a single representative particle, which is given a weight according to the number of particles it represents. Larger values of thinning increase the fluctuations in the numbers of charged particles listed in the longitudinal development tables, but reduce computation time significantly. Since fits to the shower profiles are used instead of the actual table data, use of the same level of thinning is unnecessary.

Each CORSIKA run produces a number of output files, depending on the options used when compiling. In this case, the SLANT and LONG options were used so that the longitudinal profiles of the showers were saved as a function of *slant depth*, the amount of atmospheric matter traversed by the shower. With these options activated, CORSIKA produces a text file containing two tables for each simulated air shower; one to express the numbers of electrons, muons, photons, hadrons and neutrinos, and the other for local energy deposit by those particles.

TRUMP is designed to simulate a detector's response to an extensive air shower but not the shower development itself. A library of shower profile parameters derived from CORSIKA simulations is used instead, where each shower is fit to the Gaisser-Hillas (GH) function (c.f. Equation (1.14)). Recall from Chapter 1 that the GH formula is a function of four parameters: the number of charged particles present when the shower reaches its maximum intensity,  $N_{\text{max}}$ , the

depth in the atmosphere where the maximum occurs,  $X_{\max}$ , the effective depth of first interaction,  $X_0$ , (which may take negative values, and often does) and the shower width parameter,  $\Lambda$ , which is related to the characteristic charged particle interaction length. CORSIKA performs its own fit to every simulated shower, but it uses a width parameter which is quadratic in  $X$ . Instead of using CORSIKA's fit, CERN's MINUIT package was used to perform a least-square minimization of the charged particle profile using the common form for the  $\chi^2$  sum,

$$\chi^2 = \sum_i \frac{(y_i - N(x_i))^2}{\delta y_i^2}. \quad (4.1)$$

Here,  $y_i$  is the sum of the charged particles in the table row corresponding to slant depth  $x_i$  and  $N(x_i)$  is the GH formula. The use of thinning causes fluctuations in the number of particles represented, which must be accounted for in the uncertainty. After some trial and error, weights of  $\delta y_i^2 = y_i \cdot \max(y_i) \cdot 10^{-4}$  were found to produce mean  $\chi^2$ s per degree of freedom near unity. The complete shower library consists of 45,000 simulated showers divided into 90 “drawers”, each corresponding to a specific energy and zenith angle. The energy levels go from 16 to 20 in half-decades in  $\log E/\text{eV}$  and from 1 to 2 in steps of 0.25 in  $\sec \theta$ , with one library for proton showers and one for iron.

After generating random shower energy and geometry, TRUMP finds the drawer in the shower library with the nearest energy and zenith angle. One set of shower parameters is selected at random from the 500 entries in the drawer. All of the Gaisser-Hillas parameters have some dependence on energy which are modeled well by a linear function in  $\log E$ . To account for this, the average  $\log N_{\max}$ ,  $X_{\max}$ ,  $X_0$  and  $\Lambda$  are plotted against  $\log E$  and fit to a line. The scale factors are saved with the shower library and are used by TRUMP when interpolating between energy levels. The result is a set of Gaisser-Hillas parameters for an air shower, scaled according to a random energy and zenith angle. Scale factors for the zenith angle dependencies are saved as well, though none of the parameters have a significant dependence on it. Figure 4.1 shows how

the Gaisser-Hillas parameters depend on energy ( $y$ -axis in  $\log E$ , labeled 16-20) and zenith angle ( $x$ -axis in  $\sec \theta$ , labeled 1-2). The units of the  $z$ -axes for the  $X_{\max}$ ,  $X_0$  and  $\Lambda$  plots are all in  $\text{g}/\text{cm}^2$ . The plots show that  $X_0$  and  $\Lambda$  do not have simple linear dependence on  $\log E$  and  $\sec \theta$ , but the overall shape of the Gaisser-Hillas function is weakly dependent on these parameters.

There is a subtlety which must be addressed when incorporating the shower library data into TRUMP. The particle number tables produced by CORSIKA only account for particles above a user-defined minimum energy. This is a feature which is independent of the thinning option mentioned earlier. During the simulation, when a particle is found to have energy below this threshold, tracking of that particle ends and its total energy added to the local energy deposit according to special rules, depending on its type. In this manner, the energy deposit tables account for below-threshold particles, but the particle number tables do not. One could make the argument that fluorescence yield is proportional to energy deposit and that the energy deposit profile of an air shower has the shape of a Gaisser-Hillas formula. But the formula was derived from EM cascade theory and it is meant to represent the number of charged particles present in an air shower. Therefore we maintain that, while the charged particle profile expressed in the CORSIKA output files is smaller than that which would exist in reality, given the same conditions, it is more appropriately expressed by the GH formula than the energy deposit profile would be. As is shown by Equation 15 from [34], these quantities are simply related through the mean ionization loss rate per particle, so either representation is acceptable.

## 4.2. TRUMP

TRUMP is an acronym for Telescope Array Reversible and Updateable Monte Carlo program. It is “reversible” because the same function libraries used for shower simulation can be used for inverse Monte Carlo. Its object-oriented design makes it “updateable” in that large portions of code may be easily updated or replaced.

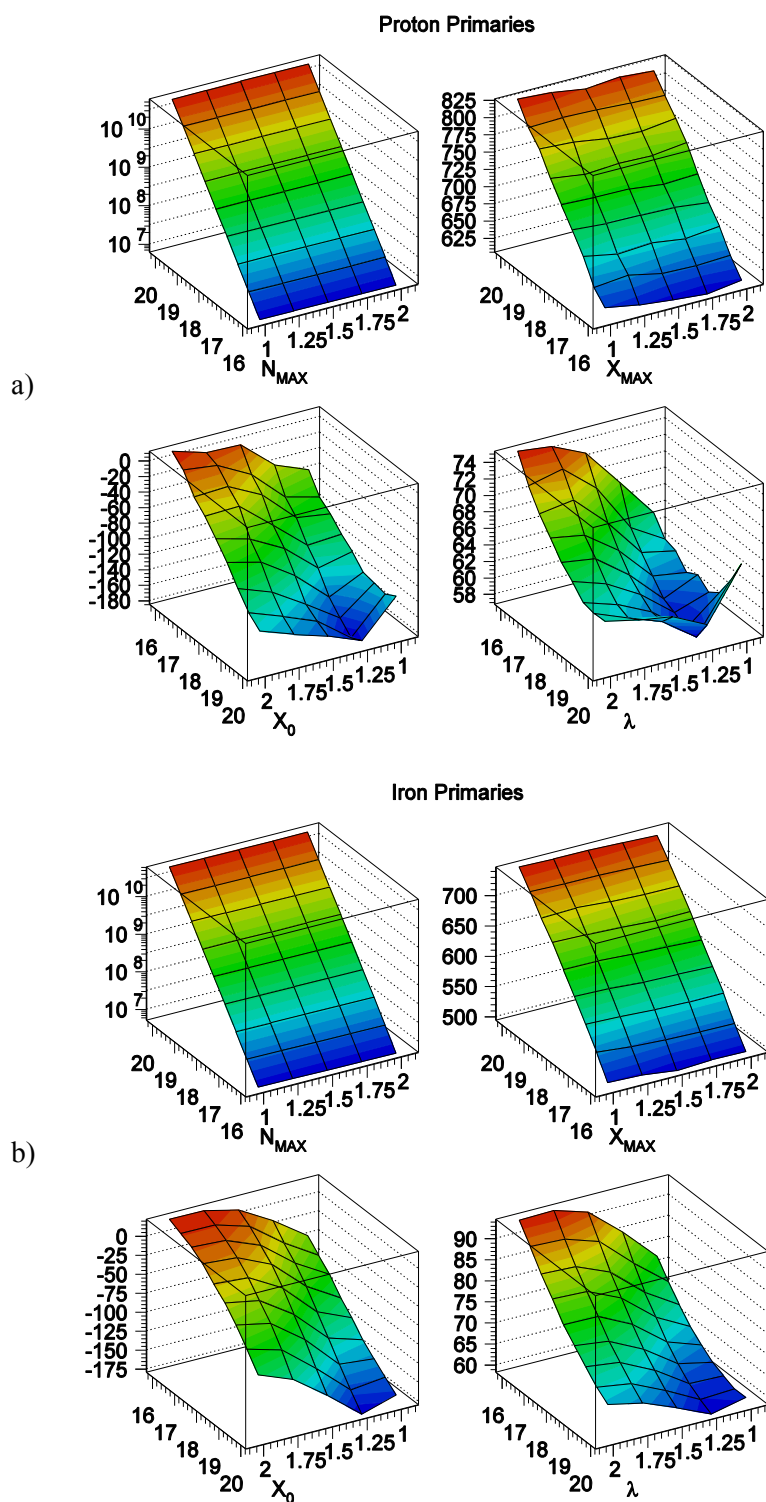


**Figure 4.1** Gaisser-Hillas parameter dependence on  $E$  and  $\theta$ . Figures (a) and (b) correspond to proton and Iron primaries, respectively.  $x$ -axes are  $\sec \theta$  (labeled 1-2),  $y$ -axes are  $\log E$  (labeled 16-20) and  $z$ -axes for  $X_{\max}$ ,  $X_0$  and  $\lambda$  are in  $\text{g}/\text{cm}^2$ .

FILE	[%s]	Output file name
PARENT	[%s]	Parent directory of output file
STARTID	[%d]	ID number of first successful triggering event
NTRIALS	[%d]	Number of trigger attempts before quitting
NEVENTS	[%d]	Number of successful triggers before quitting
SEED	[%d]	Random number seed
ORIGIN	[%f %f %f]	Global origin latitude, longitude and altitude (deg,deg,m)
EVENTLIST	[%s]	Path to list of user-defined events
ONTIME	[%s]	Path to FDPed file for on-times by part number
DTIME	[%f]	Average $dt$ for consecutive events (seconds)
SPECIES	[%d]	Particle species ID using CORSIKA convention
SHOWLIB	[%s]	Path to shower library file
ATMOSDB	[%s]	Path to atmospheric parameter database file
SCATTE	[%s]	Path to molecular scattering parameter database file
ENERGY	[%f %f]	Primary particle energy bounds (low, high in log(eV))
NBREAK	[%d]	Number of break points in power law spectrum
EBREAK	[%f ... %f]	Break point energies for power law spectrum (log(eV))
ESLOPE	[%f ... %f]	Power law slopes between break points
CLFENERGY	[%f]	CLF energy in mJ
RP	[%f %f]	Bounds for shower impact parameter (low, high in km)
PHI	[%f %f]	Bounds of azimuthal direction of shower development (low, high in deg)
THETA	[%f %f]	Bounds of shower zenith angle (low, high in deg)
LAT	[%f]	Core location limit in angular distance from CLF (deg)
SITEID	[%d]	Site ID (0=BRM, 1=LR, 2=MD)
GEOFILE	[%s]	Path to FD geometry file
MIRREF	[%s]	Path to mirror reflectivity DST file
PARAGLAS	[%s]	Path to Paraglas transmission DST file
BG3	[%s]	Path to BG3 transmission DST file
PMTQE	[%s]	Path to PMT QECE DST file
PMTGAIN	[%s]	Path to PMT gain DST file
PMTUNIF	[%s]	Path to PMT uniformity map DST file
PMTCAL	[%s]	Path to pedestals DST file.
PSI	[%f %f]	Bounds of shower angle in SDP (low, high in deg)
PHIIMP	[%f %f]	Bounds of azimuthal direction to core (low, high in deg)
SKYBG	[%f]	Default night sky background level (# per 100ns)

**Table 4.2** List of configuration parameters recognized by TRUMP. First column is the parameter name, followed by the argument format (%s=string, %d=integer, %f=float) and a brief description.

TRUMP consists of five modules: AirShower, Control, FADCTel, RayTrace and Toolbox. The Control and Toolbox libraries handle run time behavior and contain custom mathematics routines. The AirShower package contains the functions for air shower simulation and atmospheric scattering. The functions that calculate the way light generated at the shower is projected onto the camera are in the RayTrace library and the FADCTel library simulates the electronics response of the FADC telescopes.

TRUMP's run configuration is set using a CORSIKA-style card file. The first column in each line is the name of the parameter the user wishes to set or change, followed by the list of arguments it requires. The currently installed options are described in Table 4.2. Up to three configuration files can be passed to TRUMP on the command line, which should correspond to the detector configurations that will be viewing the same sequence of simulated events. For instance, TRUMP can be run in stereo mode by providing two configuration files on the command line; one corresponding to Black Rock Mesa FD station and the other for Long Ridge. In this case, individual DST files will be generated for each configuration, since most of the simulated events will trigger only one of the two detectors.

#### **4.2.2. Air Shower Simulation**

To simulate an air shower, TRUMP first selects a random location and orientation for the shower track, using a coordinate system based on the Central Laser Facility (CLF). Impact coordinates for the shower track are chosen from a random point on the cap of a sphere of radius  $R_E$  and covering one degree of solid angle (the area within  $\sim 100$  km radius from the CLF). Even at this distance, the cap is approximately flat. Cosmic rays are assumed to have isotropic direction vectors in space, so when considering the nearly flat nature of the impact coordinates, the distribution of shower propagation directions will be evenly distributed in  $\cos^2 \theta$ . Next, primary energy is chosen from the range and power law distribution provided in the configuration file.

TRUMP allows for a broken power law distribution by defining break points and slopes in the configuration file.

Once a random energy and zenith angle are selected, a set of GH parameters are pulled from the shower library. Again, the library only includes fits to CORSIKA showers which were generated at specific energies and zenith angles. These particles produce fluorescence light via the ionization of nearby atmospheric molecules. They will also have sufficient energy to produce large numbers of Čerenkov photons. Although the Čerenkov beam is highly concentrated in the direction of shower propagation, it is bright enough that a significant fraction of the total light received at the detector will consist of scattered Čerenkov photons. Total fluorescence yield is proportional to the local ionization energy deposit, but Čerenkov yield is proportional to the number of charged particles. Nerling provides fluorescence and Čerenkov yield models which are implemented in TRUMP.

### 4.2.3. Fluorescence Yield Model

As energetic charged particles pass through the atmosphere, they transfer energy to nearby air molecules by raising their electrons to higher energy levels. Fluorescence photons are produced as the electrons de-excite. The total number of fluorescence photons that result from this ionization energy deposit is a function of the charged particle's energy as it passes through the atmosphere. Some of the Nitrogen and Oxygen electron energy levels are more efficiently excited than others, giving a wavelength-dependence to the fluorescence yield. In TRUMP, the model for total fluorescence yield comes from [35], combined with a normalized wavelength spectrum provided by FLASH [36].

Kakimoto describes an experiment in which an electron beam was passed through a chamber with a controlled atmosphere [35]. The pressure and temperature dependence of the fluorescence yield in the 300-400nm wavelength range was measured and fit to the equation,

$A_1$	$89.0 \pm 1.7 \text{ m}^2 \text{ kg}^{-1}$
$A_2$	$55.0 \pm 2.2 \text{ m}^2 \text{ kg}^{-1}$
$B_1$	$1.85 \pm 0.04 \text{ m}^3 \text{ kg}^{-1} \text{ K}^{-1/2}$
$B_2$	$6.50 \pm 0.33 \text{ m}^3 \text{ kg}^{-1} \text{ K}^{-1/2}$

**Table 4.3** Constants used in equation (4.2), taken from [35].

$$\frac{dN_{\gamma}^1}{dx} = \frac{dE^1/dx}{(dE^1/dx)_{1.4\text{MeV}}} \left( \frac{A_1}{1 + B_1 \rho \sqrt{T}} + \frac{A_2}{1 + B_2 \rho \sqrt{T}} \right) \quad (4.2)$$

which carries units of number of photons per meter per electron. The superscript ‘1’ is there to clarify that this refers to the energy deposit and fluorescence yield from a single electron.

TRUMP uses the parameters given in Table 1 of [35], restated here in Table 4.3.

The FLASH experiment was designed to independently measure air fluorescence yield which, like Kakimoto, also used a concentrated electron beam [36]. An optical filter was placed in the path between the photomultiplier and the beam in order to measure wavelength dependence. The peaks in the spectrum were identified and matched to known emission lines. In TRUMP, their relative intensities are normalized according to,

$$N \times \int_{300\text{nm}}^{400\text{nm}} \sum_i c_i \delta(\lambda - \lambda_i) d\lambda = 1 \quad (4.3)$$

where  $\delta$  is the Kronecker delta function and the summation is done over the emission lines at wavelengths  $\lambda_i$  with relative intensities  $c_i$  (see Figure 4.2). The specific normalization over wavelengths from 300-400nm is important if the FLASH results are to be used with Kakimoto.

It was determined by FLASH that the relative intensities of the emission lines had very weak dependence on pressure, temperature or electron energy [36]. It is therefore acceptable to treat the total fluorescence yield as a function that is separable in wavelength, rate of ionization energy deposit and height (for combined pressure and temperature dependence).

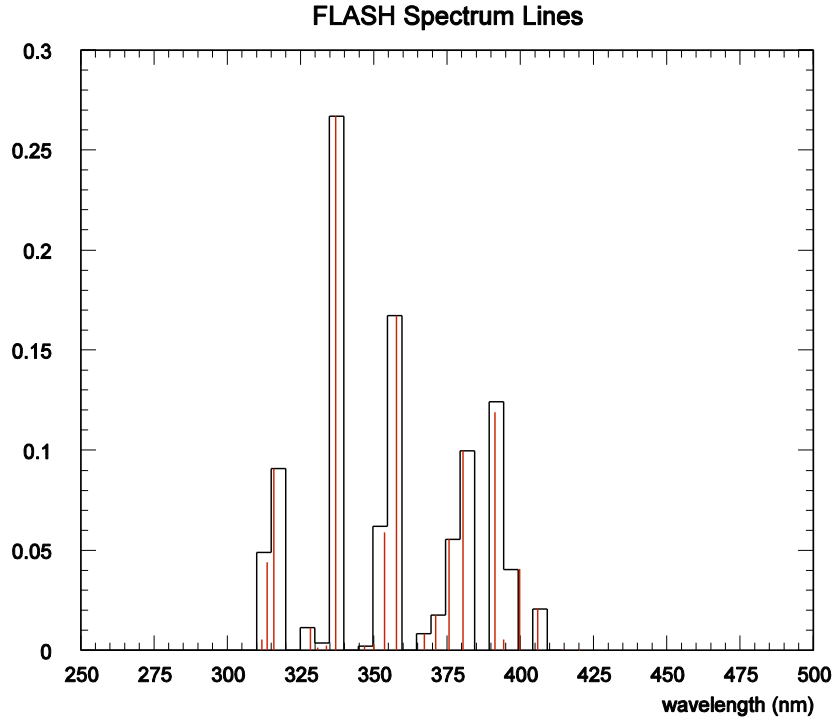


**Figure 4.2** Fluorescence Spectrum Lines. The red lines indicate the spectrum lines themselves. This histogram is their sum in 5 nm bins.

#### 4.2.4. Energy Deposit Model

It has been shown that there is a linear dependence between fluorescence yield and ionization energy deposit. To complete the connection between fluorescence production and charged particle population at the shower, the relationship between energy deposit rate and the Gaisser-Hillas function must be established. The GH formula describes the number of charged particles present in the shower as a function of slant depth  $X$ . The total ionization energy deposit rate will be the sum of the energy deposit rates of the individual charged particles,

$$\frac{dE_{\text{dep}}}{dX}(X) = \sum_{k=1}^{N_{\text{spec}}} \sum_{i=1}^{N_k} \left( \frac{dE^1}{dX}(E_i) \right)_k. \quad (4.4)$$

The double-summation reflects the differing energy loss rates between particle species. Consider just one species, with the summation binned according to energy,

$$\frac{dE}{dX}(X) = \sum_{j=1}^{N_{\text{bin}}} N_j \cdot \frac{dE^1}{dX}(E_j) \Rightarrow \int_0^{N_k} \frac{dE^1}{dX}(E) dN. \quad (4.5)$$

With a simple change of variables, this is transformed to an integral over energy,

$$\frac{dE}{dX}(X) = \int_0^{\infty} \frac{dN}{d \ln E}(X, E) \cdot \frac{dE^1}{dX}(E) d \ln E. \quad (4.6)$$

The differential charged particle energy spectrum can be normalized to the total number of particles of species  $k$ ,

$$\frac{dE}{dX}(X) = N_k(X) \int_0^{\infty} f(X, E) \frac{dE^1}{dX}(E) d \ln E = N_k(X) \alpha_k(X) \quad (4.7)$$

where  $\alpha_k(X)$  stands for the mean ionization loss rate for particles of type  $k$  at slant depth  $X$ . In general, the total energy deposit may be expressed as the product of the average of the  $\alpha_k$ 's, weighted by the relative abundance of  $N_k$ 's. That is,

$$\frac{dE_{\text{dep}}}{dX}(X) = N_{\text{ch}}(X) \cdot \alpha(X). \quad (4.8)$$

Nerling demonstrates that  $\alpha$  may be estimated by analyzing the profiles of air showers simulated with CORSIKA with one major caveat [34]. It would be computationally prohibitive for CORSIKA to track every single particle produced in an extensive air shower. The simulation therefore requires the user to provide a cutoff energy, depending on the particle type, below which the particles in that class are no longer tracked. After each shower simulation, tables are generated of particle number and total energy deposit as functions of slant depth. The particle number tables do not account for particles below the cutoff energy, but the energy deposit profiles include these particles by considering their most probable fate. Nerling compensates for this by defining an effective mean ionization loss rate for particles above the cutoff energy,

$c_1$	3.90883
$c_2$	1.05301
$c_3$	9.91717
$c_4$	2.41715
$c_5$	0.13180

**Table 4.4** Constants used to parameterize  $\alpha_{\text{eff}}$  in [34] and this analysis.

$$\alpha_{\text{eff}}(s; E \geq E_{\text{cut}}) \equiv \frac{1}{N_{\text{ch}}(X; E \geq E_{\text{cut}})} \cdot \frac{dE_{\text{dep}}}{dX}(X) \quad (4.9)$$

where the shower age parameter  $s = 3X/(X + 2X_{\text{max}})$ . The functional form for  $\alpha_{\text{eff}}$  provided by Nerling is,

$$\alpha_{\text{eff}}(s) = \frac{c_1}{(c_2 + s)c_3} + c_4 + c_5 s. \quad (4.10)$$

The constants used for this analysis, which also come from Nerling et al., are shown in Table 4.4. They are specific to CORSIKA simulations using a 1 MeV cutoff energy for electrons and do not show any dependence on primary particle species or shower zenith angle.

#### 4.2.5. $\hat{C}$ erenkov Model

The charged particles in an extensive air shower produce a highly collimated beam of  $\hat{C}$ -erenkov radiation during shower development. As is shown in Figure 4.3, so much is produced that a significant amount of  $\hat{C}$ erenkov light gets scattered into the detectors' fields of view. Therefore, a complete FD simulator must include the effects of  $\hat{C}$ erenkov radiation. For this, TRUMP also uses the models described in [34].

$\hat{C}$ erenkov yield depends mainly on the number of charged particles present and the index of refraction of light. The total number of  $\hat{C}$ erenkov photons produced per charged particle per radiation length with wavelengths between  $\lambda_1$  and  $\lambda_2$  is approximately,

$$Y_{\hat{C}_v} = \frac{2\pi\alpha Z^2}{\rho} \int_{\lambda_1}^{\lambda_2} \left(1 - \frac{1}{n^2\beta^2}\right) \frac{d\lambda}{\lambda^2} \approx \frac{2\pi\alpha Z^2}{\rho(h)} \left(2\delta(h) - \frac{m^2 c^4}{E^2}\right) \left(\frac{1}{\lambda_1} - \frac{1}{\lambda_2}\right). \quad (4.11)$$

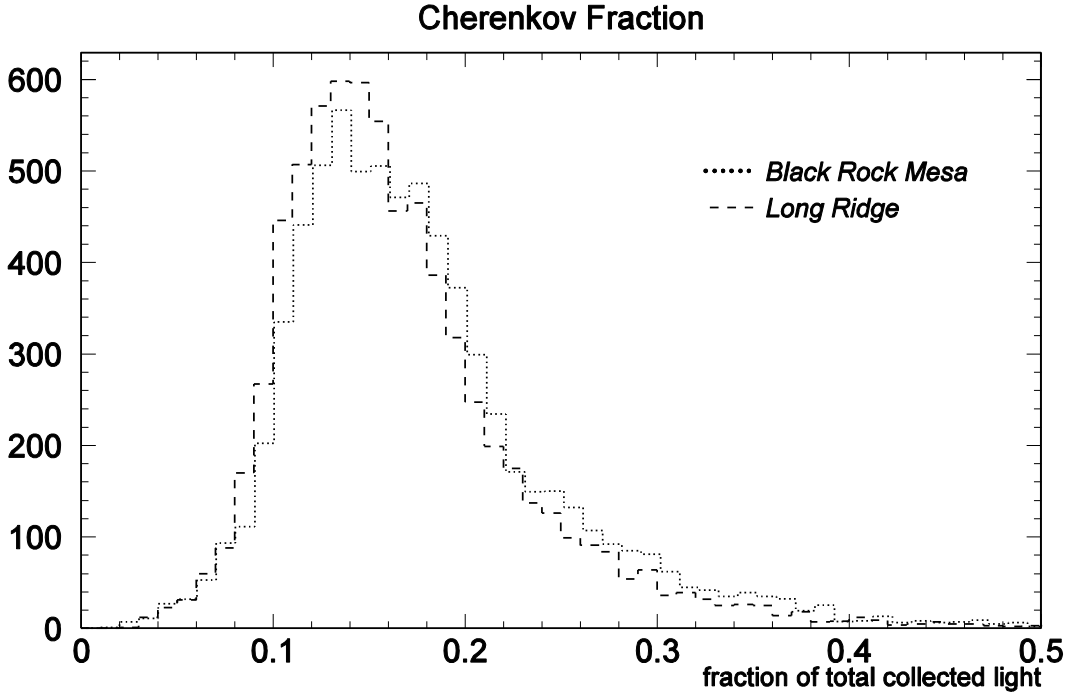


**Figure 4.3** Contribution of  $\hat{C}$ erenkov light to the total light collected for each event.

Here,  $\delta(h)$  is the index of refraction minus 1 and  $\alpha$  is the fine structure constant. Less than 3% of the energy deposited by charged air shower particles responsible are heavier than electrons [12], so the approximations  $N_{\text{ch}} \approx N_e$  and  $m \approx m_e$  are used here. The total number of  $\hat{C}$ erenkov photons produced near the shower axis at slant depth  $X$  is the convolution of equation (4.11) with the differential electron energy spectrum,  $f_e$ ,

$$\frac{dN_{\hat{C}_v}}{dX}(\lambda, h, X) = N_{\text{ch}}(X) \int_{E_{\text{thr}}}^{\infty} f_e(s, E) Y_{\hat{C}_v}(h, \lambda, E) d\ln E \quad (4.12)$$

where,

$$f_e = \frac{1}{N_{\text{ch}}(X)} \frac{dN_e}{d\ln E}(s, E) \quad (4.13)$$

and,

$$E_{\text{thr}} = \frac{m_e c^2}{\sqrt{2\delta(h)}} \quad (4.14)$$

The number of charged particles comes from the Gaisser-Hillas formula which does not account for below-cutoff particles in the CORSIKA simulations. This is compensated for by the normalization of  $f_e$ , which is well described by the formula,

$$f_e(s, E) = \frac{a_0 E}{(a_1 + E)(a_2 + E)^s} \quad (4.15)$$

with,

$$\begin{aligned} a_1 &= 6.42522 - 1.53183 \cdot s, \\ a_2 &= 168.168 - 42.1368 \cdot s, \text{ and} \\ a_0 &= 0.145098 \cdot \exp(6.20114 \cdot s - 0.596851 \cdot s^2). \end{aligned} \quad (4.16)$$

The term  $a_0$  determines the overall normalization of  $f_e$ , hence the coefficients in that term depend on the choice of electron cutoff energy in CORSIKA.

Unlike fluorescence, which is emitted isotropically,  $\hat{C}$ erenkov light is highly focused in the direction of shower development. Nerling also describes a functional form for the angular dependence of  $\hat{C}$ erenkov emission, but we prefer to use the “traditional” form,

$$A(E_{\text{thr}}, \theta) = \frac{1}{\theta_c} e^{-\theta/\theta_c}, \quad \theta_c = 0.83 E_{\text{thr}}^{-0.67} \quad (4.17)$$

where  $E_{\text{thr}}$  is the threshold energy for  $\hat{C}$ erenkov production described earlier.

#### 4.2.6. Simulation of Atmospheric Conditions

Variability in the atmosphere is the greatest source of systematic uncertainty in fluorescence detector experiments. The most critical parameters in shower energy estimation depend on local molecular density and temperature. Additionally, scattering phenomena have a significant impact on the relationship between the collected light and that produced at the shower track.

##### 4.2.6.1. Molecular Atmosphere

TRUMP is typically run using real time Radiosonde data from NOAA’s IGRA database. Temperature, altitude and dew point temperature data is taken at several critical pressure levels,

which are roughly evenly spaced in  $\ln P$ . Of the thousands of Radiosonde launch sites in the database, Salt Lake City Utah, Elko Nevada, and Flagstaff Arizona are the closest to Telescope Array. This analysis uses only data from the Salt Lake City station. A separate program generates a DST file from the Radiosonde data, which is in ASCII format. Radiosonde balloons are launched every 12 hours and it is assumed that the temperature and pressure profiles do not vary much during the periods between balloon flights.

TRUMP's routines query the Radiosonde database DST file with a date, time, and altitude. If the altitude falls within the range of data points for a given set of soundings, then temperature and pressure data are interpolated according to,

$$T(z) = T_b \frac{z_t - z}{z_t - z_b} + T_t \frac{z - z_b}{z_t - z_b} \quad (4.18)$$

and,

$$\ln \frac{P(z)}{P_b} = \begin{cases} -\frac{gM}{R} \frac{(z - z_b)}{T_b}, & T_t = T_b \\ -\frac{gM(z_t - z_b)}{R(T_t - T_b)} \ln \left( \frac{T(z)}{T_b} \right), & T_t \neq T_b \end{cases} \quad (4.19)$$

Here, subscripts  $t$  and  $b$  indicate parameter values at the first data point above and below the requested altitude, respectively. The constant  $M = 28.9644$  g/mol is used for the average molecular weight of air, which is accurate to an altitude of about 80 km.  $R$  is the ideal gas constant and  $g$  is the acceleration of gravity at sea level. Since gravity is a function of altitude, a transformation to coordinates of *geopotential* altitude is made, where  $g$  is constant. The use of  $z$  to represent altitude instead of the  $h$  used before is meant to reflect that difference. Density follows from plugging  $T$  and  $P$  into the ideal gas equation.

If the queried altitude falls outside of the range of data points from the Radiosonde soundings, then standard atmospheric conditions are applied. Temperature is linearly extrapolated from the nearest data point using gradients of 0 and  $-6.3$  K/km for altitudes above and below

the outer-most data points, respectively. Pressure can also be determined using the same values for temperature gradient and setting  $P_b$  to the nearest data point. Like before, density is found by putting these into the ideal gas formula.

#### 4.2.6.2. Scattering and Attenuation of Light

Scattering phenomena are responsible for both the reduction of light observed from the shower and the contribution of the Čerenkov beam observed at the detector. Rayleigh and Aerosol scattering are the dominant effects, with Rayleigh playing a more significant role.

In terms of its contribution to attenuation, Rayleigh scattering follows an exponential decay in radiation length with a  $\lambda^4$  dependence, computed from the formula,

$$f_{\text{ray}}(\Delta X, \lambda) = 1 - \exp \left[ -\frac{\Delta X}{2969.6 \text{ g/cm}^2} \cdot \left( \frac{400 \text{ nm}}{\lambda} \right)^4 \right] \quad (4.20)$$

where  $\Delta X$  is the matter between two points in the atmosphere and  $\lambda$  is the wavelength of the light being attenuated. The equation,

$$\phi_{\text{ray}}(\theta) = \frac{3}{16\pi} (1 + \cos^2 \theta) \quad (4.21)$$

is used for the angular dependence.

Dust in the atmosphere also has a significant impact on the attenuation of light from the shower. How light is scattered by aerosols and how much depends on the shape and density of the dust particles and is very difficult to model exactly. A special case of aerosol scattering is used here called Mie Scattering, which treats the particles as dielectric spheres. This dictates the functional form for the scattering model used, but the coefficients in the formulae come from experimental measurements. Aerosol scattering is accounted for in TRUMP by applying the attenuation factor,

$$f_{\text{Mie}} = \exp \left( -\frac{(e_1 - e_2)h_s}{\lambda_{\text{Mie}} \cos \theta} \right) \quad (4.22)$$

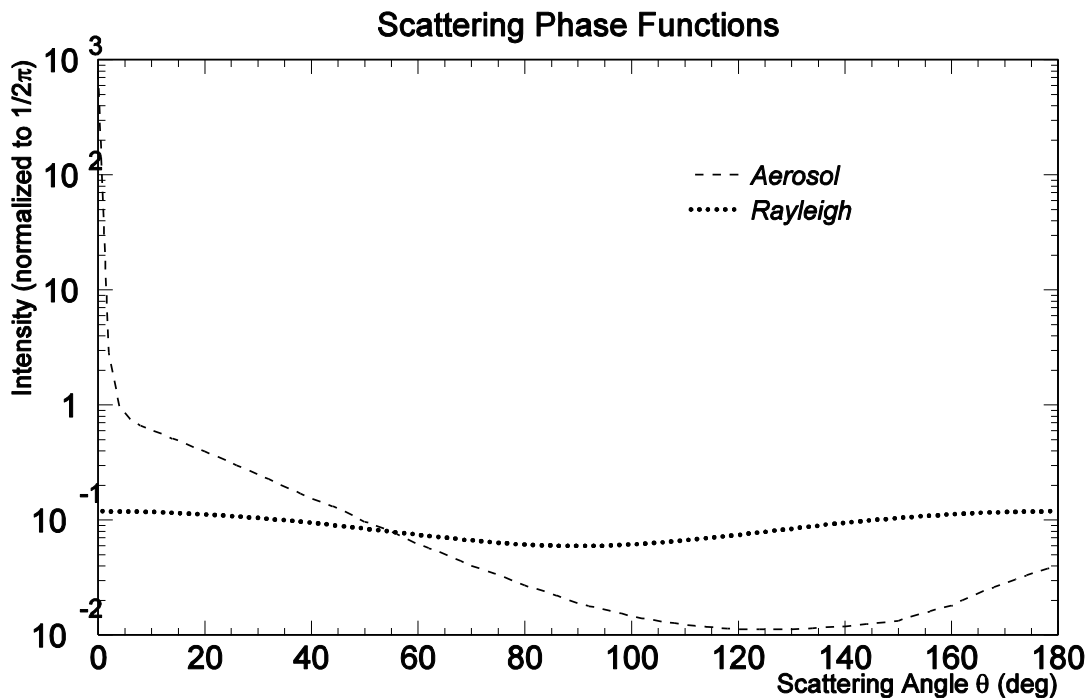


**Figure 4.4** Rayleigh and Aerosol scattering phase functions, normalized so that the integral of the scattering amplitude over all solid angles is unity.

where  $h_s = 1$  km,  $\lambda_{\text{Mie}} = 29.4$  km, and

$$e_1 = e^{-\frac{h_1}{h_s}}, \quad e_2 = e^{-\frac{h_2}{h_s}} \quad (4.23)$$

where  $h_1$  and  $h_2$  are the altitudes of the path's endpoints for which attenuation is computed. The phase function does not have an analytical form. Instead, the Longtin Desert phase function [37] is used, shown in blue in Figure 4.4, with log-linear interpolation.

#### 4.2.7. Ray Tracing

TRUMP simulates an extensive air shower by dividing its length into one  $\text{g/cm}^2$  segments. The Gaisser-Hillas formula (Equation (1.14)) is used to compute the average number of charged particles  $N'(X)$  present within the segment. The prime denotes this is an effective number of charged particles, specifically the number above the cutoff energy used when generating

the shower library. The local ionization energy deposit is found by multiplying  $N'$  by  $\alpha_{\text{eff}}$ , using the prescription provided by [34], necessary for computing the fluorescence yield.  $N'$  is also used for calculating Čerenkov light, which is aggregated through the sequence of shower segments. A table of numbers of photons and thickness of the cylindrical slab-shaped shower segments is produced by TRUMP's air shower generator routines, which are then passed to the ray tracing process.

The ray tracing functions compute how much light the fluorescence detectors will collect from an extensive air shower. The atmospheric attenuation factors and number of observed photons are computed, based on the orientation of the mirrors relative to the track and distance to the track segments. To improve simulation speed, Paraglas and BG3 filter transmittance, mirror reflectance and quantum efficiency are applied since these are not geometry-dependent factors. The coordinate for each photoelectron's source is chosen at random from within each shower segment. They are evenly distributed parallel to the shower axis and the NKG function described by [38] is used for the lateral distribution. The destination coordinate is a randomly selected point on an imaginary disk in front of the mirror.

Rays are rejected if their paths cross the camera or its support structure, if they do not land on any of the mirror segments or if their projection onto the focal plane does not fall within the active area of any PMTs. The product of the ray tracing phase of the simulation is a sorted list of photo-electron arrival times, indexed by camera and PMT ID number.

#### **4.2.8. Electronics Simulation**

TRUMP's routines for simulating detector electronics produce FDRaw DST banks from the lists of photo-electron arrival times generated during ray tracing. It functions, logically, just like the real detector electronics. Memory is allocated for the FADC buffers of every channel of each camera which might receive some light from the simulated shower. Frames of 256 time slices are searched for signals above threshold and are advanced in steps of 128 time slices. If

signals are identified in five contiguous channels from one camera or three contiguous channels in the edges of each of two adjacent cameras, then the data is passed through the same pre-processing algorithm used by TAMA. There are, however, some nuances in the real hardware which cannot be simulated, mainly from noise in the electronics.

The fluctuations in the waveform come from electrical noise, night sky background, and signal PE. The signal from a single photo-electron is shaped and smeared by the circuit which connects the photomultiplier to the FADC chip. While every component in the circuit has some impact on its response function, the two most significant factors come from the shaper amplifier and the transit time spread from the PMT. The shaper circuit is a second-order Butterworth filter with a 50 ns time constant which determines the general shape of the pulse received at the FADC chip. The transit time spread for the Hamamatsu PMTs is approximately a 5 ns wide Gaussian which is delayed 50 ns from the true photon arrival time. This modifies the pulse shape by pushing the rise time back slightly and forcing the pulse to fall back to zero more quickly.

The accuracy of our modeling of the electronics was tested by comparing the correlation coefficients of the FADC between a given time slice and the first, second and third subsequent time slices. This autocorrelation is caused by the Butterworth filter and changes the shape of the distribution of raw background data counts (see Appendix B for a mathematical description). Since the signal digitizer-finder uses a signal-to-noise based threshold, the potential for arriving photons to trigger a photomultiplier tube is dependent on how the noise is characterized. If this is not simulated accurately then the calculation of detector aperture will be wrong. The effective shaper circuit time constant and transit time spread in the simulation were adjusted until the waveform power spectra matched in data and Monte Carlo. A detailed description of how the impulse response function was derived and how it is implemented in TRUMP is provided in Appendix C.

There are several sources of noise which contribute to the waveform as a whole. Night sky background light is Poisson-distributed and will vary from tube to tube, since some channels will have UV bright stars in their field of view. The average night sky background per tube is estimated by analyzing the mean and variance of FADC in non-signal channels in raw data. A study was done on the electrical noise, which was found to have a regular periodic behavior and is consistent across all channels and cameras. The average is stored as an array which gets added to the simulated waveform at the end.

### **4.3. Data-Monte Carlo Comparisons**

The strength of our result hinges on the quality of our simulation. To verify how effectively the simulation reflects reality, the results are compared to data at many levels. In a typical Data-Monte Carlo comparison, the distribution of some parameter is chosen for comparison. The Monte Carlo distribution is normalized to the number of entries in the corresponding distribution from the data and their histograms are shown in the same figure, with the MC distribution represented as a histogram and the data shown as points with error bars. Their bin-by-bin ratio is taken and fit to a linear function. If there is perfect agreement, then the fit will be a horizontal line at unity. A sample of these comparisons is shown at the end of this section.

The lowest level that a comparison can be made with data is the raw FADC level. Time slice correlation, for example, is important because channels trigger the SDF when they receive a significant signal over a short period of time. If the waveform simulation did not consider pulse shaping, then larger signals would be required for triggering and trigger aperture would be underestimated. Data-Monte Carlo comparisons for electronics simulation include autocorrelation in the waveform data, distributions of signal and noise tubes and mean and variance of noise tubes. Figure 4.5 shows data-Monte Carlo comparisons for the waveform power spectra, computed with FFT, at Black Rock Mesa and Long Ridge FD stations.

Because cosmic rays arrive isotropically, more or less, the distribution of their impact parameters,  $R_p$ , will increase linearly with distance from the fluorescence detector. However, the distribution of *observed*  $R_p$  will only increase up to some distance, then begin to fall off because the detector is not sensitive enough to reconstruct those events. The direction of shower propagation is also important for event reconstruction. Fluorescence detectors favor events that produce longer tracks over longer time periods, which tend to be high-energy events propagating perpendicularly to the detectors' fields of view. Good data-Monte Carlo comparisons of  $R_p$  and  $\psi$  are crucial because they go directly into the calculation of detector aperture. Furthermore, estimates of  $N_{\max}$ ,  $X_{\max}$  and energy depend on reconstructed geometry, so if the  $R_p$  and  $\psi$  distributions don't match between data and simulation, then neither will  $N_{\max}$  or  $X_{\max}$ . Figure 4.6 and Figure 4.7 show data-Monte Carlo comparisons of  $R_p$  and  $\psi$  distributions for events with reconstructed energies above  $10^{17.5}$  eV.

Assuming the other aspects of the simulation are correct, the profile data-Monte Carlo comparisons will indicate how well the physics are being modeled. Atmospheric conditions and scattering will impact  $X_{\max}$  distributions and the shape of the energy spectrum we throw in our simulation will be reflected in the energy and  $N_{\max}$  distributions. Figure 4.8 and Figure 4.19 are the data-Monte Carlo comparison plots for  $X_{\max}$  and  $N_{\max}$  distributions.

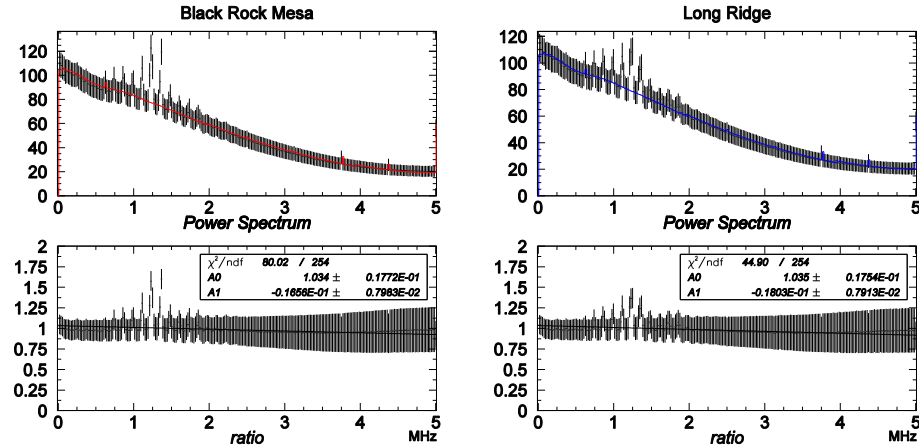


Figure 4.5 Data-Monte Carlo comparison of waveform power spectra. The spikes near 1.25 MHz represent a  $1.6 \mu\text{s}$  square pulse firing with a period of  $80 \mu\text{s}$ , possibly from the FPGA.

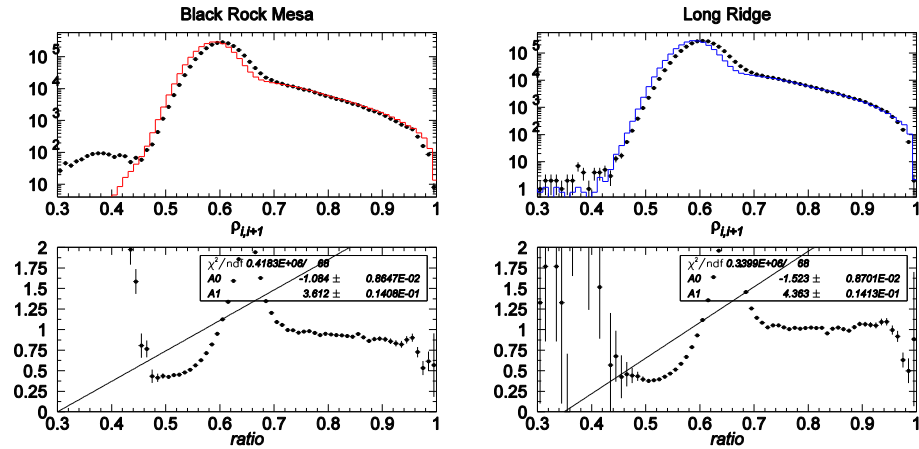


Figure 4.6 Waveform autocorrelation between each time bin with the next ( $\log E > 17.5 \text{ eV}$ ).

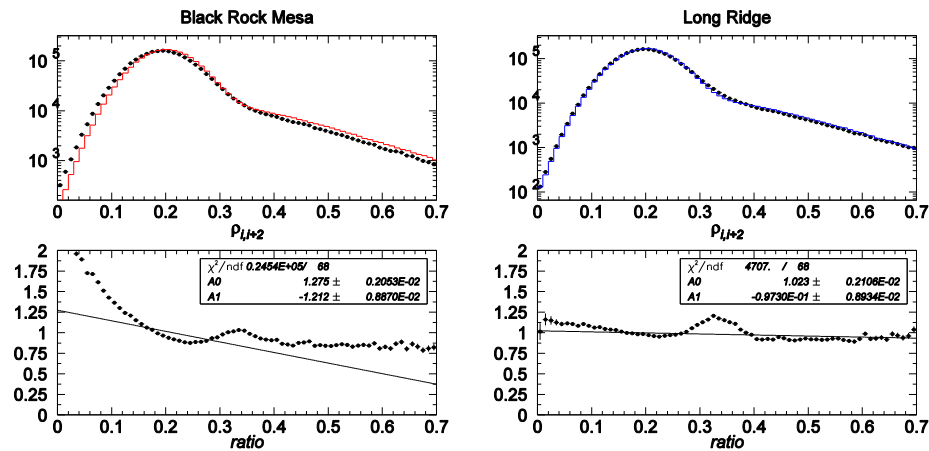


Figure 4.7 Waveform autocorrelation between time bins separated by 200ns ( $\log E > 17.5 \text{ eV}$ ).

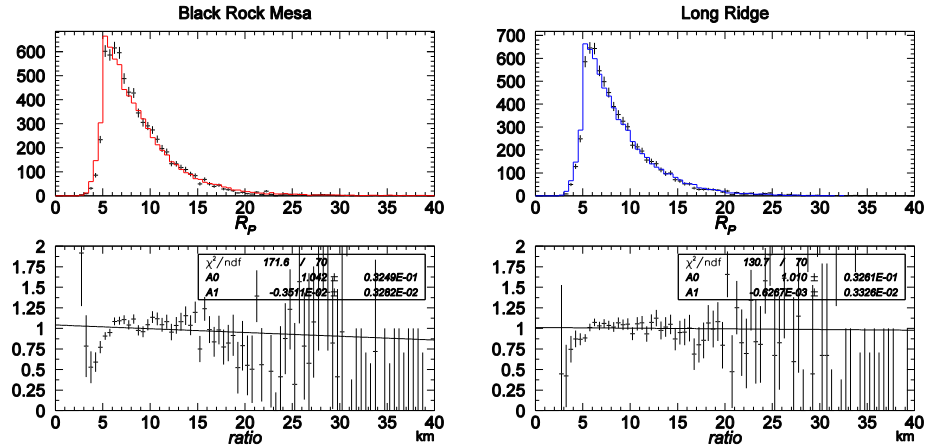


Figure 4.8 Data-Monte Carlo comparisons of  $R_P$  distributions ( $\log E > 17.5\text{eV}$ ).

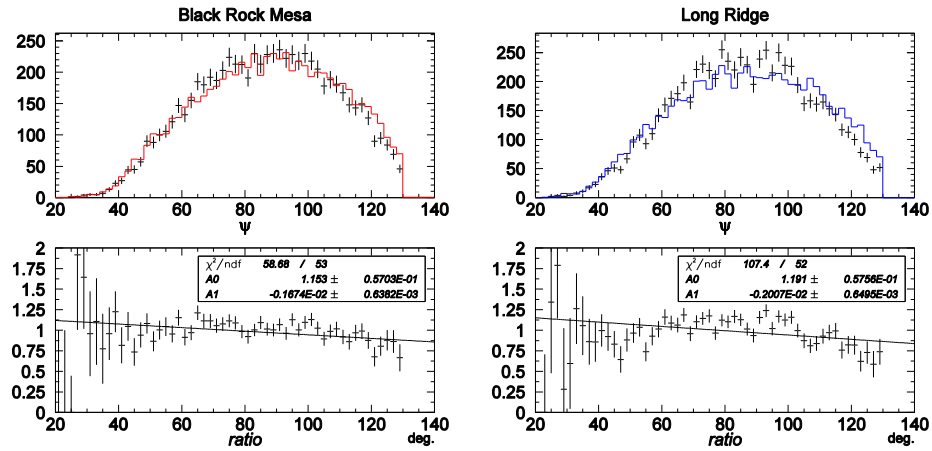


Figure 4.9 Data-Monte Carlo comparisons of  $\psi$  distributions ( $\log E > 17.5\text{eV}$ ).

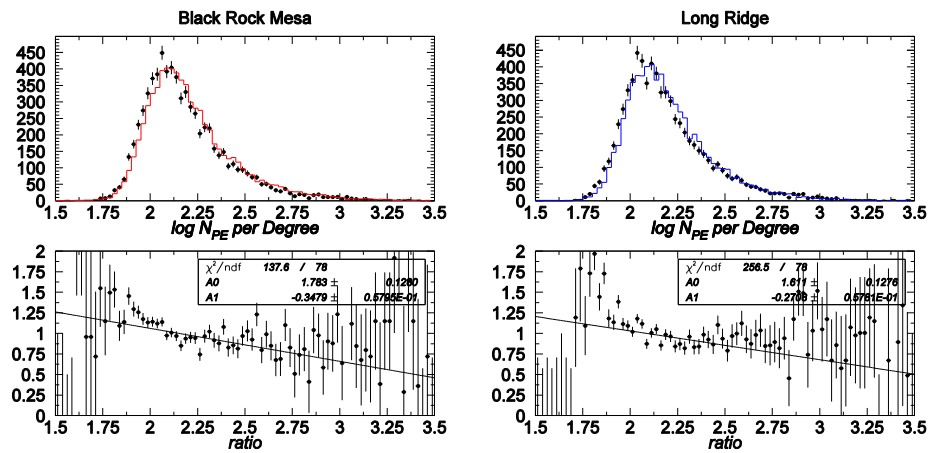


Figure 4.10 Data-Monte Carlo comparisons of  $\log(N_{PE}/\text{deg})$  ( $\log E > 17.5\text{eV}$ ).

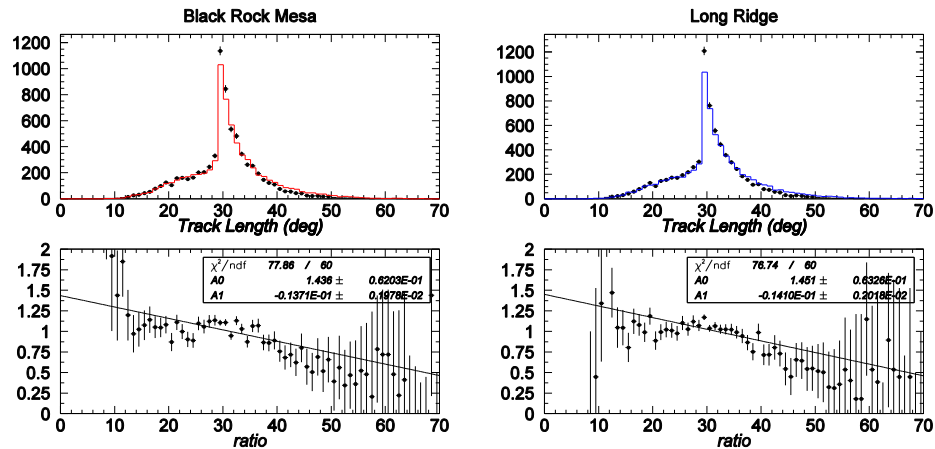


Figure 4.11 Data-Monte Carlo comparisons of track length distributions ( $\log E > 17.5\text{eV}$ ).

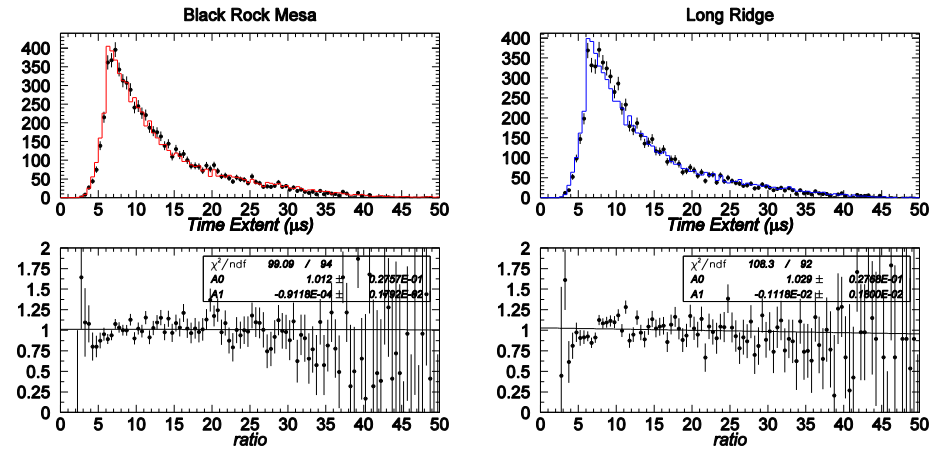


Figure 4.12 Data-Monte Carlo comparisons of event duration ( $\log E > 17.5\text{eV}$ ).

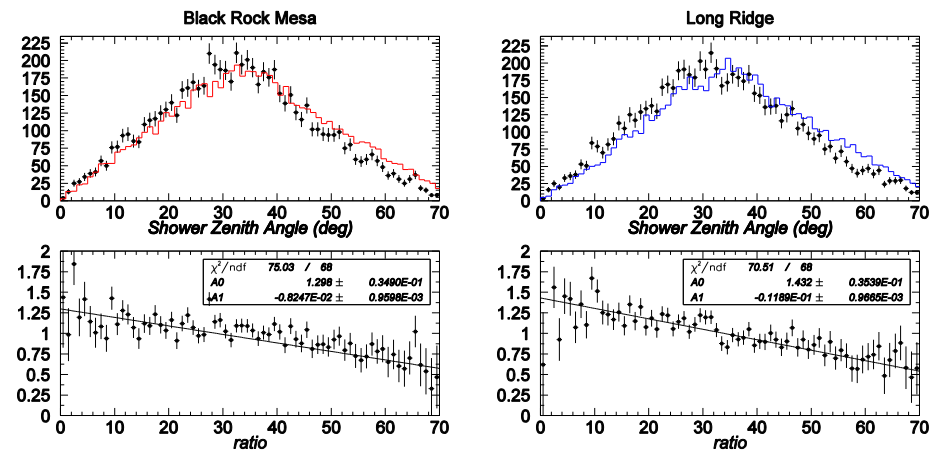


Figure 4.13 Data-Monte Carlo comparisons of zenith angle distributions ( $\log E > 17.5\text{eV}$ ).

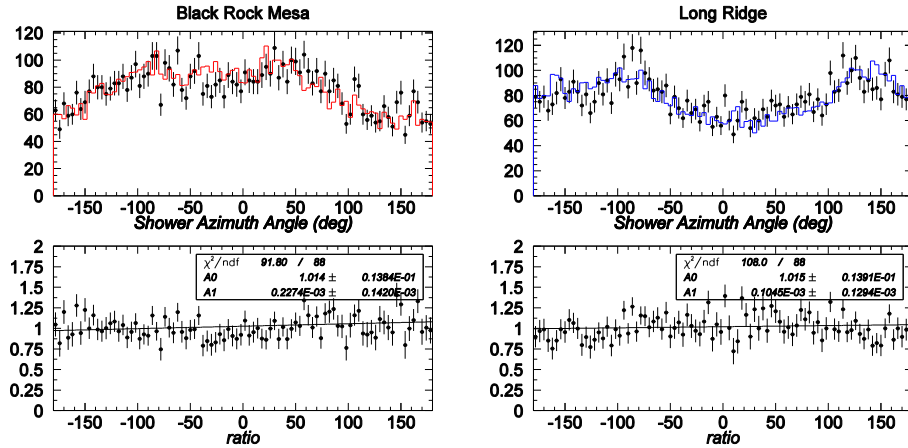


Figure 4.14 Data-Monte Carlo comparisons of shower azimuthal direction ( $\log E > 17.5\text{eV}$ ).

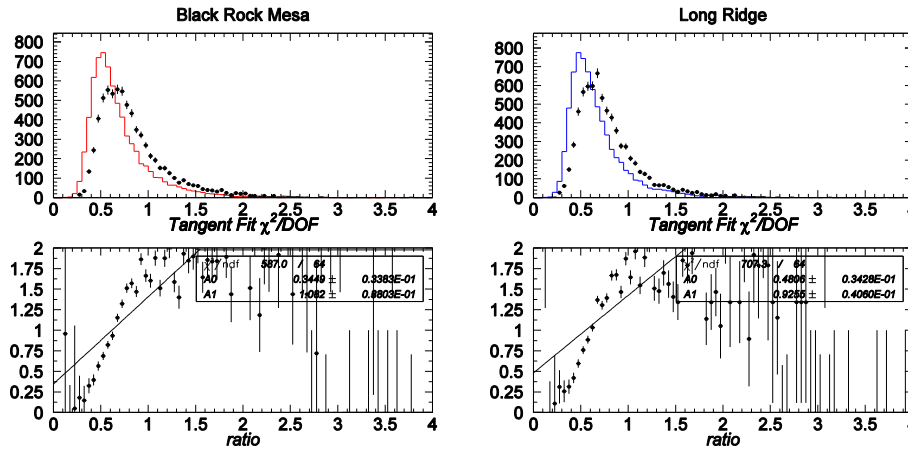


Figure 4.15 Data-Monte Carlo comparisons of the tangent fit  $\chi^2/\text{DOF}$  ( $\log E > 17.5\text{eV}$ ).

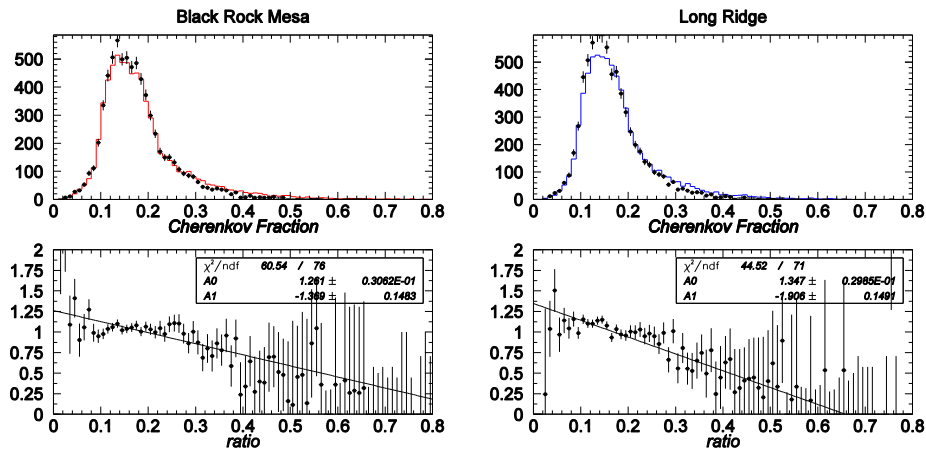


Figure 4.16 Data-Monte Carlo comparisons of Cherenkov fraction distributions ( $\log E > 17.5\text{eV}$ ).

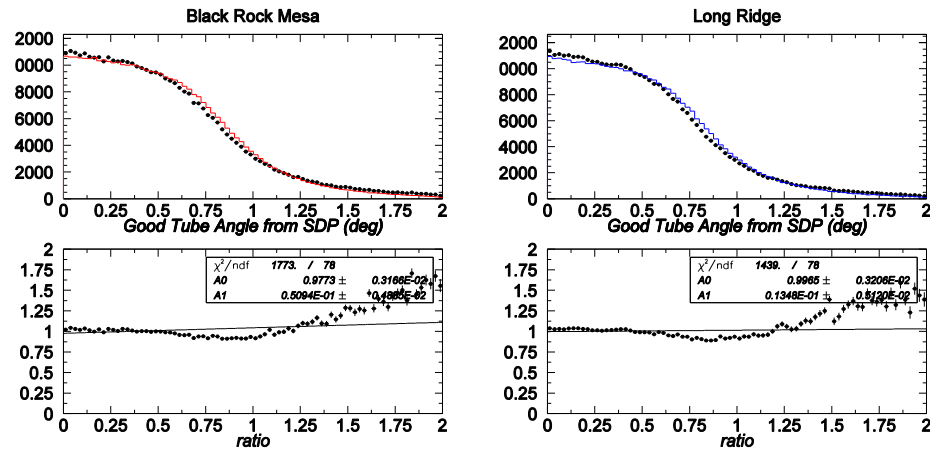


Figure 4.17 Data-Monte Carlo comparisons of good tube viewing angle from the shower-detector plane ( $\log E > 17.5\text{eV}$ ).

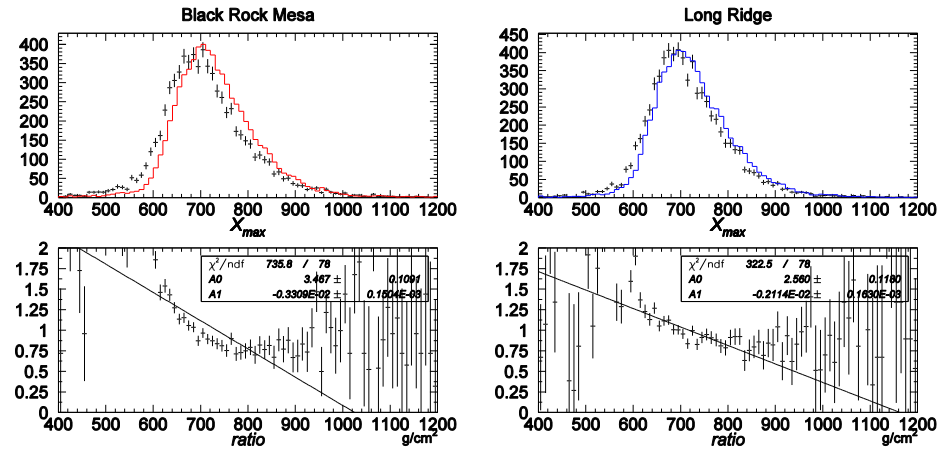


Figure 4.18 Data-Monte Carlo comparisons of  $X_{\max}$  distributions ( $\log E > 17.5\text{eV}$ ).

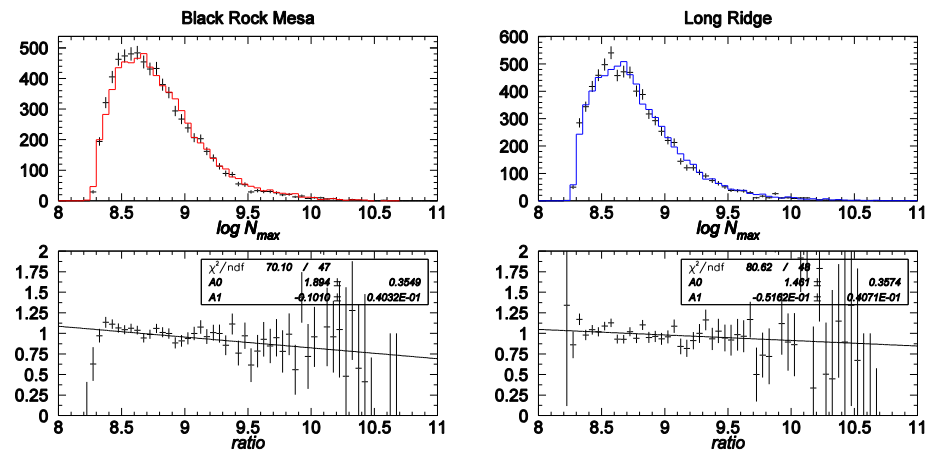


Figure 4.19 Data-Monte Carlo comparisons of  $N_{\max}$  distributions ( $\log E > 17.5\text{eV}$ ).

## Chapter 5. Measurement of the UHECR Flux

### 5.1. Monocular Energy Spectrum Measurement

#### 5.1.1. Data Set

The FDs at Black Rock Mesa and Long Ridge began taking data in November 2007. In the months that followed, adjustments were made to the hardware, firmware and software to tune the detectors' performance, which were carefully noted and accounted for in the calibration data set. However, to avoid including these systematic issues, data collected before March 21, 2008 has been excluded from this work. The end point for this data set is determined by the latest update of the calibration database to date, September 6, 2011. After eliminating poor-weather data and runs where the hardware appeared to be unstable, the set includes about 3800 cumulative hours of data Black Rock Mesa and Long Ridge FD stations. The general statistics of this data set are shown in Table 5.1.

	Black Rock Mesa	Long Ridge
Data period	3/29/2008 – 9/6/2011	3/30/2008 – 8/8/2011
good weather nights	436	417
good runs	4581	3793
Gross on-time	2077.00hr	1727.27hr
Dead time	7.6%	8.7%
triggers	$17.3 \times 10^6$	$16.2 \times 10^6$
downward events	835,195	806,597
good geometry	10,983	10,441
good events	7318	7479

**Table 5.1** Statistics for the good-weather data collected by BRM and LR FD stations.

Figure 5.1 and Figure 5.2 give a measure of the detectors' overall operating efficiency. Unlike the surface detectors, which can be constantly running, fluorescence detectors can only be operated on clear, moonless nights. The solid curve in Figure 5.1 is the total dark time, without poor-weather nights factored in. Furthermore, FDs are not run on nights with less than three hours of

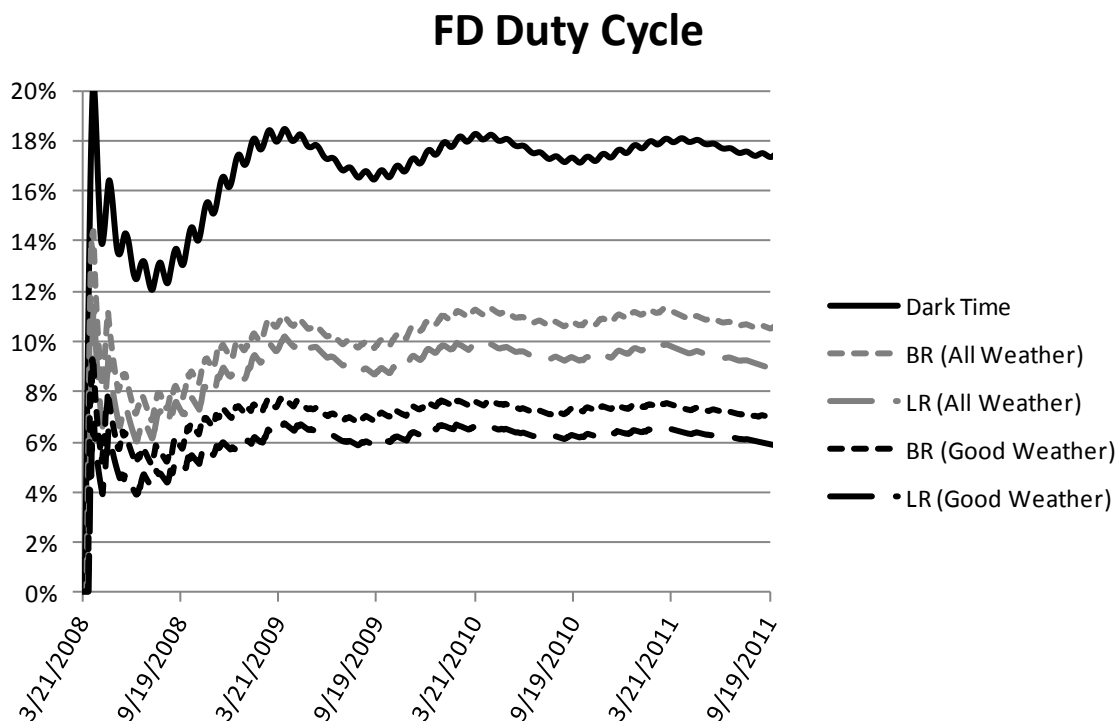


**Figure 5.1** FD duty cycle. Fluorescence detectors can only be run on clear, moonless nights. After accounting for technical issues, periodic breaks for calibration runs and early shut-downs due to poor weather conditions, the FD duty cycle is typically 10%.

potential dark time, so even the “all-weather” run time is much smaller than the available dark time. For a large part of this data period, the Long Ridge station required individuals to be on-site in order to operate the detector. Notice in Figure 5.1 that Long Ridge’s duty cycle is systematically smaller than that of Black Rock Mesa. There are two reasons for this difference. For the first half of the period covered in this work, Long Ridge operators there were required to hold off data collection until they received word that Black Rock Mesa station was actively taking data. Eventually, systems were put into place that allowed Long Ridge station to be run remotely. However, operators were still required to shut the site down 90 minutes earlier than BRM, in case either the bay doors failed to close or the connection was lost. This would allow time for the operators to drive out to the site and protect the equipment from sunlight. The oscillations in the plots are an artifact of taking time averages. The high-frequency oscillations correspond to individual observation periods (lunar cycle) and the lower frequency oscillations come from seasonal

dark time.

Figure 5.3 shows the distribution of primary energies of cosmic ray events observed at Black Rock Mesa and Long Ridge. The drop-off at low energies reflects the combined effect of detector sensitivity and reconstruction efficiency. You will notice that there are more events in the final data set from Long Ridge, compared to Black Rock, despite having a shorter on-time and greater dead time fraction. Even though they are the same detector by design, there are systematic differences which allow for this to happen. For example, if the PMT gains are higher or the mirrors tend to stay cleaner longer at LR, then it would tend to have greater trigger efficiency than BR. If the detector geometry or atmospheric conditions near LR more closely match those in the Monte Carlo, then a greater fraction of events will pass the quality cuts. It is likely that some mixture of these effects is responsible for the difference in observed low-energy events.

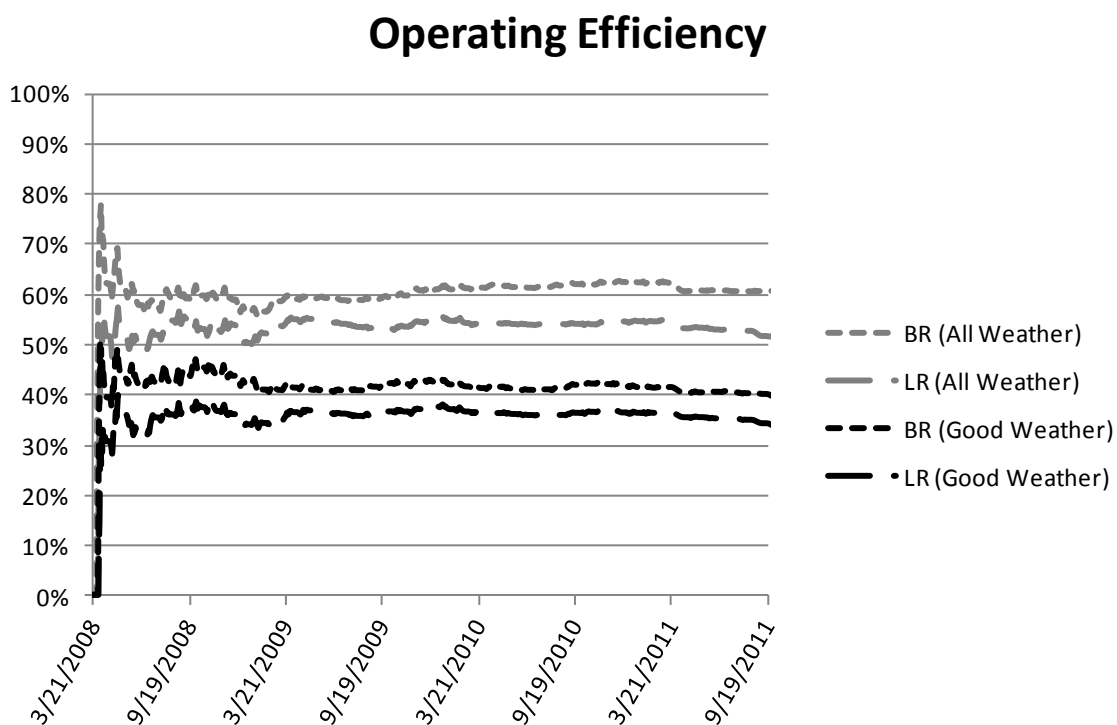


**Figure 5.2** Fraction of dark period when the detectors were actually taking data. LR is systematically lower than BRM because it is more remote and operators there need to stand by until the shift leader at BRM signals the go-ahead to begin observation. Note that this also includes reductions due to poor weather.

### 5.1.2. Aperture

The term *aperture* is used here to describe the observable parameter space of extensive air shower positions and orientations. For fluorescence detectors, this space consists of the directions from which cosmic rays are arriving and the locations where their trajectories cross the Earth's surface. Since brighter showers can be seen farther from the detector, aperture increases with cosmic ray energy, but there is also a dependence on the orientations of the shower axes. This complex interdependence between energy and angle means that aperture must be calculated using the Monte Carlo method.

In TRUMP, air showers are simulated with an isotropic distribution of propagation directions with zenith angles up to  $80^\circ$ . Random shower core positions, the points where the shower trajectories intersect with the ground, are evenly distributed within a one-degree circle on the Earth's surface centered at the CLF. Together, this defines a parameter space far beyond that in which the detectors are truly sensitive, the volume of which is found by integrating,

$$A\Omega = \int_{0^\circ}^{1^\circ} R_E^2 \cos \alpha \, d\alpha \int_{0^\circ}^{80^\circ} \cos^2 \theta \, d\theta \, d\phi = 118,348 \text{ km}^2 \text{ sr.} \quad (5.1)$$

Here,  $R_E = 6370.9843 \text{ km}$ , the mean radius of the Earth at  $39.29693^\circ\text{N}$  latitude plus  $1382 \text{ m}$  altitude.

The fraction of simulated showers which trigger the detector and pass through the full chain of analysis and quality cuts is called the *acceptance*, which may be described by the matrix  $H_{ij}$  such that,

$$N_i = \sum_j H_{ij} \mathcal{N}_j \quad (5.2)$$

where  $N_i$  is the number of events seen with reconstructed energies between  $E_i$  and  $E_i + \Delta E_i$  and  $\mathcal{N}_j$  is the number of events thrown into  $A\Omega$  with true energies between  $E_j$  and  $E_j + \Delta E_j$ . In the limit of energy resolution  $\delta E$  much smaller than the bin width  $\Delta E$ ,  $H$  is diagonal and each ele-

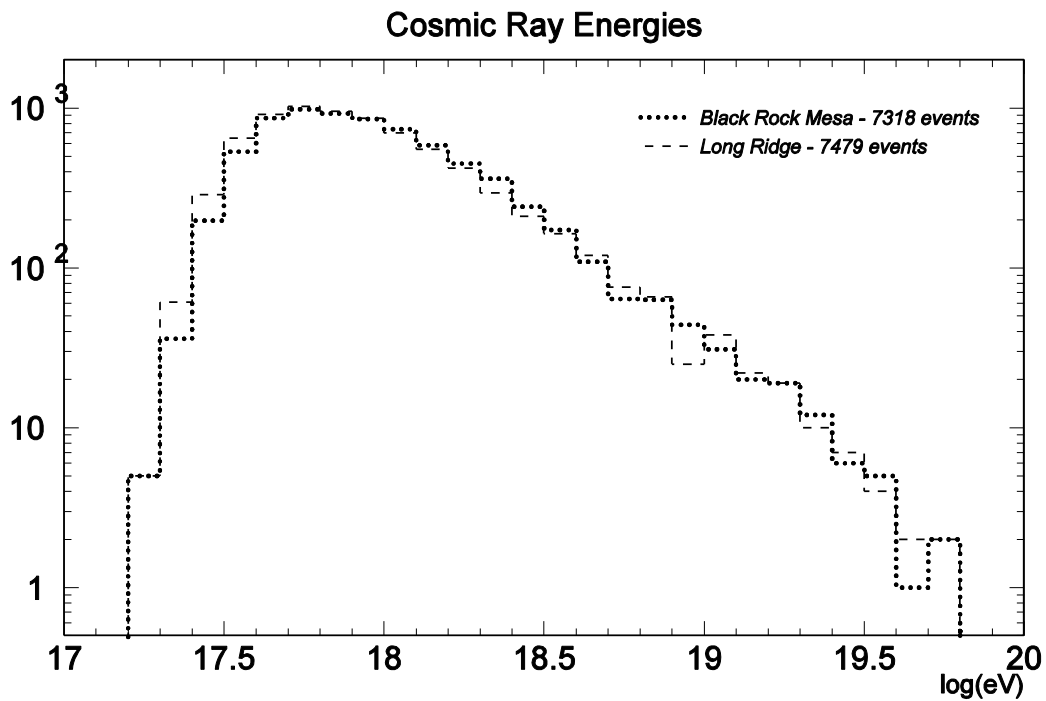


**Figure 5.3** Distribution of primary energies for events observed at Black Rock Mesa and Long Ridge.

ment is the number of reconstructed events  $\nu_i$  divided by thrown events  $n_j$ . However,  $\Delta E$  must be set small enough to resolve the features of the energy spectrum. One-tenth decade bins are used except for UHECR energies above 10 EeV, where the statistics are small. Some resolution mixing does occur, but this effect is mitigated by simulating an energy spectrum according to the flux measured by the HiRes experiment. The final expression for aperture is,

$$Ap(E_i) = \frac{\nu_i}{n_j} A\Omega \quad (5.3)$$

where the subscripts  $i$  and  $j$  are reminders that accepted events are binned according to reconstructed energy but thrown events are binned according to true energy.

The measured aperture in each energy bin is fit to the broken exponential function,

	Black Rock Mesa	Long Ridge
$p_1$	3.37±0.03	3.32±0.01
$p_2$	17.25±0.02	17.24±0.01
$p_3$	0.62±0.02	0.60±0.02
$p_4$	17.390±0.002	17.36±0.01
$p_5$	0.31±0.01	0.3±0.1
$\chi^2/\text{DOF}$	1.71	2.15

**Table 5.2** Fit parameters for aperture.

$$\log \text{Ap} = \begin{cases} p_1 \left(1 - \exp\left(-\frac{\log E - p_2}{p_3}\right)\right), & E \geq E_b \\ \gamma p_1 \left(1 - \exp\left(-\frac{\log E - p_4}{p_5}\right)\right), & E \leq E_b \end{cases} \quad (5.4)$$

where,

$$\gamma = \frac{1 - \exp\left(-\frac{\log E_b - p_2}{p_3}\right)}{1 - \exp\left(-\frac{\log E_b - p_4}{p_5}\right)} \quad (5.5)$$

and  $E_b = 10^{17.7}$  eV. Aperture was measured by generating a data set with TRUMP three times the size of the corresponding real data for each FD station. The ratio of the distributions of thrown and reconstructed events were taken and scaled by  $A\Omega$ . The results were fit to Equation (5.4) and are shown in Figure 5.4. The parameters from the fits are listed in Table 5.2. The break point was adjusted manually between 17.7 and 18.3 in steps of 0.1. The break point of 17.7 produced the smallest  $\chi^2$  in both BR and LR apertures.

## 5.2. Energy Spectrum

The number of events observed carrying energies between  $E$  and  $E + \Delta E$  is related to the differential cosmic ray flux through the detector's exposure,  $T\text{Ap}(E)$ , according to,

$$N(E, E + \Delta E) = \int_E^{E+\Delta E} T \text{Ap}(E') J(E') dE'. \quad (5.6)$$

The average flux in energy bin  $i$  is found by,

$$J(E_i) = \frac{N(E_i)}{\Delta E_i \text{Ap}(E_i) T} \quad (5.7)$$

where  $E_i$  is the energy at the center of the bin and  $\Delta E_i$  is the bin width. Essentially, Equation (5.7) says the UHECR flux can be calculated by taking the number of observed events in energy bin  $i$  and dividing by detector sensitivity. This is the same as dividing the entries in Figure 5.3 by those in Figure 5.4 and scaling according to net on-time, which is the total time the detectors were taking data minus the dead time which follows each trigger.

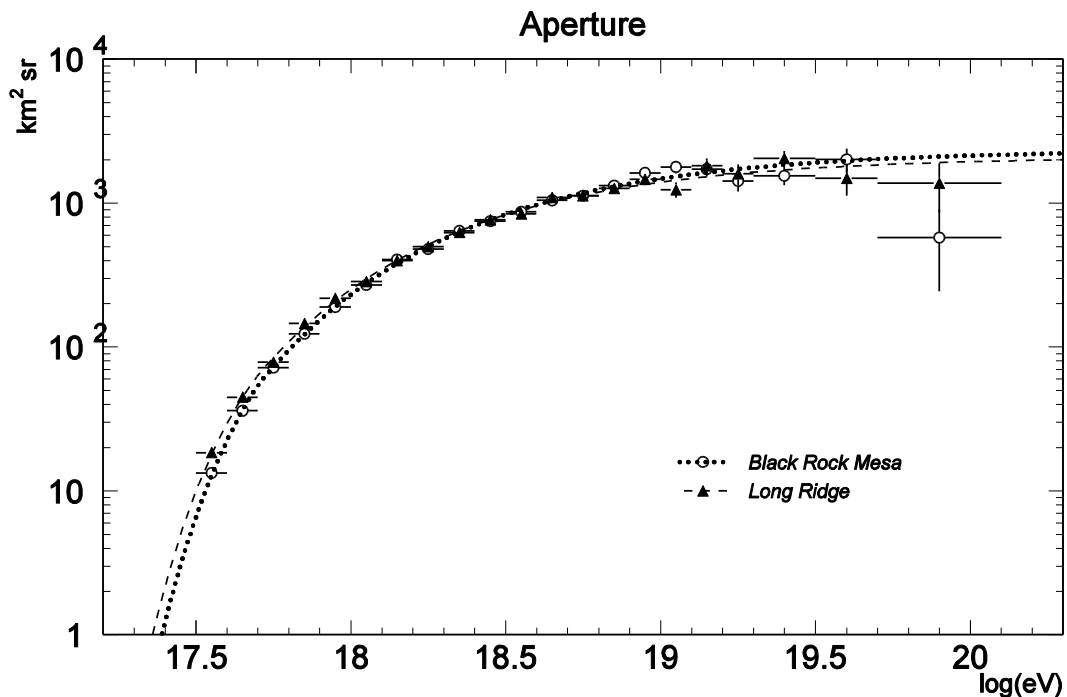


**Figure 5.4** FD aperture measured by Monte Carlo method.

Figure 5.5 shows the measurement of the UHECR flux. Since the energy spectrum drops off with energy according to an approximately  $E^{-3}$  power law, the spectrum is multiplied by  $E^3$  to emphasize its features. Just below  $10^{19}$  eV is the “ankle”, where the spectrum turns from a power law slightly steeper than  $E^{-3}$  to one that’s slightly shallower. The GZK suppression is visible above  $10^{19.5}$  eV, though the statistics are still small in that region.

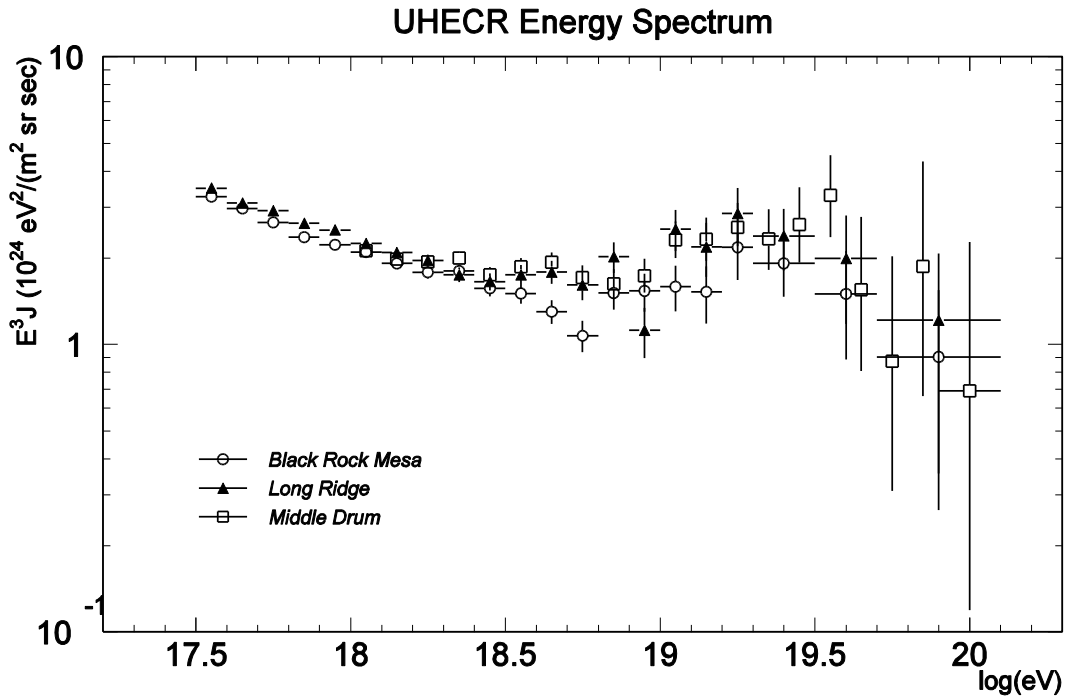


**Figure 5.5** Measurement of the UHECR flux from the three FD stations of Telescope Array.

### 5.3. BR & LR Combined Spectrum

One of the challenges in studying UHECRs comes from the rarity in the occurrence of the highest energy events. Since the FDs at Black Rock Mesa and Long Ridge are similar, their individual data sets can be combined to improve the statistics. However, care must be taken to account for the overlap in detector exposure and avoid double-counting events. This should be done in such a way that does not favor one station's results over the other.

Consider two cosmic ray detectors pointing in the same direction. For a given air shower, twice the light will be collected, possibly improving measurement of the shower profile and geometry. But there will be no improvement in numbers of events observed and hence the total aperture will not change. Now consider the same two detectors pointing in opposite directions. It is now unlikely that they will observe the same air showers and therefore the total aperture will double. The same principle may be applied when combining the monocular results from BR and

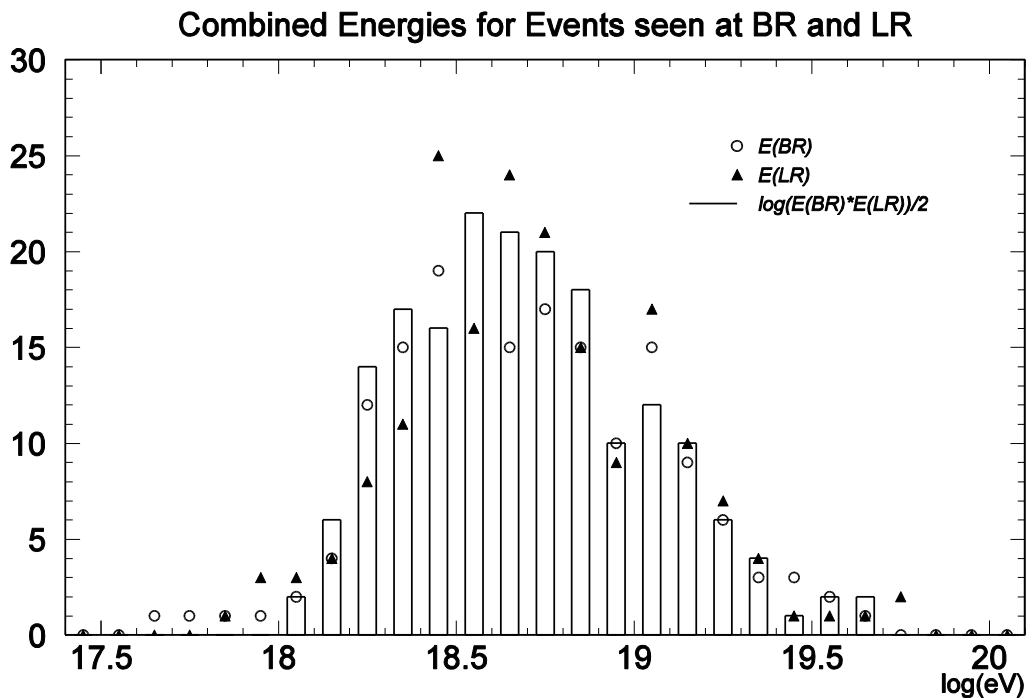


**Figure 5.6** Combined energy distribution for the 183 events in common between the BR and LR data sets. White circles and black triangles are the distributions of measured energies at Black Rock Mesa and Long Ridge, respectively. The bar histogram is the distribution of their geometric means.

LR. The stations are separated by about 30 km, so up to about  $10^{18}$  eV there is very little overlap in their apertures. However, at high energies the overlap is significant and must be accounted for if the sets are to be combined.

For a single detector, the flux of cosmic rays carrying energies between  $E$  and  $E + \Delta E$  is found by counting the number of observed cosmic ray events in that energy range and dividing by the detector's exposure, the product of aperture and on-time. The FD exposure may be thought of as sampling a volume in the space of UHECR geometries. Consider Equation (5.7), slightly re-written,

$$N(E_i) = T \text{ Ap}(E_i) J(E_i) \Delta E_i. \quad (5.8)$$

Flux must be independent of the detector, so any difference in the number of observed events must be a result of different detector exposures. The sets are combined by taking the union of the event distributions and corresponding exposures,

$$\begin{aligned} N_{BR}(E_i) + N_{LR}(E_i) - N_{BR \cap LR}(E_i) \\ = [T_{BR} A_{p_{BR}}(E_i) + T_{LR} A_{p_{LR}}(E_i) - T_{BR \cap LR} A_{p_{BR \cap LR}}(E_i)] \\ \cdot J(E_i) \Delta E_i \end{aligned} \quad (5.9)$$

The overlap in the BR and LR event distributions and exposures are denoted with the subscript  $BR \cap LR$ .

Of the 7318 events seen at BR and 7479 at LR, 183 were seen by both. So as not to give preference to the measurement from one detector over the other, the geometric mean of their energies is used,  $\log E_{BR \cap LR} = \frac{1}{2} \log(E_{BR} \cdot E_{LR})$ . Figure 5.6 shows the resulting energy distribution for the events seen in common between the BR and LR data sets. Figure 5.7 shows how the individual components combine into a single distribution. Note that Black Rock Mesa and Long Ridge each have one event in the 1019.6-1019.7 eV bin, but the combined distribution shows two events in that same bin (implying that each site observed the same two events in that range). It would seem that this was a contradiction, but this is just a consequence of binning the combined data set according to the geometric mean of each site's measurement of the energies of the events observed by both stations.

A tandem stereo (TS) Monte Carlo simulation was run to measure stereo aperture. When TRUMP is run in tandem mode, separate DST files are generated corresponding to each FD. These files were passed through the standard monocular reconstruction programs, then time-matched using the same program used on real data. But there are some differences in the calculation of TS exposure compared to single-detector mode. In both cases, event times are simulated along with each event and the atmospheric conditions, calibrations and pedestals corresponding to that time are used when simulating the event. By simulating over all the times in the data set, some time-dependent effects like drifting of the gain and seasonal variations in the atmosphere

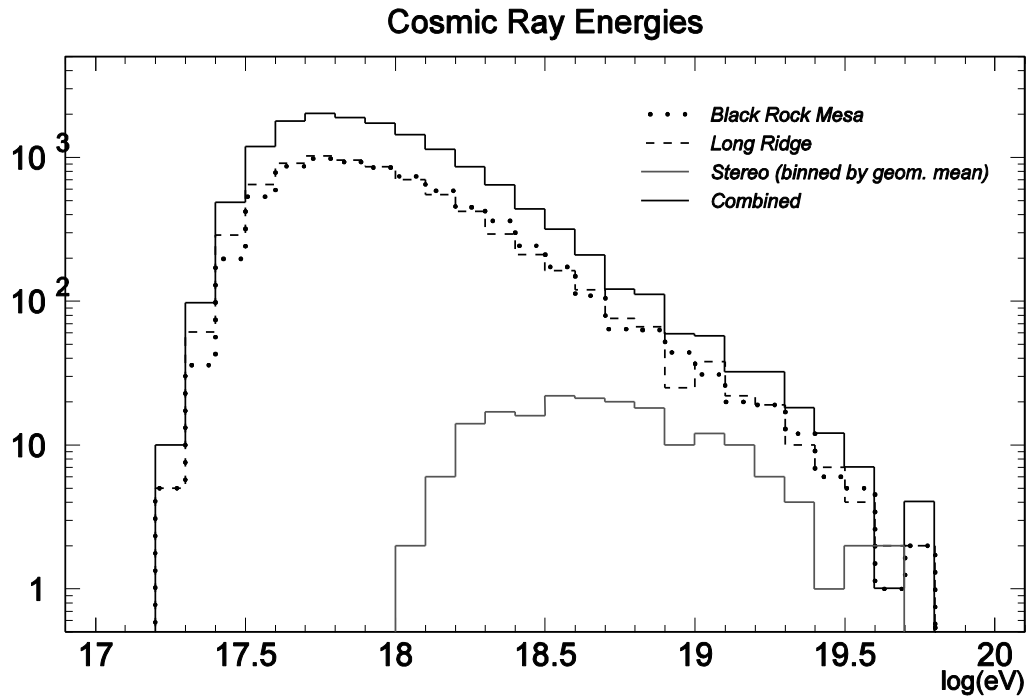


**Figure 5.7** Individual components of the combined data event distribution. The histograms are necessarily un-normalized because the differences in on-times and aperture are accounted for when combining exposures.

are averaged out. In single-detector mode, the pedestals files are used to find the times the detector was actively taking data and event times are only selected in that range. In this case, the meaning of a “thrown” cosmic ray event is one which was given a random position and orientation within  $A\Omega$  during the time when the detector was actually taking data.

In TS mode, however, one detector’s on-time cannot be favored over the other. The periods when the detectors were actually taking data vary quite a bit, a property which is reflected in the pedestals files used for the simulation. To maintain a consistent treatment between BR and LR, event times are allowed to occur any time within the earliest start time and latest stop time between the two detectors on a given night instead of selecting times which only occur while one detector was taking data. If the event time falls between runs, then detector ray tracing and electronics simulation is skipped, but it is still counted as thrown. In this case, the meaning of a thrown event is one given a random position and orientation in  $A\Omega$ , but occurs at any time within

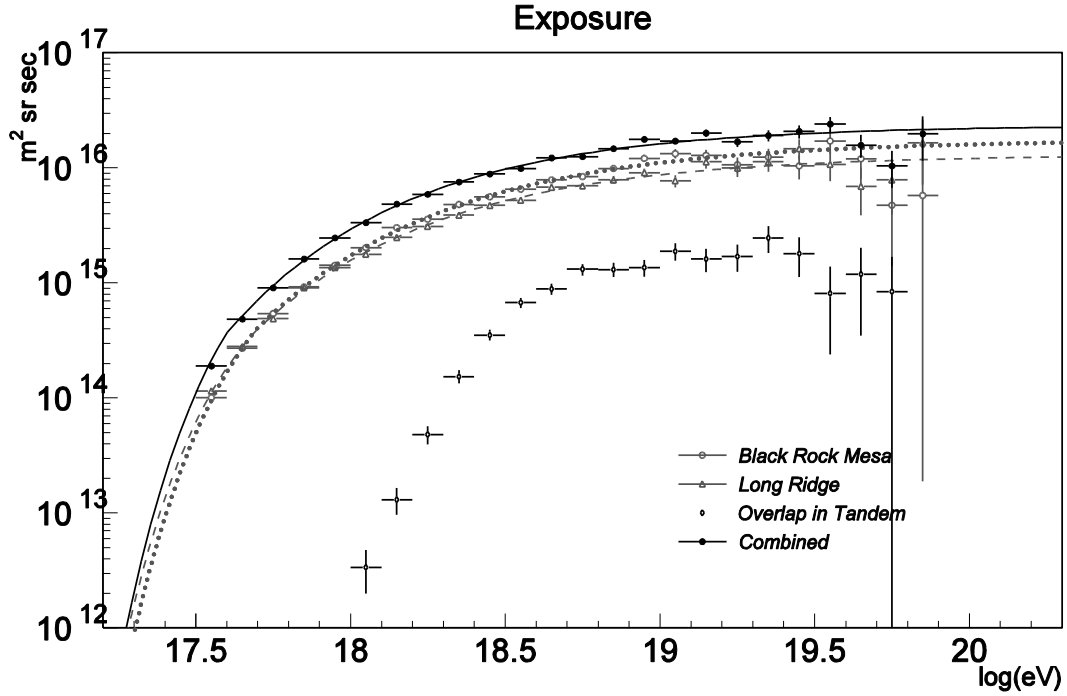


**Figure 5.8** The combined exposure is the union of the LR and BR exposures. It is nearly twice the size of either BR or LR, since the overlap is so small.

the start and end of observation between BR and LR. For this reason, mono and TS aperture cannot be directly compared, but their total exposure can. Detector exposures are combined using the expression,

$$X(E) = \bar{T}A\Omega[\xi_{BR}(E) + \xi_{LR}(E) - \xi_{BR\cap LR}(E)], \quad \xi = \frac{T v_i}{\bar{T} n_j} (1 - f) \quad (5.10)$$

where the ratio  $v_i/n_j$  is acceptance,  $T$  is the detector's gross on-time,  $f$  is the dead time fraction and  $\bar{T}$  is a characteristic exposure time, used to normalize the acceptances from each configuration (BR mono, LR mono and tandem stereo). The dead time fraction for TS data comes from the product of the individual detectors' dead times,  $f_{BR\cap LR} = 1 - (1 - f_{BR})(1 - f_{LR})$ . The combined exposure, plotted with its individual components, is shown in Figure 5.8. Finally, the combined spectrum is the combined number of observed events divided by the combined exposure.

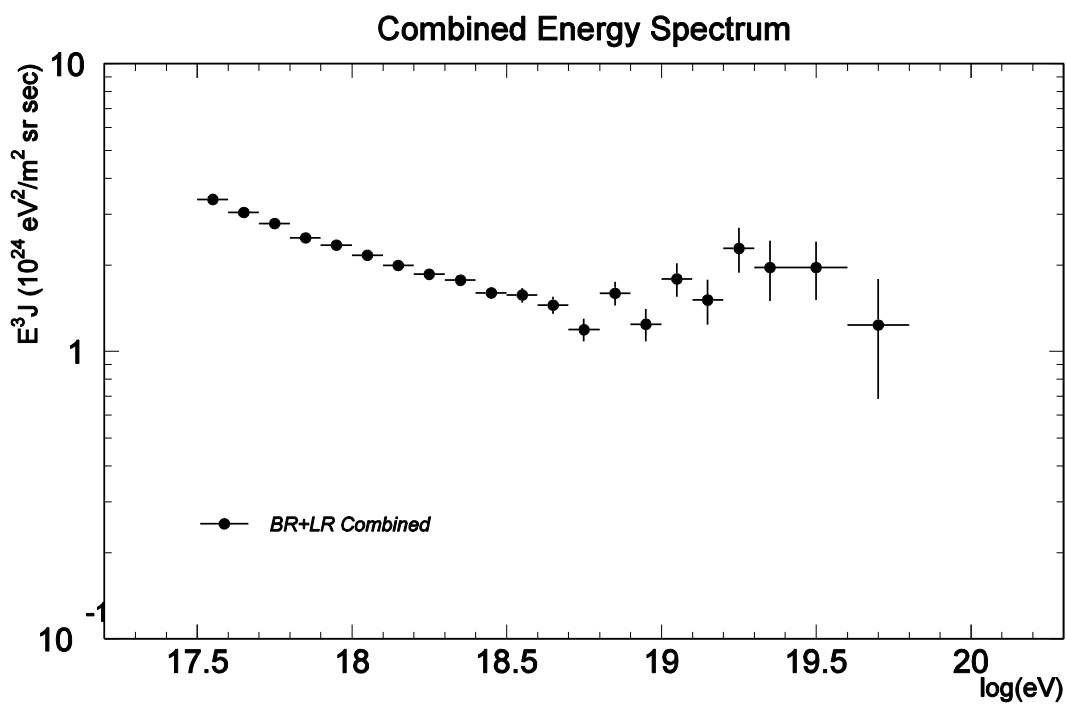


**Figure 5.9** Energy spectrum calculated by combining the statistics of the Black Rock Mesa and Long Ridge data sets.

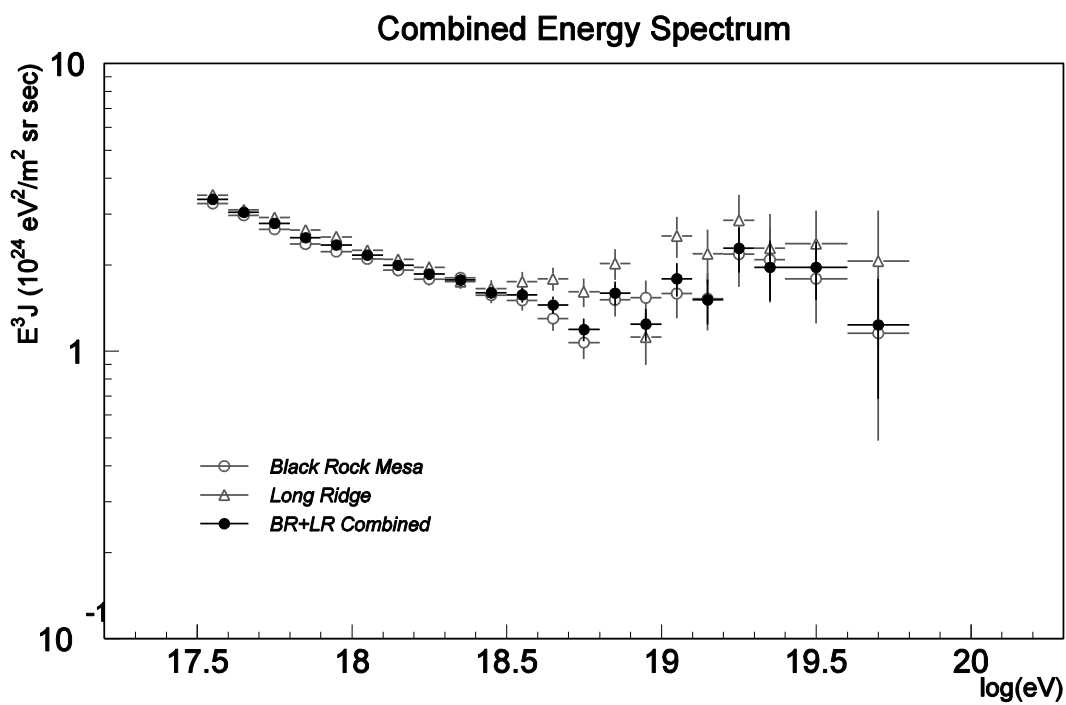


**Figure 5.10** Combined energy spectrum compared to its constituent data sets.

Figure 5.9 shows the combined spectrum compared to the individual monocular measurements by BR and LR. In each case, a least-squares fit is performed on the aperture, so the data points in the combined spectrum do not necessarily need to fall between the corresponding points from the monocular spectra.

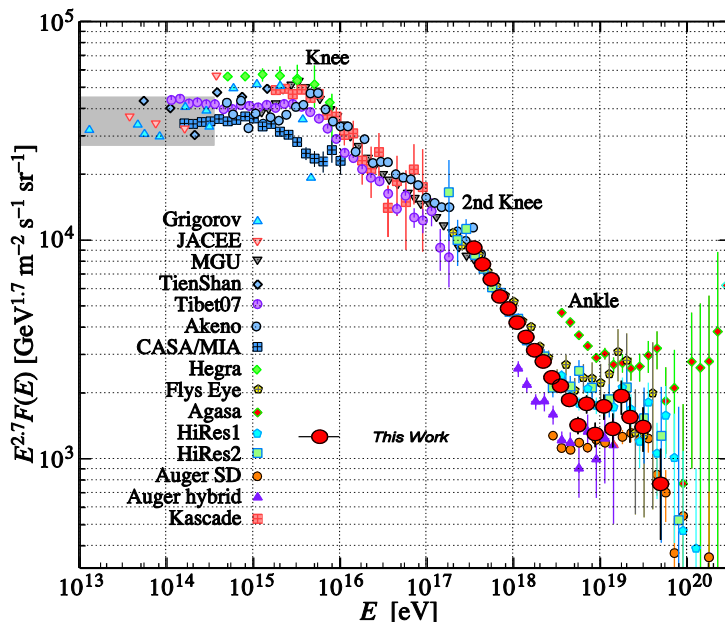


**Figure 5.11** Measurement presented in this work compared to other independent experiments.

## 5.4. Evaluation of Detector Resolution

Before complete estimates of the systematic errors in energy measurements can be made, one must understand the limits of each fluorescence detector's resolution. In other words, given a set of ideal conditions, how well the energy of a given air shower event can be calculated. Energy resolution is found entirely by analyzing Monte Carlo data. This analysis offers some guarantees that don't exist when processing real data. First, the detector geometry used throughout the analysis is identical to that used by TRUMP. So errors in mirror reflectance, radius of curvature, detector pointing directions, won't be factored in the energy resolution. The pressure, temperature and density profiles of the atmosphere are also guaranteed to match between simulation and

the processing of simulated data. Even though real-time Radiosonde sounding data is used, the corresponding time-dependent PTD data will be used throughout the analysis. Finally, PMT gains are also guaranteed to match in simulation and the analysis. The calibration database uses estimates of true PMT gains by drawing on data from a larger database. This introduces some uncertainty in the absolute photonic scale when analyzing real data, but not when analyzing simulated data.

With most of the major contributions of systematic error eliminated, the analysis of Monte Carlo data can provide information about how well the shower geometry and profile parameters can be estimated using particular software, data quality cuts and an idealized version of the fluorescence detectors. Here, the resolution of a parameter is defined as the difference between its measured and known value. Parameters such as  $N_{\max}$  and energy span several orders of magnitude, so the difference between their natural logarithms is taken. The distributions of these are non-Gaussian and slightly asymmetric, so the full-width at half-maximum is used to characterize their width. Figure 5.12 shows the  $R_p$  and  $\psi$  resolution for BR and LR. Figure 5.13 shows the resolution in  $X_{\max}$  and  $\ln N_{\max}$ , which include errors introduced by uncertainty in  $R_p$  and  $\psi$ . Finally, Figure 5.14 shows the energy resolution, including a Gaussian fit from  $-0.2$  to  $0.2$ . These plots show the energy resolution for Black Rock and Long Ridge to be just below 10%. Due to poor data-Monte Carlo agreement for air showers with measured energies below  $10^{17.5}$  eV, those events have been excluded from this analysis.

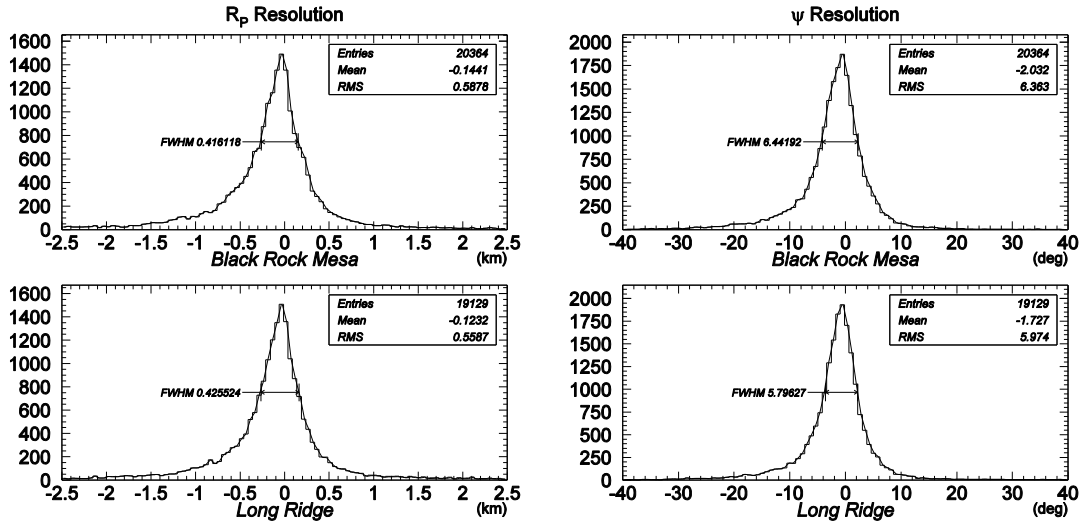


Figure 5.12  $R_p$  and  $\psi$  resolution plots for BR and LR FD stations. Only events with energies above  $10^{17.5}$  eV were considered here.

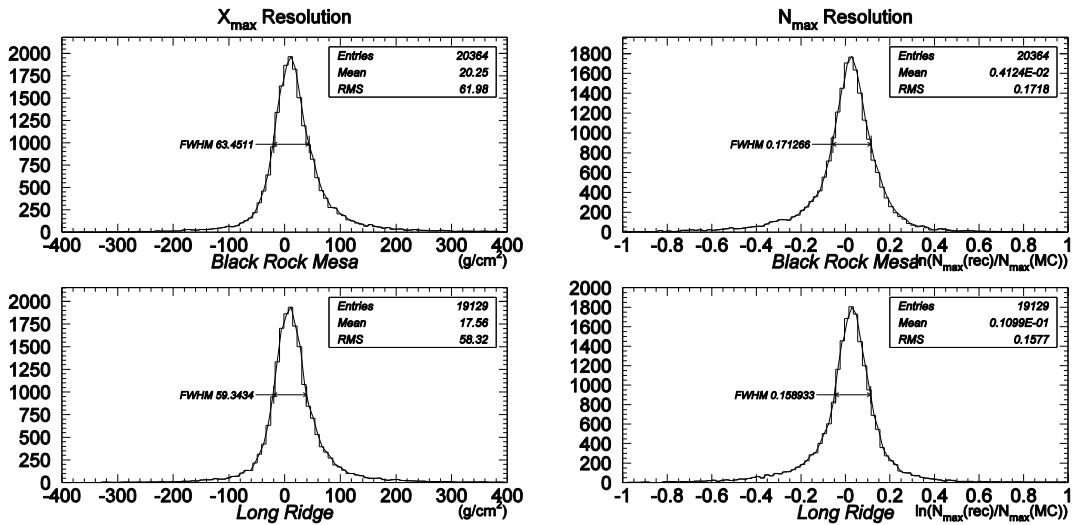
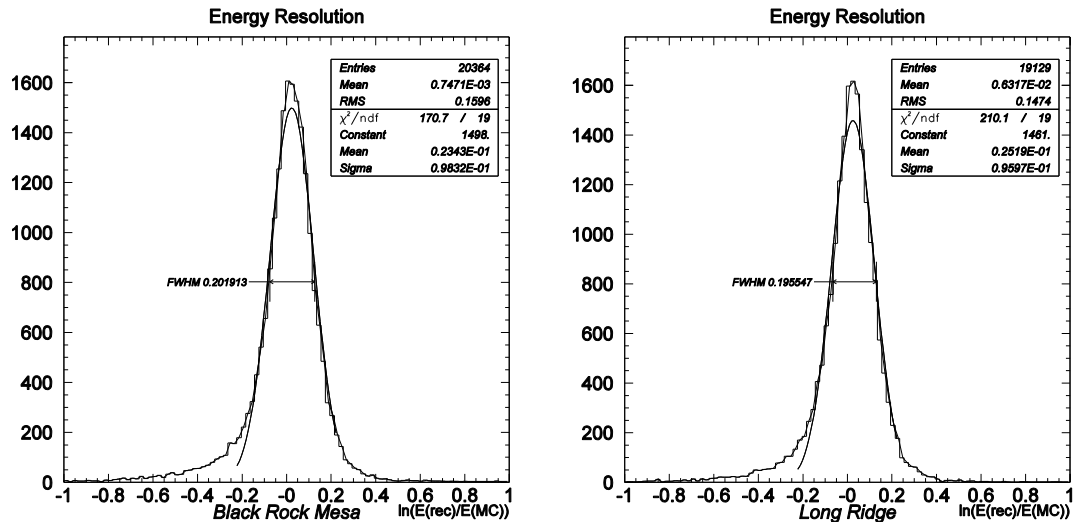


Figure 5.13  $X_{\max}$  and  $N_{\max}$  resolution plots for BR and LR FD stations. Only events with energies above  $10^{17.5}$  eV were considered here. Note that these values are based on reconstructed geometries, so errors in  $R_p$  and  $\psi$  are intrinsically included here.



**Figure 5.14** Energy resolution plots for BR and LR FD stations. Only events with energies above  $10^{17.5}$  eV were considered here.

## 5.5. Evaluation of Systematic Errors

The light produced in an extensive air shower must be transmitted through the atmosphere, the physical components of the FD telescope and converted to a set of electrical signals before winding up as bits in a raw data stream. For each trigger, the goal is to find the set of parameters,  $R_p$ ,  $\psi$ ,  $\hat{n}$ ,  $N_{\max}$  and  $X_{\max}$ , which uniquely describe the underlying air shower geometry and light profile. The first three describe the shower geometry and are found by combining signal timing information and the image on the detector's focal plane. The last two are found by repeatedly simulating air showers with the best-fit geometry while varying  $N_{\max}$  and  $X_{\max}$  until the best agreement between the real and simulated waveforms are found. The measurement of calorimetric energy deposited follows from these two parameters and the *missing energy* correction is found by analysis of air showers simulated with CORSIKA. This is essentially a summary of UHECR fluorescence detection and virtually everything mentioned here contributes to the total systematic uncertainty.

Optics	Mirror Reflectance	4%
	Paraglas Transmittance	2%
	BG3 Transmittance	2%
	subtotal	5%
PMT, gain, monitor	2D Uniformity	3%
	CRAYS	7%
	HV Stability	2%
	Gain correction in camera by XF	2%
	Hourly monitoring	3%
	Camera-camera correction from XF	5%
	subtotal	10%
Total uncertainty from detector calibration		11%

**Table 5.3** Contribution to total systematic uncertainty in energy measurements due to detector calibration [39].

Fundamentally, the systematic error of an experiment arises from limitations in the understanding of the physical phenomena being studied and the phenomena intrinsic to the experimental apparatus. With this in mind, the contributing factors are divided into three groups: uncertainty in the models related to the physics of cosmic rays and the extensive air shower (e.g. the missing energy correction), those related to the physical phenomena intrinsic to the “laboratory”, referring to the open atmosphere in this case (e.g. Rayleigh and aerosol scattering), and those related to the experimental apparatus (e.g. photomultiplier gains). In the case of the missing energy correction, for example, no experimental data exists for the average penetration depth of a  $10^{21}$  eV proton in air (or through any matter). Instead, CORSIKA simulations are used which rely on the standard model and extrapolation from experimental results involving particle interactions many orders of magnitude lower in energy. In fact, when compiling CORSIKA, users are required to select a high-energy interaction model, either QGSJet or SIBYLL. The difference between using one model or the other adds 5% to the total systematic uncertainty for this experiment. To be clear, the systematic errors described here indicate a 68% confidence level that the difference between a measurement and its true value is less than the quoted uncertainty.

Absolute photomultiplier gains were measured in a laboratory using CRAYS, which is essentially a separate experiment with its own sources of systematic error. The major compo-

nents of the uncertainty in absolute gain come from the measurement of the position of the components in the chamber and accounting for multiple scattering. The final report on CRAYS quoted a total uncertainty of 7%, but this result only applies to the 52 PMTs that were calibrated with this system. The non-CRAYS tubes are gain-matched by adjusting their individual HV until all of the tubes in each camera produce the same size response to the built-in xenon flashers. This response is monitored on an hourly basis during runs, but each PMT has unique temperature dependence and the HV supply is restricted to one volt increments. For the non-CRAYS tubes, the systematic error will include the CRAYS result, the tube-to-tube variance in temperature dependence, the variance in the signal from the xenon flasher and an additional 2% for the resolution and stability of the HV supply. These factors together add 3% uncertainty to the gain and, since the FDs use mostly non-CRAYS tubes, the systematic error in PMT gain is 10%.

The transmittance as a function of wavelength of the BG3 filter and Paraglas dust covers were measured by the manufacturers and confirmed by the calibration group using their own spectrometer. The error due to glass transmittance comes from the piece-to-piece variation, which inherently combines the fluctuations in the glass thickness, purity and the performance of the spectrometer. Glass transmittance directly affects the photonic scale, so each contributes 2% to the systematic error. Mirror reflectivity is measured periodically, before and after washing. The reflectivity drops rapidly in the days immediately following washing due to dust accumulation, but levels off roughly according to an exponential decay function. The reflectometer that is used does not actually probe down to the wavelengths the detector is designed to observe. Instead, the results from the reflectivity measurements are scaled to the curves provided by the manufacturer and extrapolated to the relevant wavelength band. Mirror reflectivity is also directly proportional to photonic scale and adds 4% uncertainty. The calibration sub-group released their own detailed analysis of the systematic errors associated with the experimental apparatus. The results are shown in Table 5.3.

Uncertainty from experimental apparatus	
Detector Optics [39] & Telescope Geometry	10%
Electronics [39]	10%
Detector On-time	1%
Uncertainty from “laboratory” environment	
Attenuation by Aerosols	10%
Uncertainty from physics models	
Fluorescence Yield [8]	10%
Mean $dE/dX$ [34]	1%
Missing Energy Correction	5%
Systematic Uncertainty to Energy Measurement	21%
Systematic Uncertainty to Flux Measurement	35%

**Table 5.4** Contributions to the systematic uncertainty.

Molecular (Rayleigh) scattering is a well-understood process and does not contribute much to the uncertainty. The Mie model is used for aerosol scattering which assumes the aerosols are dielectric spheres. In reality, the aerosols vary in size and shape tremendously and form an inhomogeneous mixture with the air. LIDAR systems and the CLF are used to measure aerosols and show a large variation from night to night. The systematic error due to aerosol attenuation was calculated empirically by performing the standard analysis using different values of mean attenuation lengths. The study revealed that, on average, a 10% shift to attenuation length led to a 1% shift in energy scale. The measured attenuation fluctuated by about 100% over a six month time period ( $29.4 \pm 30$  km). Therefore, the error in energy estimates due to uncertainty in aerosol scattering will be about 10%. Other properties of the atmosphere, namely pressure, density and temperature, are derived from Radiosonde data taken 150 miles away at Salt Lake City airport. Comparison to profiles from Radiosonde data taken at Elko, Nevada and Flagstaff, Arizona show little variation on average from station to station, but on a given night there can be a large discrepancy. These properties affect basic shower development as well as dictating light

transmission. Uncertainty in the thermodynamic properties of the atmosphere therefore contributes another 10% to the total systematic error.

The fluorescence yield models used in TRUMP are based on the results from the Kakimoto and FLASH electron beam experiments. Because fluorescence yield is directly proportional to calorimetric energy and each experiment quotes a 10% total uncertainty, this must be brought directly into the systematic uncertainty total here. Čerenkov yield is proportional to the number of charged particles present in the shower at any given moment, a number which is based on fits to CORSIKA showers. Just as with the missing energy correction, CORSIKA relies on high-energy interaction models which combine Standard Model theory with particle collider experiment data. There is no experimental data which can tell us the real number of charged particles that would result from the collision of a 1-100 EeV proton and a nitrogen atom, so uncertainty in Čerenkov yield contributes 5%, the same as the missing energy correction.

Table 5.4 is an itemized list of the systematic uncertainty for the measurement of the primary energy of a UHECR. The total uncertainty is the sum of the individual errors added in quadrature.

## 5.6. Interpretation of results

This year will mark the 100<sup>th</sup> anniversary of Victor Hess' discovery of cosmic radiation, yet we still don't know the origin of ultra-high energy cosmic rays. The High-Resolution fly's eye experiment, one of Telescope Array's predecessors, operated long enough to resolve the GZK suppression, thus confirming the energy scale of measurements using the fluorescence detection technique [8]. But the highest energy cosmic rays occur very rarely, so larger, more sensitive experiments are required in order to collect a large enough data set for comparison with theoretical models. The other major obstacle in UHECR research relates to the large systematic errors that enter in by applying interaction models developed from particle collider data to measure-

ments taken in an uncontrolled environment. When compounded with an  $E^{-2.7}$  power law, a 21% uncertainty in measurements of cosmic ray energies turns into a 35% uncertainty to the measurement of flux! So while it might seem that the measurements by Auger hybrid and AGASA shown in Figure 5.11 are significantly different than the trend, they are within the experiments' systematic errors.

The good news is these are not insurmountable problems. At the Large Hadron Collider, protons are collided with protons with center-of-mass energies near 10 TeV. This is comparable to the center-of-mass energy in the collision between a  $10^{18}$  eV proton and a molecule of atmosphere. Therefore, data collected by the LHC may be used to refine the interaction models UHECR experiments use to estimate cosmic ray energies. Systematic errors due to atmospheric scattering may also be reduced by analysis of LIDAR and other laser data collected by the fluorescence detectors. There is also work being done to improve measurements of the detector optics, such as mirror reflectivity and mirror alignment.

This thesis presents an analysis of the first three years of data collected by the fluorescence detectors at Black Rock Mesa and Long Ridge. It was demonstrated here that the analysis and corresponding measurement of UHECR flux is consistent with other components within Telescope Array. Furthermore it is consistent with measurements produced independently by other cosmic ray experiments. In the coming years, Telescope Array will add detectors and continue to collect data. As new results are published and presented, the feedback loop between experiment and theory will continue to be driven.

## Appendix A. Geometry Correction

The PMTs are gain-matched by adjusting their individual HV supplies until they all produce the same ADC response to a xenon flasher (XF). Due to their physical location with respect to the XF, tubes farther from the mirror-camera axis will receive less light and their HV will be slightly over-adjusted. A correction factor must be applied to the gains to account for this difference.

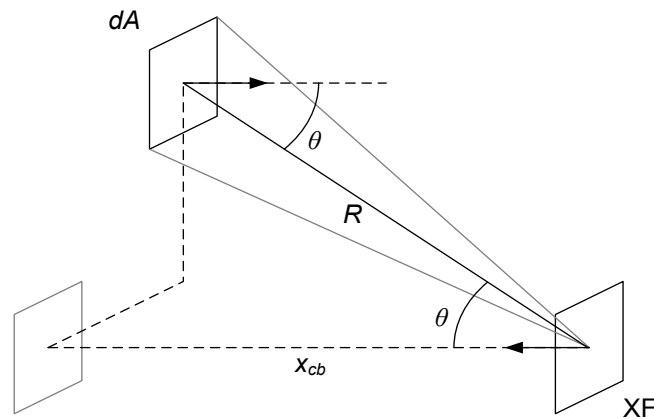


**Figure A.1** Geometry Correction.

Consider the scenario illustrated by Figure A.1. Light is produced from a source at XF and received in the region labeled  $dA$ . The differential photon flux from the XF is,

$$\frac{dN}{d\Omega} = \frac{N_0}{\pi} \cos \theta \quad (\text{A.1})$$

If  $dA$  is small compared to its distance from the source, then  $R^2 d\Omega \approx dA \cos \theta$ . If  $dA$  is constrained to the plane a distance  $x_{cb}$  from the flasher along the mirror-camera axis, then  $R$  will depend on  $\theta$  according to  $R = x_{cb} / \cos \theta$  and the differential flux in terms of  $dA$  becomes,

$$\frac{dN}{dA} = \frac{N_0}{\pi x_{cb}^2} \cos^4 \theta. \quad (\text{A.2})$$

Therefore the observed flux through  $dA$  from Lambertian source XF is proportional to  $\cos^4 \theta$ .

## Appendix B. FADC Correlation

Consider a waveform in the presence of Poisson-distributed background noise  $v_i$  and constant pedestal  $p$ . Let  $E[x]$  be the expectation value of  $x$ , according to Poisson statistics,

$$E[v_i] = E[(v_i - E[v_i])^2] = \mu \quad (\text{B.1})$$

where  $\mu$  is the background level which is assumed constant or slowly varying in time. The signal is smeared by the data acquisition circuit so the value  $f_i$  of the FADC is influenced by all of the photo-electrons that arrive before and during time slice  $i$ . That is,

$$f_i = g \sum_{k=0}^{\infty} c_k v_{i-k} + p, \quad \sum_{k=0}^{\infty} c_k = 1. \quad (\text{B.2})$$

Furthermore, the background is uncorrelated, so,

$$E[v_i v_j] = \mu^2 + \mu \delta_{i,j}, \quad \delta_{i,j} = \begin{cases} 1, & i = j \\ 0, & i \neq j \end{cases} \quad (\text{B.3})$$

In the absence of signal, the expectation value for each time slice is then,

$$E[f_i] = E \left[ g \sum_{k=0}^{\infty} c_k v_{i-k} + p \right] = g\mu + p. \quad (\text{B.4})$$

The covariance between time slices is,

$$\begin{aligned} E[f_i f_j] &= E \left[ \left( g \sum_{m=0}^{\infty} c_m v_{i-m} + p \right) \left( g \sum_{n=0}^{\infty} c_n v_{j-n} + p \right) \right] \\ &= g^2 \sum_{m=0}^{\infty} \sum_{n=0}^{\infty} c_m c_n (\mu^2 + \mu \delta_{i-m, j-n}) + p^2 + 2pg\mu \\ &= g^2 \mu \sum_{k=0}^{\infty} c_k c_{k-(i-j)} + (g\mu + p)^2. \end{aligned} \quad (\text{B.5})$$

For  $i = j$ ,

$$E[f_i^2] - E[f_i]^2 = g^2 \mu \sum_{k=0}^{\infty} c_k^2. \quad (\text{B.6})$$

Therefore, time slice correlation does not affect the observed mean FADC but it does reduce the variance, since the sum over  $c_k^2$  is necessarily less than one.

Let  $s_i$  be the sum of a sequence of FADC such that,

$$s_i = \sum_{j=0}^{w-1} f_{i-j}. \quad (\text{B.7})$$

The expectation value of  $s_i$  is then given by,

$$E[s_i] = E\left[\sum_{j=0}^{w-1} f_{i-j}\right] = \sum_{j=0}^{w-1} E[f_{i-j}] = wE[f_i] = w(g\mu + p) \quad (\text{B.8})$$

since  $E[f_i] = E[f_{i-1}]$ . The variance in the summed FADC is,

$$\begin{aligned} E[(s_i - E[s_i])^2] &= \sum_{j=0}^{w-1} \sum_{k=0}^{w-1} E[f_{i-j}f_{i-k}] - E[s_i]^2 \\ &= \sum_{j=0}^{w-1} \sum_{k=0}^{w-1} \left\{ g^2 \mu \sum_{m=0}^{\infty} c_m c_{m-(k-j)} + (g\mu + p)^2 \right\} - E[s_i]^2 \\ &= g^2 \mu \sum_{j=0}^{w-1} \sum_{k=0}^{w-1} \sum_{m=0}^{\infty} c_m c_{m-(k-j)} = \gamma w g^2 \mu. \end{aligned} \quad (\text{B.9})$$

No matter how large  $w$  is, there will always be some small reduction in the measured variance as a result of time slice correlation. The coefficients  $c_k$  were found by waveform simulation. The mean and variance used by the SDF threshold generator are based on 16-bin sums of FADC, which puts  $\gamma = 0.956$ .

## Appendix C. Recursion Relation for Waveform Simulation

Consider an  $n$ -pole low pass filter with RC time constant  $\tau$  and transfer function,

$$f_n(t; \tau) = \frac{t^{n-1} e^{-\frac{t}{\tau}}}{(n-1)! \tau^n}. \quad (\text{C.1})$$

This function may be propagated in equal steps in time with period  $T$  by repeatedly applying a set of constant factors to the sum of the lower order filters with the same time constant. After  $N$  periods, Equation (C.1) becomes,

$$f_n(t + NT; \tau) = \frac{(t + NT)^{n-1} e^{-\frac{t+NT}{\tau}}}{(n-1)! \tau^n}. \quad (\text{C.2})$$

The coefficient in the numerator can be expanded in binomial series giving,

$$\begin{aligned} f_n(t + NT; \tau) &= \sum_{k=0}^{n-1} \frac{(n-1)!}{k! (n-1-k)!} \frac{(NT)^k t^{n-1-k}}{(n-1)! \tau^n} e^{-\frac{t+NT}{\tau}} \\ &= \sum_{k=0}^{n-1} \frac{(NT)^k e^{-\frac{NT}{\tau}}}{k! \tau^k} \frac{t^{n-1-k} e^{-\frac{t}{\tau}}}{(n-1-k)! \tau^{n-k}} = \sum_{k=0}^{n-1} c_k f_{n-k}(t; \tau). \end{aligned} \quad (\text{C.3})$$

If the transfer function represents two filters with different RC time constants  $\alpha$  and  $\tau$ , then  $F$  will be the convolution of the individual filters' transfer functions, found by Laplace transform,

$$F(t) = f_m(t; \alpha) * f_n(t; \tau) \quad (\text{C.4})$$

$$H(s) = \mathcal{L}[F(t)] = \frac{1}{(1 + \alpha s)^m} \frac{1}{(1 + \tau s)^n} \quad (\text{C.5})$$

$$F(t) = \mathcal{L}^{-1}[H(s)] = \sum_{i=0}^{m-1} a_i t^i e^{-\frac{t}{\alpha}} + \sum_{j=0}^{n-1} b_j t^j e^{-\frac{t}{\tau}}. \quad (\text{C.6})$$

The coefficients  $a_i$  and  $b_j$  will contain a mixture of  $\alpha$  and  $\tau$ . In TRUMP, only the contribution from the photomultiplier transit time spread (TTS) and the shaper circuit were considered when computing the net impulse response function for light incident on the PMT. The shaper circuit is

a second-order Butterworth filter with RC time constant  $\tau = 50$  ns. The TTS is approximately a 5 ns wide Gaussian, a function in which the treatment described here does not apply. Instead, the Gaussian shape is approximated by a 5-pole filter with time constant  $\alpha = 5$  ns and the net impulse response function used by TRUMP is,

$$F(t) = \left(\frac{\alpha}{\tau - \alpha}\right)^2 \sum_{i=1}^5 (6-i) \left(\frac{\tau}{\tau - \alpha}\right)^{5-i} f_i(t; \alpha) + \left(\frac{\tau}{\tau - \alpha}\right)^5 \sum_{i=1}^2 \left(\frac{5\alpha}{\tau - \alpha}\right)^{2-i} f_i(t; \tau). \quad (\text{C.7})$$

The total impulse response to  $N_{\text{pe}}$  arriving between samples is just the sum of their individual impulse response functions. It can be shown that this total may be propagated in time in the same way. Let  $t_i$  be the length of time between the arrival of photo-electron  $i$  and the next sample. Assuming linearity of PMT gain, the measured signal at the first sample will be the sum,

$$V_0 = \sum_{i=1}^{N_{\text{pe}}} F(t_i) = \sum_{i=1}^{N_{\text{pe}}} \left[ \sum_{k=1}^5 a_k f_k(t_i; \alpha) + \sum_{k=1}^2 b_k f_k(t_i; \tau) \right] = \sum_{k=1}^5 a_k \sum_{i=1}^{N_{\text{pe}}} f_k(t_i; \alpha) + \sum_{k=1}^2 b_k \sum_{i=1}^{N_{\text{pe}}} f_k(t_i; \tau). \quad (\text{C.8})$$

After one sample period, this becomes,

$$V_1 = \sum_{k=1}^5 a_k \sum_{i=1}^{N_{\text{pe}}} f_k(t_i + T; \alpha) + \sum_{k=1}^2 b_k \sum_{i=1}^{N_{\text{pe}}} f_k(t_i + T; \tau) = \sum_{k=1}^5 a_k \sum_{i=1}^{N_{\text{pe}}} \sum_{l=1}^5 c_l f_{k-l}(t_i; \alpha) + \sum_{k=1}^2 b_k \sum_{i=1}^{N_{\text{pe}}} \sum_{l=1}^2 d_l f_{k-l}(t_i; \tau) \quad (\text{C.9})$$

with,

$$c_l = \frac{T^l}{l! \alpha^l} e^{-\frac{T}{\alpha}}, \quad d_l = \frac{T^l}{l! \tau^l} e^{-\frac{T}{\tau}}. \quad (\text{C.10})$$

Let  $R$  and  $S$  be defined as the sums,

$$R^{(n)} \equiv \sum_{i=1}^{N_{\text{pe}}} f_n(t_i; \alpha), \quad S^{(n)} \equiv \sum_{i=1}^{N_{\text{pe}}} f_n(t_i; \tau). \quad (\text{C.11})$$

After one sample period,  $R$  and  $S$  become,

$$R_1^{(n)} = \sum_{i=1}^{N_{\text{pe}}} \sum_{k=1}^n c_k f_{n-k}(t_i; \alpha) = \sum_{k=1}^n c_k R^{(n-k)} \quad (\text{C.12})$$

and,

$$S_1^{(n)} = \sum_{i=1}^{N_{\text{pe}}} \sum_{k=1}^n d_k f_{n-k}(t_i; \tau) = \sum_{k=1}^n d_k S^{(n-k)}. \quad (\text{C.13})$$

Rewriting Equations (C.8) and (C.9) in terms of  $R$  and  $S$  yield,

$$V_0 = \sum_{k=1}^5 a_k R^{(k)} + \sum_{k=1}^2 b_k S^{(k)} \quad (\text{C.14})$$

and,

$$\begin{aligned} V_1 &= \sum_{k=1}^5 \sum_{l=1}^5 a_k c_l R^{(k-l)} + \sum_{k=1}^2 \sum_{l=1}^2 b_k d_l S^{(k-l)} \\ &= \sum_{k=1}^5 a_k R_1^{(k)} + \sum_{k=1}^2 b_k S_1^{(k)}. \end{aligned} \quad (\text{C.15})$$

The coefficients  $a_k$  and  $b_k$  are therefore independent of the number of individual photo-electrons and their arrival times. Additionally, PE that arrive in subsequent sampling periods simply add to the total signal which can then be propagated using the same factors.

TRUMP simulates the impulse response by treating the electronics transfer function as the convolution of a two- and 5-pole filter. Equations (C.12) and (C.13) set up a recursion relation which can be used to update the observed signal without the need for an extra loop over time slices. In fact the “state” of the signal may be expressed by seven constants, five from  $R^{(n)}$  and two from  $S^{(n)}$ . Beyond this, no memory of the underlying signal is needed to produce a continu-

ous waveform. Hence, using this recursion relation method improves the electronics simulation in two major ways. First, only the PE arrival times within a sample period are needed for each iteration over clock cycles, compared to the “brute-force” method where the signal would be added to all clock cycles where it was significant.

The second, more important, improvement stems from the nature of the electronics simulation. By design, it behaves like the real electronics in that waveforms are scanned one frame at a time. In this case, it is important that the subsequent time slices in the updated waveform reflect the history of PE arrival times when moving to the next frame. Otherwise, breaks would appear in the waveform, possibly affecting calculation of significance and potentially not triggering a PMT when it would under regular conditions. Without using this recursion relation, there are two alternative methods one could use. First, simply repeat the waveform simulation with all PE times shifted by  $12.8 \mu\text{s}$ . This would yield accurate results but would be very time consuming. Second, save the waveform signal history in an array. This would require four times the size of the waveforms, due to the 25 ns clock cycle. With one to two hundred waveforms to remember, the memory needed to save this information would be prohibitive. The seven-value waveform state contains the history and ensures that the underlying signal in a waveform will pick up where it left off.

## BIBLIOGRAPHY

- [1] Wikipedia. *Theodor Wulf*. [http://en.wikipedia.org/wiki/Theodor\\_Wulf](http://en.wikipedia.org/wiki/Theodor_Wulf). (last modified 25 March, 2012).
- [2] M.S. Longair. *High energy astrophysics*. Cambridge: Press Syndicate of the University of Cambridge, 1981.
- [3] Per Carlson. “A century of cosmic rays.” *Physics Today* 65 (February 2012): 30-36.
- [4] Pierre Auger. “Extensive Cosmic Ray Showers.” *Reviews of Modern Physics* 11 (1939): 288-91.
- [5] Daniela Monaldi. “Life of  $\mu$ : The Observation of the Spontaneous Decay of Mesotrons and its Consequences, 1938–1947.” *Annals of Science* 62 (2005) 4: 419-55.
- [6] Jörg R. Hörandel. *Cosmic Rays from the Knee to the Second Knee:  $10^{14}$  to  $10^{18}$  eV*. A lecture given at the International School of Astrophysics, 15<sup>th</sup> course: Astrophysics at Ultra-high Energies, 20-27 June 2006, Ettore Majorana Centre Erice, Sicily, Italy. arXiv:astro-ph/0611387v1. Monday, 13 November, 2006.
- [7] K. Nakamura *et al.* (Particle Data Group), *Journal of Physics G* 37, 075021 (2010) and 2011 partial update for the 2012 edition.
- [8] R.U. Abbasi, T. Abu-Zayyad, M. Allen, J.F. Amman, G. Archbold, K. Belov, J.W. Belz, S.Y. Ben Zvi, D.R. Bergman, S.A. Blake, O.A. Brusova, G.W. Burt, C. Cannon, Z. Cao, B.C. Connolly, W. Deng, Y. Fedorova, C.B. Finley, R.C. Gray, W.F. Hanlon, C.M. Hoffman, M.H. Holzscheiter, G. Hughes, P. Hüntemeyer, B.F. Jones, C.C.H. Jui, K. Kim, M.A. Kirn, E.C. Loh, M.M. Maestas, N. Manago, L.J. Marek, K. Martens, J.A.J. Matthews, J.N. Matthews, S.A. Moore, A. O’Neill, C.A. Painter, L. Perera, K. Reil, R. Riehle, M. Roberts, D. Rodriguez, N. Sasaki, S. R. Schnetzer, L. M. Scott, G. Sinnis, J. D. Smith, P. Sokolsky, C. Song, R.W. Springer, B. T. Stokes, S. B. Thomas, J. R. Thomas, G. B. Thomson, D. Tupa, S.Westerhoff, L. R. Wiencke, X. Zhang and A. Zech (High Resolution Fly’s Eye Collaboration). “First Observation of the Greisen-Zatsepin-Kuzmin Suppression.” *Physical Review Letters* 100 (2008): 101101.
- [9] M. Kachelrieß. *Lecture Notes on High Energy Cosmic Rays*. arXiv:0801.4376v1 [astro-ph]. ([v1] Tue, 29 Jan 2008 16:44:54 GMT).
- [10] Michał Ostrowski. *Cosmic ray acceleration at relativistic shocks, shear layers, [etc]*. A talk given at “Jean Pierre Lasota, X-ray binaries, accretion disks and compact stars.” (October, 2007); Abromowicz M. Ed. New Astron Rev. in press. arXiv:0801.1339v2. Friday, 11 January, 2008.
- [11] Jaime Alvarez-Muñiz and Todor Stanev. “The Large Scale Structure of the Galactic Magnetic Field and High Energy Cosmic Ray Anisotropy.” *Journal of Physics: Conference Series* 47 (2006): 126-31.
- [12] Markus Risse and Dieter Heck. “Energy Release in Air Showers.” *Astroparticle Physics* 20 (2004): 661-7.

- [13] Thomas Gaisser and A. Michael Hillas. “Reliability of the Method of Constant Intensity Cuts for Reconstructing the Average Development of Vertical Showers.” Paper presented at the 15<sup>th</sup> International Cosmic Ray Conference (v8 pp353-5), Plovdiv, Bulgaria, 1977.
- [14] J. Matthews. “A Heitler model of extensive air showers.” *Astroparticle Physics* 22 (2005): 387-97.
- [15] H. Kawai, S. Yoshida, H. Yoshii, K. Tanaka, F. Cohen, M. Fukushima, N. Hayashida, K. Hiyama, D. Ikeda, E. Kido, Y. Kondo, T. Nonaka, M. Ohnishi, H. Ohoka, S. Ozawa, H. Sagawa, N. Sakurai, T. Shibata, H. Shimodaira, M. Takeda, A. Taketa, M. Takita, H. Tokuno, R. Torii, S. Udo, Y. Yamakawa, H. Fujii, T. Matsuda, M. Tanaka, H. Yamaoka, K. Hibino, T. Benno, K. Doura, M. Chikawa, T. Nakamura, M. Teshima, K. Kadota, Y. Uchihori, K. Hayashi, Y. Hayashi, S. Kawakami, T. Matsuyama, M. Minamino, S. Ogio, A. Ohshima, T. Okuda, N. Shimizu, H. Tanaka, D.R. Bergman, G. Hughes, S. Stratton, G.B. Thomson, A. Endo, N. Inoue, S. Kawana, Y. Wada, K. Kasahara, R. Azuma, T. Iguchi, F. Kakimoto, S. Machida, K. Misumi, Y. Murano, Y. Tameda, Y. Tsunesada, J. Chiba, K. Miyata, T. Abu-Zayyad, J.W. Belz, R. Cady, Z. Cao, P. Hüntemeyer, C.C.H. Jui, K. Martens, J.N. Matthews, M. Mostofa, J.D. Smith, P. Sokolsky, R.W. Springer, J.R. Thomas, S.B. Thomas, L.R. Wiencke, T. Doyle, M.J. Taylor, V.B. Wickwar, T.D. Wilkerson, K. Hashimoto, K. Honda, K. Ikuta, T. Ishii, T. Kanbe, T. Tomida. “Telescope Array Experiment.” *Nuclear Physics B – Proceedings Supplements* 175-176 (January 2008): 221-6.
- [16] Robert Cady. *TA Maps*. Posted on the Telescope Array internal Wiki by GinaVasiloff on 24 January, 2008.
- [17] H. Tokuno, Y. Tameda, M. Takeda, K. Kadota, D. Ikeda, M. Chikawa, T. Fujii, M. Fukushima, K. Honda, N. Inoue, F. Kakimoto, S. Kawana, E. Kido, J.N. Matthews, T. Nonaka, S. Ogio, S. Okuda, S. Ozawa, H. Sagawa, N. Sakurai, T. Shibata, A. Taketa, S.B. Thomas, T. Tomida, Y. Tsunesada, S. Udo, T. Abu-zayyad, R. Aida, M. Allen, R. Anderson, R. Azuma, E. Barcikowski, J.W. Belz, D.R. Bergman, S.A. Blake, R. Cady, B.G. Cheon, J. Chiba, E.J. Cho, W.R. Cho, H. Fujii, T. Fukuda, D. Gorbunov, W. Hanlon, K. Hayashi, Y. Hayashi, N. Hayashida, K. Hibino, K. Hiyama, T. Iguchi, K. Ikuta, T. Ishii, R. Ishimori, D. Ivanov, S. Iwamoto, C.C.H. Jui, O. Kalashev, T. Kanbe, K. Kasahara, H. Kawai, S. Kawakami, H.B. Kim, H.K. Kim, J.H. Kim, J.H. Kim, K. Kitamoto, K. Kobayashi, Y. Kobayashi, Y. Kondo, K. Kuramoto, V. Kuzmin, Y.J. Kwon, S.I. Lim, S. Machida, K. Martens, J. Martineau, T. Matsuda, T. Matsuura, T. Matsuyama, I. Myers, M. Minamino, K. Miyata, H. Miyauchi, Y. Murano, T. Nakamura, S.W. Nam, M. Ohnishi, H. Ohoka, K. Oki, D. Oku, A. Oshima, I.H. Park, M.S. Pshirkov, D. Rodriguez, S.Y. Roh, G. Rubtsov, D. Ryu, A.L. Sampson, L.M. Scott, P.D. Shah, F. Shibata, H. Shimodaira, B.K. Shin, J.I. Shin, T. Shirahama, J.D. Smith, P. Sokolsky, T.J. Sonley, R.W. Springer, B.T. Stokes, S.R. Stratton, T. Stroman, S. Suzuki, Y. Takahashi, M. Takita, H. Tanaka, K. Tanaka, M. Tanaka, G.B. Thomson, P. Tinyakov, I. Tkachev, S. Troitsky, K. Tsutsumi, Y. Tsuyuguchi, Y. Uchihori, H. Ukai, G. Vasiloff, Y. Wada, T. Wong, M. Wood, Y. Yamakawa, H. Yamaoka, K. Yamazaki, J. Yang, S. Yoshida, H. Yoshii, R. Zollinger, Z. Zundel. “New air fluorescence detectors employed in the Telescope Array experiment.” *Nuclear Instruments and Methods in Physics Research: Section A* 676 (2012): 54-65.
- [18] Hamamatsu Photonics, K.K. *Black Rock Mesa FD and Long Ridge FD*. Posted on the Telescope Array internal Wiki by Hisao Tokuno on 1 March, 2011.

- [19] Daisuke Ikeda. *TA FD Calibration first data set ver 1.00*. Telescope Array internal document, produced on 10 March, 2009.
- [20] Analog Devices. *Complete 12-Bit, 40 MSPS Monolithic A/D Converter*. AD9224 data sheet. Rev A (1999).
- [21] Yuichiro Tameda, Akimichi Taketa, Jeremy D. Smith, Manobu Tanaka, Masaki Fukushima, Charles C.H. Jui, Ken'ichi Kadota, Fumio Kakimoto, Takeshi Matsuda, John N. Matthews, Shoichi Ogio, Hiroyuki Sagawa, Nobuyuki Sakurai, Tatsunobu Shibata, Masahiro Takeda, Stanton B. Thomas, Hisao Tokuno, Yoshiki Tsunesada, Shigeharu Udo. "Trigger electronics of the new Fluorescence Detectors of the Telescope Array Experiment." *Nuclear Instruments and Methods in Physics Research: Section A* 609 (2009): 227-34.
- [22] A. Taketa, M. Fukushima, H. Ohoka, S. Ozawa, H. Sagawa, M. Takeda, H. Tokuno, S. Udo, T. Shibata, T. Matsuda, M. Tanaka, S. Ogio, Y. Tameda, J.D. Smith, S.B. Thomas and TA group. *Data Digitization and Fluorescence Signal Recognition for Telescope Array Experiment*. Paper presented at the 29<sup>th</sup> International Cosmic Ray Conference (v8 pp209-12), Pune, India, August 3-10, 2005.
- [23] Shoichi Ogio, Hitoshi Miyauchi, Toshio Matsuyama, Daisuke Ikeda and Hisao Tokuno for the Telescope Array Collaboration. *Temperature characteristics of PMTs and calibration light sources for the Telescope Array Fluorescence Detectors*. Paper presented at the 31<sup>st</sup> International Cosmic Ray Conference, Łódź, Poland, July 7-15, 2009.
- [24] Masaaki Kobayashi, Takao Shinkawa, Takahiro Sato. "YAlO<sub>3</sub>: Ce-Am light pulsers as a gain monitor for undoped CsI detectors in a magnetic field." *Nuclear Instruments and Methods in Physics Research: Section A* 337 (1994): 335-61.
- [25] H. Tokuno, Y. Murano, S. Kawana, Y. Tameda, A. Taketa, D. Ikeda, S. Udo, S. Ogio, M. Fukushima, R. Azuma, M. Fukuda, N. Inoue, K. Kadota, F. Kakimoto, H. Sagawa, N. Sakurai, T. Shibata, M. Takeda, Y. Tsunesada. "On site calibration for new fluorescence detectors of telescope array experiment." *Nuclear Instruments and Methods in Physics Research: Section A* 601 (2009): 364-71.
- [26] Hans Naus and Wim Ubachs. "Experimental verification of Rayleigh scattering cross sections." *Optics Letters* 25-5 (2000): 347-9.
- [27] Shingo Kawana, Nobuyuki Sakurai, Toshihiro Fujii, Masaki Fukushima, Naoya Inoue, John N. Matthews, Shoichi Ogio, Hiroyuki Sagawa, Akimichi Taketa, Masato Takita, Stan B. Thomas, Hisao Tokuno, Yoshiki Tsunesada, Shigeharu Udo, Lawrence R. Wiencke. "Calibration of photomultiplier tubes for the fluorescence detector of telescope array experiment using a Rayleigh scattered laser beam." *Nuclear Instruments and Methods in Physics Research: Section A* 681 (2012): 68-77.
- [28] R.M Baltrusaitis, R. Cady, G.L. Cassiday, R. Cooper, J.W. Elbert, P.R. Gerhardy, S. Ko, E.C. Loh, M. Salamon, D. Steck and P. Sokolsky. "The Utah Fly's Eye Detector." *Nuclear Instruments and Methods in Physics Research: Section A* 240 (1985): 410-28.

- [29] C. Song, Z. Cao, B.R. Dawson, B.E. Fick, P. Sokolsky, X. Zhang. “Energy estimation of UHE cosmic rays using the atmospheric fluorescence technique.” *Astroparticle Physics* 14 (2000): 7-13.
- [30] H.M.J. Barbosa, F. Catalani, J.A. Chinellato, C. Dobrigkeit. “Determination of the calorimetric energy in extensive air showers.” *Astroparticle Physics* 22 (2004): 159-66.
- [31] John Linsley, *New Calorimetric All-Particle Energy Spectrum*. Paper presented at the 19<sup>th</sup> International Cosmic Ray Conference, La Jolla, USA, 1985.
- [32] R.U. Abbasi, T. Abu-Zayyad, M. Al-Seady, M. Allen, J.F. Amman, R.J. Anderson, G. Archbold, K. Belov, J.W. Belz, D.R. Bergman, S.A. Blake, O.A. Brusova, G.W. Burt, C. Cannon, Z. Cao, W. Deng, Y. Fedorova, C.B. Finley, R.C. Gray, W.F. Hanlon, C.M. Hoffman, M.H. Holzscheiter, G. Hughes, P. Hüntemeyer, B.F. Jones, C.C.H. Jui, K. Kim, M.A. Kirm, E.C. Loh, J. Liu, J.P. Lundquist, M.M. Maestas, N. Manago, L.J. Marek, K. Martens, J.A.J. Matthews, J.N. Matthews, S.A. Moore, A. O’Neill, C.A. Painter, L. Perera, K. Reil, R. Riehle, M. Roberts, D. Rodriguez, N. Sasaki, S.R. Schnetzer, L.M. Scott, G. Sinnis, J.D. Smith, P. Sokolsky, C. Song, R.W. Springer, B.T. Stokes, S. Stratton, S.B. Thomas, J.R. Thomas, G.B. Thomson, D. Tupa, A. Zech, and X. Zhang (The High Resolution Fly’s Eye Collaboration). “Indications of a Proton-Dominated Cosmic-Ray Composition above 1.6 EeV.” *Physical Review Letters* 104 (2010): 161101.
- [33] D. Heck and T. Pierog. *Extensive Air Shower Simulation with CORSIKA: A User’s Guide*. [http://www-ik.fzk.de/corsika/usersguide/corsika\\_tech.html](http://www-ik.fzk.de/corsika/usersguide/corsika_tech.html). (Version 6.6 from April 20, 2007).
- [34] F. Nerling, J. Blümer, R. Engel, M. Risse. “Universality of electron distributions in high-energy air showers—Description of Čerenkov light production.” *Astroparticle Physics* 24 (2006): 421-37.
- [35] F. Kakimoto, E.C. Loh, M. Nagano, H. Okuno, M. Teshima, S. Ueno. “A measurement of the air fluorescence yield.” *Nuclear Instruments and Methods in Physics Research: Section A* 372 (1996): 527-33.
- [36] R. Abbasi, T. Abu-Zayyad, K. Belov, J. Belz, Z. Cao, M. Dalton, Y. Fedorova, P. Hüntemeyer, B.F. Jones, C.C.H. Jui, E.C. Loh, N. Manago, K. Martens, J.N. Matthews, M. Maestas, D. Rodriguez, J. Smith, P. Sokolsky, R.W. Springer, J. Thomas, S. Thomas, P. Chen, C. Field, C. Hast, R. Iverson, J.S.T. Ng, A. Odian, K. Reil, D. Walz, D.R. Bergman, G. Thomson, A. Zech, F.Y. Chang, C.C. Chen, C.W. Chen, M.A. Huang, W.Y.P. Hwang, G.L. Lin. “Air fluorescence measurements in the spectral range 300–420 nm using a 28.5 GeV electron beam.” *Astroparticle Physics* 29 (2008): 77-86.
- [37] D.R. Longtin, E.P. Shettle, J.R. Hummel, J.D. Pryce. *Desert Aerosol Model for Radiative Transfer Studies*. Air Force Geophysics Laboratory, Hanscom AFB, MA. Report AFGL-TR-89-0075 (1988).
- [38] W.D. Apel, A.F. Badea, K. Bekk, A. Bercuci, J. Blümer, H. Bozdog, I.M. Brancus, A. Chilingarian, K. Daumiller, P. Doll, R. Engel, J. Engler, H.J. Gils, R. Glasstetter, A. Haungs, D. Heck, J.R. Hörandel, K.H. Kampert, H.O. Klages, G. Maier, H.J. Mathes, H.J. Mayer, J. Milke, M. Müller, R. Obenland, J. Oehlschläger, S. Ostapchenko, M. Petcu, H. Rebel, A.

Risse, M. Risse, M. Roth, G. Schatz, H. Schieler, H. Ulrich, J. van Buren, A. Vardanyan, A. Weindl, J. Wochele, J. Zabierowski. "Comparison of measured and simulated lateral distributions for electrons and muons with KASCADE." *Astroparticle Physics* 24 (2006): 467-83.

- [39] Yoshiki Tsunesada, *Energy Scale Project*. A presentation given at a general meeting of the Telescope Array Collaboration on March 19, 2011 via teleconference.